UCLA

UCLA Electronic Theses and Dissertations

Title

Wearable and Mobile Bioanalytical Systems for Health Monitoring at the Point-of-Person

Permalink

https://escholarship.org/uc/item/0fk5p778

Author

Lin, Haisong

Publication Date

2021

Peer reviewed|Thesis/dissertation

eScholarship.org Powered by the California Digital Library
University of California

UNIVERSITY OF CALIFORNIA

Los Angeles

Wearable and Mobile Bioanalytical Systems for Health Monitoring at the Point-of-Person

A dissertation submitted in partial satisfaction of the
requirements for the degree Doctor of Philosophy
in Electrical and Computer Engineering

by

Haisong Lin

2021

© Copyright by

Haisong Lin

2021

ABSTRACT OF THE DISSERTATION

Wearable and Mobile Bioanalytical Systems for Health Monitoring at the Point-of-Person

by

Haisong Lin

Doctor of Philosophy in Electrical and Computer Engineering

University of California, Los Angeles, 2021

Professor Sam Emaminejad, Chair

Point-of-care testing has greatly improved the accessibility of medical diagnostics and brought it from central laboratory closer to our daily life settings: hospitals, clinics, and pharmacies. The maturity and convergence of micro-device fabrication, sensing methodology development, and low power electronics technologies, in combination with the exponential expansion of internet of things infrastructure have provided an unprecedented opportunity to transform the accessibility of medical testing from the point-of-care to the point-of-person setting. Such transformation would create a paradigm shift in healthcare: moving away from reactive medicine to proactive medicine, which means instead of getting sick and then go to the doctor, the risk of developing disease will be calculated based on our daily measurements, informing timely and preventative actions. To realize point-of-person monitoring, the new generation of personal health monitoring systems should be: 1) portable, allowing for them to be easily distributed and embedded in our lives (e.g., in a wearable or mobile formats); 2) low cost and affordable by the general population; and 3) simple to operate, ideally eliminating the need for user intervention, for example, via automation of the underlying analytical operations. Moreover, the targeted bio-signal domain should be expanded from biophysical signals to biochemical signals to capture insightful health information related to different types of diseases at the molecular level.

Aligned with this vision, this dissertation introduces new wearable and mobile bioanalytical systems that are uniquely positioned to support health monitoring at the point-of-person. The first section of this dissertation provides the background and an overview of the point-of-person health monitoring. The second section describes the biofluid-centered operations (e.g., sampling, management, processing, and sensing) that are essential for the realization of complete solutions for point-of-person biochemical monitoring (with the particular focus on wearable format). The third section demonstrates the mobile point-of-person biochemical platforms with specifics in different automated biofluid functionalities and biomarker detection. The final section discusses the remaining challenges and outlines the potential directions to be pursued in order to enable the large-scale deployment of biochemical health monitoring, and catalyze the transition from point-of-lab and point-of-care testing to point-of-person monitoring.

The dissertation of Haisong Lin is approved.

Dino Di Carlo

Aydogan Ozcan

Xiang “Anthony” Chen

Sam Emaminejad, Committee Chair

University of California, Los Angeles

2021

TABLE OF CONTENTS

Chapter 1 Introduction 1

1.1 From Point-of-Care test to Point-of-Person monitoring 1

1.2 Dissertation overview 2

1.3 References 2

Chapter 2 Wearable point-of-person biochemical monitoring 5

2.1 Wearable biofluid sampling 5

2.1.1 Introduction 5

2.1.2 CAD-to-3D wearable microfluidic device fabrication and integration 7

2.1.3 Wearable microfluidic sweat sampling 10

2.1.4 References 13

2.2 Wearable biofluid management 15

2.2.1 Introduction 15

2.2.2 Operational principles of the wearable valving system 16

2.2.3 Wearable valve-gated microfluidic networks 20

2.2.4 Active biofluid sampling from pressure-driven sources 25

2.2.5 References 27

2.3 Wearable biofluid processing 31

2.3.1 Introduction 31

2.3.2 Operational principles of wearable ACET actuation 32

2.3.3 ACET pumping 34

2.3.4 ACET mixing 36

2.3.5 References 45

2.4 Active biofluid sensing and on-body validation 47

2.4.1 Flow rate-undistorted biomarker analysis based on valve-gated sensing interface 47

2.4.2 Contextually relevant on-body biomarker analysis 52

2.4.3 Enhanced biochemical sensing based on ACET mixing 58

2.4.4 References 64

Chapter 3 Mobile point-of-person biochemical monitoring 66

3.1 Introduction 66

3.2 Amplified addressable electromagnetic actuation 70

3.3 Functional components for advanced operations: droplet dispensing, generation, merging, and filtration 77

3.3.1 Dispensing 78

3.3.2 Generation 79

3.3.3 Filtration 81

3.3.4 Merging and mixing 82

3.4 Efficient achievement of objectives with a cross-collaborative network of ferrobots 83

3.5 Application of the ferrobotic system: automated matrix metallopeptidases bioassay 86

3.6 References..91

Chapter 4 Conclusions and prospects..96

Appendix A: Fabrication and assembly of wearable microfluidic modules for biofluid sampling……………………………………………………………………………………101

Appendix B: Fabrication procedure for epidermal microfluidic valving system 102

Appendix C: ACET theory and simulation..105

Appendix D: Theoretical analysis of the flow rate influence on the electrochemical sensor response…………………………………………………………………………………...107

Appendix E: Force balance model of ferrofluid droplet transportation 109

LIST OF FIGURES

Figure 2. 1 Overview of the CAD-to-3D flexible and adhesive microfluidic device fabrication and integration scheme: a) Conceptualized two-step fabrication of the microfluidic layers; b) Vertical assembly of the laser-cut microfluidic layers; c) Assembly of a representative 3D flexible and adhesive microfluidic device; d) Red-, Blue-, Yellow-, and Green- dyed artificial sweat samples are injected in U-, C-, L-, and A-shaped microfluidic channels to visualize the 3D integrated microfluidic module; e) Top-view and magnified images of the interwoven microfluidic region of the device, performed over 72 hours, illustrating that no leakage has occurred; f) Device mating/integration with curved glass, human skin, and flexible PCB. 8

Figure 2. 2 a) SEM images of the laser-cut tape-based microchannel (top view, microchannel bottom is PET and walls are double-sided tape) with corresponding zoomed-in images outlined. b) Optical microscope image of the cross section view of the laser-cut tape-based channel............. 9

Figure 2. 3 On-body bending test of an illustrative multilayered device (composed of PET/double-sided tape/skin adhesive medical tape layers) on different body parts: a) forearm, b) thumb metacarpal, and c) thumb knuckle with bending angles of a) 18°, b) 78°, and c) 108°, respectively. Conformal device-skin adherence under different conditions: d) no strain, e) compressing, and f) twisting. g) 180° peeling adhesion force characterization setup using Instron 5943 for different material interfaces (used in device construction). h) 180° peeling adhesion force characterization setup using Instron 5943 for the skin-skin adhesive medical tape interface. i) Force characterization results (device displacement rate: 5 mm/s, material peeling width: 3 cm). Interface 1: skin adhesive medical tape and skin. Interface 2: double-sided tape and skin adhesive medical tape. Interface 3: double-sided tape and PET. Interface 4: double-sided tape and double-sided tape..................... 10

Figure 2. 4 Wearable microfluidic sweat collector: a) Cross-section of the tape-based sweat collector structure; b) On-body application of the collector for sweat sampling, as a standalone unit. Inset shows the commercialized sweat collection device (Macroduct, ELITechGroup, France), which requires straps for holding down the device; c) Sequential optical images of the sweat secretion and in-situ collection in the designed sweat collector; d) Measured sweat volume vs. time profiles for two subjects (the sweat secretion rate is inferred from the slope of the curve-fitted lines at the desired time-points). 12

Figure 2. 5 Demonstration of two sweat sample collection and transfer processes with the aid of the sweat collection device and a syringe with an adhesive-connector: 1) In-situ collection directly from the device while it is attached on-body. 2) Ex-situ collection with the device after removed from the body. 12

Figure 2. 6 A fully-integrated wearable valving system (concept and operational principle). a) Illustration of a representative wearable bioanalytical platform, consisting of an integrated programmable microfluidic valving system interfacing a FPCB; b) Illustration of PNIPAM hydrogel shrinkage/expansion in response to temperature change above/below its LCST (induced by activation/deactivation of the microheater); c) A schematic operation example of the programmable microfluidic valving system, demonstrating biofluid routing, compartmentalization, and analysis in the selected compartment and sensor protection in the non-selected compartments; d) Illustration of control commands (automated and manual) communication for scheduled and on-demand biomarker data acquisition with the aid of user interfaces preloaded on smart consumer electronics.. 18

Figure 2. 7 a) An illustrative Scanning Electron Microscopy (SEM) of a freeze-dried hydrogel with 4% BIS (imaged once). The features are consistent with previously reported observations3;

b,c) Characterization of the hydrogel volume transition time vs hydrogel size upon activation/deactivation of the microheater for shrinkage (b) and swelling (c). Shrinkage and swelling times are defined as the time it takes for the hydrogel shrinkage/expansion to settle within 1% of its steady-state volume upon (activation/deactivation of the microheater). Error bars, mean ± s.e (n = 3 measurements from different hydrogels). 19

Figure 2. 8 Fabrication and characterization of valve-gated microfluidic networks. a) Standalone PNIPAM hydrogel shrinkage percentage vs. temperature profile (polynomial fitted curve illustrates the trend). Microscopic images of the standalone hydrogel at the annotated temperatures are shown as insets; b) Reversible hydrogel (standalone) volume transition upon activation/deactivation of the microheater (polynomial fitted curve illustrates the trend); c) A microfluidic valving characterization setup with a feedback-controlled pressure configuration; d) The measured flow rate profile through a valve-gated microfluidic channel upon the periodic activation/deactivation of the valve; e) Hydrogel layer fabrication procedure and layer-by-layer device integration scheme to realize microfluidic valving systems with different architectures; f) Optical images of the representative fabricated hydrogel layers with different numbers/arrangements of hydrogels (a black substrate background is used to visualize the transparent hydrogel features); g) Sequential optical images of progressive microfluidic routing and compartmentalization through illustrative serial, parallel, and tree microfluidic networks (constructed through integration with the same arrangement of hydrogels). 21

Figure 2. 9 Flow rate vs. hydrogel valve temperature profile (pressure is set as 15 mmHg). The valve is opened when the temperature exceeds 44 ^{o}C. Y-axis indicates the averaged continuous recordings of the flow rate for each temperature condition. 23

Figure 2. 10 Exploded view of the epidermal microfluidic valving system, which is constructed by the vertical integration of pressure regulator/hydrogel embodiments, laser-cut microfluidic channel layers, microheater/sensor array layers, and a double-sided adhesive skin adhesion layer. 24

Figure 2. 11 a) Demonstration of the layer-by-layer integration method to form the valve interface; b,c) Illustrations of (b) valve closure when the microheater is off, and (c) valve opening when the microheater is on. Microheater activation causes hydrogel shrinkage, allowing incoming biofluid to travel through the channel. 24

Figure 2. 12 Elaboration, characterization, and demonstration of pressure regulated-valving. a) An electric-hydraulic analogy. (V_{min}: minimum turn-on voltage of the transistor switch; Vmax: maximum tolerable voltage of the transistor switch; P_{min}: minimum required pressure to open the valve; P_{max}: maximum tolerable pressure of the hydraulic valve); b) Design rationale of the pressure regulation mechanism (assisted by the electrical circuit analogy); c) Optical image of the implemented pressure regulated valve; d-f) Real-time pressure recording for the characterization of the (d) maximum tolerable pressure, (e) minimum required pressure, and (f) regulated pressure. Input flow rate was set to 5 μL min^{-1}; g) Characterized accumulated pressure across pressure regulated-microfluidic channels at different flow rates. Error bars, mean ± s.e (n = 3 measurements from different devices); h) Sequential optical images of progressive microfluidic routing and compartmentalization through an illustrative pressure-regulated six-compartment valving system (performed ex-situ). 26

Figure 2. 13 Characterization of the maximum tolerable pressure (P_{max}) and minimum required pressure (P_{min}). Error bars, mean ± s.e (n = 3 measurements from different devices). 27

Figure 2. 14 Conceptual illustrations of the a) ACET-based electric field, b) temperature field , and c) flow field profiles, generated by equally-sized coplanar pair of electrodes..................... 33

Figure 2. 15 Wearable ACET actuation: a,b) Conceptual illustrations of the ACET-induced temperature (a) and flow field (b) profiles, generated by an asymmetric coplanar pair of electrodes; c,d) Epidermal microfluidic device with an embedded ACET electrode pair; e) Exploded view of the epidermal microfluidic device structure. 33

Figure 2. 16 Directional ACET flow simulation and characterization: a, b) Simulated thermal profiles of parallel (a) and orthogonal (b) electrode configurations (top-view); c, d) The respective simulated ACET-induced velocity profiles illustrating net fluid direction (top-view); e, f) Sequential images of microbeads moving downstream of the channel due to the ACET directional flow (at t = 0 s, 3 s, 6 s); g, h) Characterization of the induced velocities for a range of applied voltages, indicating velocity is proportional to the 4th power of applied voltage. 35

Figure 2. 17 ACET mixing simulation and characterization. a) Simulated thermal profile of rotationally symmetric electrodes for ACET mixing (applied voltage: 3.5 V_{rms}); b) The respective simulated ACET-induced velocity profile, illustrating a vortex-like fluid motion (velocity field and vector are correspondingly shown with streamlines and arrows); c) Experimental setup for the ACET mixing of two fluids (blank and dyed solutions); d) Optical images corresponding to mixing indices of 0, 0.4 and 1; e) Mixing index vs. time for a range of applied voltages (externally driven flow rate: 1.5 µL/min); f) Comparison of mixing index vs. flow rate with and without ACET actuation (captured at t = 2 min, applied voltage: 3.5 V_{rms}). 37

Figure 2. 18 Effect of device size scaling on ACET actuation. Simulated fluid velocity magnitude profiles of ACET mixing for three configurations (top view, microfluidic channel boundary defined by the brown line, at the 100 µm above the rotationally symmetric electrodes, applied voltage: 3.5 V_{rms}, fluid conductivity: 0.6 S/m): 1) original design (left, discussed in the main text, Fig. 3), 2) design with electrode size and gap, and channel dimensions ×2 (center), and 3) design with channel dimensions ×2 only (right). Comparison of the results of the configurations 1 and 2 yields that the increased scaling of the dimensions leads to a substantial decrease in the ACET-induced velocities (because of the reduction in electric field magnitude). Comparison of the results of the configurations 1 and 3 yields that the increased scaling of the channel (without scaling the electrode dimensions) leads to negligible decrease in the ACET-induced velocities (because the electric field concentrated region between the two electrodes is minimally affected). 38

Figure 2. 19 Stability of ACET actuation. a) Optical images of the ACET mixing process when ACET actuation was deactivated, activated for more than 8 hrs at room temperature, and activated with a surrounding temperature of 40 ^{o}C; b) Mixing index vs. time for various device orientations (externally driven flow rate: 0.5 µL/min, ACET Voltage: 3.5 V_{rms}). 40

Figure 2. 20 Influence of the solution salt concentration on ACET actuation. a) Simulated fluid velocity magnitude profile (top view, at the 100 µm above the rotationally symmetric electrodes, applied voltage: 3.5 V_{rms}, fluid conductivity: 1.6 S/m). The white box outlines the area analyzed in Fig. 2.20; b) Simulated velocity magnitude with different salt concentration levels (averaged over the outlined area in Fig. 2.20, assumed fluid conductivity values of 0.16, 0.8, 1.6 S/m for 0.1X, 0.5X and 1X PBS solutions, respectively); c) Experimentally characterized mixing index vs. solution salt concentration level (normalized with respect to the 0.1X PBS solution case). 40

Figure 2. 21 Wearable ACET excitation and visualization on-body. a) System level diagram of the ACET excitation circuit (numbers 1 through 7 indicate corresponding circuitries on the ensuing FPCB images); b) A representative push-pull circuit voltage output for ACET actuation; c) A representative assembled FPCB, integrated with the microfluidic device, placed on a human subject’s forearm; d) Front view of the assembled FPCB; e) Rear-view of the assembled FPCB; f) Top view schematic of the experimental setup for the ACET mixing of secreting sweat with an externally pumped red-dyed solution. Corresponding side-views of the two inlets of the device-epidermal interface are shown atop; g) Sequential optical images of the on-body mixing of iontophoretically induced sweat with a red-dyed solution. 42

Figure 2. 22 Overview of the wireless FPCB. Schematic diagram of the a) AC excitation circuit (including the peripheral components). b) ACET switching circuit (implementing a two-channel activation and actuation). c) Implementation of the positive and negative rails of the push-pull circuit using AP3012 (SOT-23-5 – Diodes Inc.) and LT 1617 (SOT-23 – Linear Technology) integrated circuit chips to generate +10 V and -10 V. 43

Figure 2. 23 Power consumption vs. Mixing index for different ACET excitation voltage levels (performed in 1X PBS solution, excited by a function generator Tektronix AFG3102C). 44

Figure 2. 24 Visualization of the ACET actuation with the wireless electrofluidic actuation system, performed on body with externally-pumped model solutions (1X transparent and 0.2X red-dyed PBS solutions); a) Cross-view schematic of the device-epidermal interface (for the channel containing the transparent solution); b) Sequential optical images of the on-body mixing process. For the channel containing the red-dyed solution, a PET layer is used, to physically isolate the solution from the skin. 45

Figure 2. 25 Demonstration of flow rate-undistorted biomarker analysis. a) Reaction schematic of the developed sensor (embedded within a valve-gated compartment); b, c) Current response to target analytes for (b) a glucose sensor and (c) a lactate sensor. Error bars, mean ± s.e (n = 3 measurements from different sensors); d) Simulated analyte concentration (gradient) profiles for relatively low and high flow rate conditions (low flow rate: Q = 1 µL min^{-1}, resulting in $P_e = 12.4$, high flow rate: $Q = 10$ μL min^{-1}, resulting in $P_e = 124$, assuming a channel transverse width of 2 mm and analyte diffusivity constant of 6.7×10^{-6} cm^{2} s^{-1}). The annotated dashed lines tangent to the normalized concentration curves indicate the local analyte concentration gradient for the respective case; e) Simulated local analyte concentration gradient at various flow rates (the values are normalized to that obtained for the case of 1 μL min^{-1}). The curve fitted line indicates that simulated data points present a $3Q$ relationship; f) Measured amperometric current response of a glucose sensor to 200 μM glucose solution introduced at various flow rates. The inset figure shows the corresponding measured real-time amperometric current response in the presence of progressively increasing flow rate (from 0 to 10 μL min^{-1}). The curve fitted line indicates that simulated data points present a $3Q$ relationship; g) Comparison of the estimated glucose concentration of a 200 μM glucose solution introduced at 5 μL min^{-1} (no valve) and 0 μL min^{-1} (corresponding to valve-gated condition). Error bars, mean ± s.e (n = 3 measurements from different sensors). 48

Figure 2. 26 Integration and characterization for contextually-relevant on-body biomarker analysis. a) Ex situ characterization of the prolonged operation of the pressure-regulated valve (performed over six hours); b) Ex situ characterization of the high-fidelity operation of the pressure-regulated valve in the presence of vortical vibration. The vibrational acceleration profiles are presented in the top half, and the characterized flow rate profile is captured in the bottom half; c) Optical image of a representative fully integrated programmable epidermal microfluidic valving system applied on the back of a subject with a zoomed-in view of the FPCB electronic components. The block diagram details the circuit-level valve actuation and signal processing operations; d) Illustration of the planned study for scheduled/on-demand sweat sampling during physical activity (cycling); e) Optical images of intermittently sampled, routed, and compartmentalized sweat on-body (visualized with the aid of blue dyes, embedded within the compartments). Three valves were sequentially activated/deactivated at programmed timepoints during a physical exercise. The inset figures show the characterized electrical current through the respective valves' microheaters (activated for four minutes); f) Measured sweat glucose and lactate concentrations based on-body sensor readouts (green data points). The corresponding calibration curves (dashed lines) were constructed by linear fitting the measured sensor responses to three reference samples with known analyte concentrations (blue/red data points in the case of glucose/lactate sensors). Sweat glucose readouts were obtained by the valve-gated sensing compartments 1 and 2, before and after a scheduled beverage intake event, respectively. The sweat lactate readout was obtained by the valve-gated sensing compartment 3 upon on-demand user activation. 51

Figure 2. 27 Validation of prolonged valve sealing. The maintenance of constant pressure across the valve-gated channel indicates that the channel remained fully sealed by the embedded hydrogel (without suffering from possible dehydration-induced shrinkage effects). Pressure characterization experiment was performed over 8 h, and pressure data was recorded in the first and last 1000 s-period of the experiment to illustrate the unchanged sealing status. 53

Figure 2. 28 On-body validation of valve sealing with a subject—wearing the microfluidic module on the forearm—performing shadow boxing, forearm twisting, and arm swinging at different acceleration levels, orientations, and frequencies, respectively. Optical images of the microfluidic module before/after the activities demonstrate the leakage-free preservation of the compartmentalized blue-dyed sample, illustrating the device robustness under routine user motion. 53

Figure 2. 29 a-b) COMSOL-simulated strain profile (cross-view) of a flexible microfluidic valve, under two different device bending curvatures: a) α/L = 25 °/cm and b) α/L = 50 °/cm. The hydrogel embodiment sustains minimal strain, as it is located at the neutral plane. Hydrogel valve: 1 mm in length, 170 μm in height; c-d) Experimental validation of fluid valving under two device bending curvatures: c) α/L = 25 °/cm and d) α/L = 50 °/cm. The valve is activated after 0.5 min. 54

Figure 2. 30 a) Schematic diagram of the actuation circuit, including the programmable current source and multiplexer (for microheaters) circuitries; b) The measured current through six electrical resistive microheaters upon the periodic and sequential activation/deactivation of the microheater array (resistive load: 25 Ω, connected at the output of each of the actuation channels). 56

Figure 2. 31 Schematic diagrams of the sensing (consisting of potentiostat and LPF), MCU, wireless transmission (Bluetooth), and power regulating circuits. 56

Figure 2. 32 a) intermittent sample compartmentalization via sequential on-body valving (using blue dyes for visualization); b-d) On-body sweat glucose (b, c) and lactate (d) sensor readouts and the corresponding calibration curves. Sweat glucose readouts in (b) and (c) were obtained before and after beverage intake, respectively. 58

Figure 2. 33 Sandwiched actuation and sensing interface: a) Cross-section schematic of the sandwiched-electrode array structure; b) Individual sensing (left) and actuation (right) electrode arrays, and final assembled device (middle, where the actuation electrode pair is aligned to face the sensor's working electrode); c) COMSOL ACET simulation (conductivity: 0.6 S/m, dielectric constant: 80, excitation: 3.5 V_{RMS}, ambient temperature: 25 °C), illustrating the temperature profile and induced flow pattern established the rotationally symmetric electrode pair; d) Amperometric H_2O_2 sensing mechanism and corresponding calibration curves with and without ACET actuation; e) Enzymatic glucose sensing mechanism and corresponding calibration curves with and without ACET actuation; f, g) Comparison of corresponding amperometric sensors' sensitivities (f) and response time (g) with and without ACET actuation (error bars indicate standard error, N = 3); h) Comparison of blood and sweat glucose levels of two subjects during 12-h fasting and 0.5 h after glucose intake (30 g glucose), demonstrating the elevation of sweat glucose upon glucose intake, as measured by the actuation-assisted glucose sensor. 60

Figure 2. 34 Recordings of the sensor steady-state responses shown in Fig. 2.33d,e: a) H_2O_2 without ACET actuation, b) H_2O_2 with ACET actuation, c) Glucose without ACET actuation, and d) Glucose with ACET actuation 62

Figure 2. 35 Reproduced sensor calibration results with and without ACET actuation: a) H_2O_2 sensor response and b) Glucose sensor response... 62

Figure 2. 36 Recordings of the H_2O_2 (a) and glucose (b) sensors' amperometric responses with and without the presence of ACET. The corresponding insets show the normalized slope functions (see Materials and method section) for the determination of the sensors' response times. 63

Figure 2. 37 a) Enzymatic choline sensing mechanism and representative calibration curves of the sensor response (with and without ACET actuation). b, c) Comparison of choline sensor's sensitivity (b) and response time (c) for the cases of with and without ACET actuation (error bars indicate standard error, N = 3).. 64

Figure 3. 1 The overview of ferrobotic system concept and mechanism. a) An analogy: mobility and automation in an AGV system and the devised ferrobotic system; b) Simulation results depicting the amplification of the actuation capability with the magnetic motor (the x-axis is the vertical distance from the center of the magnetic source); c) Optical image of a representative multifunctional ferrobotic system capable of performing diverse operations, including droplet package transportation, merging, generation, filtration, dispensing, and sensing. Rendered images of the droplets are for illustration purposes only (droplets can form hemisphere or disk-like shapes depending on the channel geometry). 69

Figure 3. 2 EM-coil geometry and magnetic field simulation. Oblique (a), top (b) and side (c) view of the EM-coil's geometry; d) COMSOL simulation results of the spatial gradient of the magnetic field with and without the magnetic motor (i.e., the ferrobot). The x-axis is the distance from the magnetic source center along the z-axis; e,f) magnetic field intensity (e) and spatial gradient of the magnetic field (f) in x-z plane in the absence of the ferrobot. The dashed lines outline the boundaries of the microfluidic chamber; g) spatial gradient of the magnetic field in x-y plane (1 mm above the coil) in the absence of the ferrobot; h,i) magnetic field intensity (H) and spatial gradient of the magnetic field (I) in x-z plane in the presence of the ferrobot. The dashed lines outline the boundaries of the microfluidic chamber; j) spatial gradient of the magnetic field in the x-y plane (1 mm above the coil) in the presence of the ferrobot. 71

Figure 3. 3 Design and characterization of the navigation floor for package transportation. a) Schematic diagram of the control circuitry; b) Optical image of the implemented control circuitry and the navigation floor with the close-up view of four neighboring EM coils; c) Overlaid sequential images (derived from video frames) visualize the commuted path of the ferrobot (programmed with different navigation plans; the duration for commuting "U", "C", "L" and "A" paths were correspondingly 1.4 s, 1.4 s, 0.7 s, and 2.3 s); d) Characterization of the maximum transportation velocity for two different ferrofluid concentrations. Error bars indicate standard error (n = 3); e) Characterization of the oscillatory transportation of a package with a ferrobot (sensed with an impedance sensing electrode pair) to evaluate the robustness of the ferrobotic actuation (performed for > 24 hours); f) FFT analysis of the oscillatory profile measured by the impedance sensing electrodes in part (e). Inset shows variation of the fundamental frequency of the 2000 s-segmented time windows, depicting near zero variation. 73

Figure 3. 4 Multi-ferrobot transportation. Overlaid sequential images visualize the commuted paths of the four simultaneously commuting ferrobots (duration: 7 s)....................................... 74

Figure 3. 5 Characterization of the average velocity profile of the droplet. a) Sequential imaging of a representative droplet moving along the navigation floor; b) Corresponding measured averaged velocity... 75

Figure 3. 6 Impedance spectrum measured by the impedance sensing electrode pair. a) The impedance spectrum shows distinct impedance differences when the ferrobot is present vs. not present (inset shows the droplet position with respect to the sensing electrodes for the corresponding measurements); b,c) Corresponding FFT of the impedance measurements tracking the oscillatory motion (1 Hz, over 1000 cycles) of the droplet with compositions: (b) 50% ferrofluid (diluted in water) and (c) 50% ferrofluid (diluted in plasma). 77

Figure 3. 7 a) Schematic illustration of the droplet dispensing mechanism, involving the transportation of the package against a corrugated microfluidic wall; b) Sequential optical images of the droplet dispensing process; c) Characterization of the dispensed droplets’ size for different corrugated opening widths. Error bars indicate standard error (n = 10)...................................... 79

Figure 3. 8 Dispensed droplet characterization. Characterization of the dispensed droplets’ size for different corrugated opening widths and using two ferrofluid concentrations. Error bars indicate standard error (n = 10)... 79

Figure 3. 9 a) Schematic illustration of the droplet generation process, involving the droplet transportation to a VIA-like orifice; b) Sequential optical images of the droplet generation process;

c) Characterization of the generated droplets' volume for different orifice diameters. Error bars indicate standard error (n = 20). 80

Figure 3. 10 Droplet generation characterization. a) Optical microscopic images of generated droplets using 169 µm-diameter orifice; b) Characterization of droplet generation rate for varying orifice diameters (based on counting the generated droplets over 4 s). 80

Figure 3. 11 Collective transportation of nL-droplets by a ferrobot. Sequential imaging indicates the collection and transportation of generated nL-droplets by a ferrobot through a 2 mm-wide × 1mm-long pore. 81

Figure 3. 12 a) Schematic illustration of the filtration mechanism; b) Optical image of the solution sample before and after filtration; c) Bead counts before and after filtration (three trials). 82

Figure 3. 13 a) Schematic illustration of droplet merging and mixing mechanisms; b) Optical images to visualize the droplet merging (upon applying 2 V) and mixing process (with and without active mixing); c) Comparison of the progressive mixing index for the two cases of with and without active mixing. 83

Figure 3. 14 Efficient package sorting with a cross-collaborative network of ferrobots. a)System-level view of the sorting procedure; b,c) Comparison of the sorting efficiency achieved by (b) a single ferrobot and (c) eight ferrobots tasked with sorting a random sequence of eight packages. State-by-state transitions for both scenarios are illustrated and the table details the commuted distance of each ferrobot (left). The snapshots from the sorting experiment performed with eight ferrobots are shown on the right (captured at the end of each state); d) the total temporal unit steps required for sorting 2, 4, 8, and 16 packages (based on statistical averaging of all the possible permutations).. 84

Figure 3. 15 Merge sort algorithm and sorting performance for single vs. multi ferrobots. a) Representative schematic of the application of recursive merge sort algorithm to sort an array of 8 integers; b) The averaged total temporal unit steps required for sorting n = 2, 4, 8, and 16 packages, performed with a single or n ferrobots (simulated based on 10,000 randomly generated sequence of packages for each scenario, error bars indicate standard deviation). 86

Figure 3. 16 Pipelined and automated MMP assay, performed by the ferrobotic system. a) General workflow of the MMP assay equipped with a dynamic self-calibration mechanism; b) Illustration of the ferrobotic tasks in relation to the navigation floor over the processing of a representative sample (performed by three ferrobots); c) Overview of the navigation plans of the three deployed ferrobots (F_1, F_2, and F_3) with annotated locations of interest; d) The detailed timeline of the ferrobots' status (commuting with/without package, standby), with annotated locations of interest. Overlaid sequential video frames illustrating the status at two representative stages; e) Illustration of the FRET pair from the MMP substrate cleaved by the MMPs present in the sample to yield a fluorescent product that is no longer quenched; f) The fluorescent readouts from the calibration and output wells, after automated ferrobotic processing and 10 minutes of incubation. The concentration of MMP in the test sample is estimated with the aid of a real-time calibration standard curve generated from the 4 calibrator samples (estimated: 0.0078 U/mL vs. expected: 0.008 U/mL); g) Estimated MMP concentrations in five tested human plasma samples (performed by the ferrobotic system and manually by a technician, $p < 0.01$). 88

Figure 3. 17 Characterization of the MMP assay. The recorded fluorescence signals from the calibration well array, where each well contains PBS dilutions of collagenase at different end concentrations.. 90

ACKNOWLEDGEMENTS

Throughout the journey of my doctoral work, I have received a great deal of support and assistance from the people around me. Without them, I cannot make this work possible. I feel so grateful for having them in my life and would like to appreciate them in this section.

First, I would like to express my sincere gratitude to my advisor, Professor Sam Emaminejad, for his passion, inspiration, and encouragement that helped me to set the aim of my career and even the goal for my life. I would like to thank his professional and patient guidance that supports me to finish this journey and to prepare for the new journey that is about to start.

I would also like to appreciate Professor Dino Di Carlo for the great collaboration opportunities of previous and on-going projects related to Ferrobot. Without his valuable and professional advice and tremendous resources support, such as expertise students and lab instruments, our current progress could not be possible.

I would like to thank my other committee members: Professor Aydogan Ozcan and Professor Anthony Chen for offering insightful feedbacks on both my defense and dissertation. These feedbacks helped me to gain lots of confidence for my future academic career.

Thankfully, I am grateful for not only having respectful professors to seek advice from, I am also very grateful for having talented colleagues around me to brainstorm, discuss, back-up and learn from each other's. I would like to thank my first lab partner, Yichao Zhao, for his contribution in electrochemical sensor development. Our collaborative work can be found in chapter 2.1 which is also published on the journal of Lab on a Chip titled as "A rapid and low-cost fabrication and integration scheme to render 3D microfluidic architectures for wearable biofluid sampling, manipulation, and sensing". I also want to thank my partner, Jiawei Tan, for his contribution in material synthesis, system fabrication, integration and experiments. Our collaborative work can be found in chapter 2.2 which is also published on the journal of Nature Communications titled as “A programmable epidermal microfluidic valving system for wearable biofluid management and contextual biomarker analysis”. I would like to thank my colleagues: Hannaneh Hojaiji and Shuyu Lin for their efforts in circuit designing and Multiphysics simulations. Our collaborative progress can be found in chapter 2.3 which is also published on the journal of Lab on a Chip titled as “A wearable electrofluidic actuation system”. I would also like to thank my lab partner: Wenzhuo Yu and my collaborator from Dino’s group: Yilian Wang for our great collaborative achievement of the Journal cover on Science Robotics. The result can be found in the chapter 3 and the paper on Science Robotics is titled with “A ferrobotic system for automated microfluidic logistics”.

I would like to appreciate my other colleagues from our lab: Wang Bo, Xuanbing Cheng, Jialun Zhu, Zhaoqing Wang, and Kiarash Sabet, as well as colleagues from collaborators’ lab: Shiming Zhang, Wujin Sun, and Christopher Yang. I thoroughly enjoyed every moment we interacted and brainstormed with each other, and I am very proud of the work we published all together. I would also like to thank the very talented and hardworking undergraduate students who contributed significantly to this work: Tianyou Cai, Kimber King, Kamyar Salahi, Meghana Malige, Yibo Wang, Siyang Yang, Eric Tang, Nathan Chen, Kevin Sun, Darren Lo, and Brain Cheng.

Last but not least, I want to thank my parents and Xingyu who was acknowledged in my master thesis as my girlfriend, but now as my wife, for their unconditional love and support.

VITA

2012-2016	B.S., Electrical and Computer Engineering Iowa State University Ames, IA
2014-2016	Undergraduate research assistant, Laboratory for MEMS & Biochips Iowa State University Ames, IA
2016-2018	M.S., Electrical and Computer Engineering University of California, Los Angeles Los Angeles, CA
2018-2019	Teaching assistant, Electrical and Computer Engineering University of California, Los Angeles Los Angeles, CA
2016-2021	Graduate research assistant, Interconnected & Integrated Bioelectronics Lab University of California, Los Angeles Los Angeles, CA

SELECTED PUBLICATIONS

†co-first author

1. **H. Lin**†, J. Tan†, J. Zhu, S. Lin, Y. Zhao, W. Yu, H. Hojaiji, B. Wang, S. Yang, X. Cheng, Z. Wang, E. Tang, C. Yeung, S. Emaminejad, "A Programmable Epidermal Microfluidic Valving System for Wearable Biofluid Management and Contextual Biomarker Analysis," ***Nature Communications*** (2020)

2. W. Yu†, **H. Lin**†, Y. Wang†, N. Chen, X. He, K. Sun, D. Lo, B. Cheng, C. Yeung, J. Tan, D. Di Carlo, and S. Emaminejad, "A Ferrobotic System for Automated Microfluidic Logistics," ***Science Robotics*** (2020), (Cover)
3. **H. Lin**†, H. Hojaiji †, S. Lin†, C. Yeung, Y. Zhao, B. Wang, M. Malige, Y. Wang, K. King, W. Yu, J. Tan, Z. Wang, X. Cheng, S. Emaminejad, "A Wearable Electrofluidic Actuation System," ***Lab on a Chip*** (2019)
4. **H. Lin**, Y. Zhao, S. Lin, B. Wang, C. Yeung, X. Cheng, Z. Wang, T. Cai, W. Yu, K. King, J. Tan, K. Salahi, H. Hojaiji, S. Emaminejad, "A Rapid and Low-cost Fabrication and Integration Scheme to Render 3D Microfluidic Architectures for Wearable Biofluid Sampling, Manipulation, and Sensing," ***Lab on a Chip*** (2019)
5. J. Tan, **H. Lin**, S. Lin, W. Yu, J. Zhu, Y. Zhao, X. Cheng, S. Yang, E. Tang, and S. Emaminejad, "A Stimuli-responsive Hydrogel Array Fabrication Scheme for Large-scale and Wearable Microfluidic Valving," ***IEEE Journal of Microelectromechanical Systems*** (2020)
6. S. Lin, W. Yu, B. Wang, Y. Zhao, K. En, J. Zhu, X. Cheng, C. Zhou, **H. Lin**, Z. Wang , H. Hojaiji, C. Yeung, C. Millad, R. W. Davise, and S. Emaminejad "Noninvasive wearable electroactive pharmaceutical monitoring for personalized therapeutics," ***Proceedings of the National Academy of Sciences*** (2020)
7. Y. Zhao†, B. Wang†, H. Hojaiji, Z. Wang, S. Lin, C. Yeung, **H. Lin**, P. Nguyen, K. Chiu, K. Salahi, X. Cheng, J. Tan, B. A. Cerrillos, S. Emaminejad, "A Wearable Freestanding Electrochemical Sensing System," ***Science Advances*** (2020)

Chapter 1 Introduction

1.1 From Point-of-Care test to Point-of-Person monitoring

Point-of-care testing has greatly improved the accessibility of medical diagnostics and brought it from centralized laboratory to local decentralized settings, such as: hospitals, clinics, and pharmacies. To enable longitudinal and objective assessment of the health status of individuals in daily life, more decentralized health monitoring system is needed at the point of person settings such as: home and workplace. Recently, the maturity and convergence of micro-device fabrication, sensing methodology development, and low power electronics technologies, in combination with the exponential expansion of internet of things infrastructure have provided an unprecedented opportunity to accelerate this decentralization process of health monitoring and to catalyze the transition from discrete point-of-lab and point-of-care testing to near-continuous point-of-person monitoring [1-7]. These transformation would create paradigm shifts in healthcare such as: medical treatment shift (from reactive medicine to proactive medicine), accessibility shift (from testing intervals on the order of months and years to testing intervals on the order of minutes and hours), device format shift (from large instrument in the laboratory to portable format that is closer to our lives), biofluid shift (from invasive: *e.g.* blood to noninvasive: *e.g.* sweat, saliva, and urine.), and cost shift.

To realize point-of-person monitoring, the new generation of personal health monitoring systems should be: 1) portable, allowing for them to be easily distributed and embedded in our lives (e.g., in a wearable or mobile formats); 2) low cost and affordable by the general population; and 3) simple to operate, ideally eliminating the need for user intervention, for example, via automation of the underlying analytical operations. Moreover, at present, most health monitoring systems are only capable of tracking physical activities and vital signs. They fail to access molecular-level biomarker information that provide insight into our body's dynamic chemistry [8-17]. In that regard, the targeted bio-signal domain should be expanded from biophysical signals to biochemical signals to capture insightful health information related to different daily activities and different types of diseases.

1.2 Dissertation overview

Aligned with this vision, this dissertation introduces new wearable and mobile bioanalytical systems that are uniquely positioned to support health monitoring at the point-of-person. The second chapter describes the essential wearable biofluid-centered operations we developed such as sampling, management, processing, and sensing of biofluid, for point-of-person biochemical monitoring. The third chapter demonstrates our mobile point-of-person biochemical platforms (Ferrobot) with specifics in achieving different biofluid functionalities and completing pipelined biomarker detection in a fully-automated manner. The final section discusses the remaining challenges and outlines the potential directions to be pursued in order to enable the large-scale deployment of biochemical health monitoring, and catalyze the transition from point-of-lab and point-of-care testing to point-of-person monitoring.

1.3 References

1. Kim, J., Campbell, A. S. & Wang, J. Wearable non-invasive epidermal glucose sensors: A review. Talanta 177, 163–170 (2018).
2. Sempionatto, J. R. et al. Eyeglasses based wireless electrolyte and metabolite sensor platform. Lab Chip 17, 1834–1842 (2017).
3. Heikenfeld, J. Non-invasive Analyte Access and Sensing through Eccrine Sweat: Challenges and Outlook circa 2016. Electroanalysis 28, 1242–1249 (2016).

4. Glennon, T. et al. ‘SWEATCH’: A Wearable Platform for Harvesting and Analysing Sweat Sodium Content. Electroanalysis 28, 1283–1289 (2016).
5. Heikenfeld, J. et al. Accessing analytes in biofluids for peripheral biochemical monitoring. Nat. Biotechnol. (2019). doi:10.1038/s41587-019-0040-3
6. Durdiaková, J., Fábryová, H., Koborová, I., Ostatníková, D. & Celec, P. The effects of saliva collection, handling and storage on salivary testosterone measurement. Steroids 78, 1325–1331 (2013).
7. Mohamed, R., Campbell, J.-L., Cooper-White, J., Dimeski, G. & Punyadeera, C. The impact of saliva collection and processing methods on CRP, IgE, and Myoglobin immunoassays. Clin. Transl. Med. 1, 19 (2012).
8. Zhu, C. et al. Stretchable temperature-sensing circuits with strain suppression based on carbon nanotube transistors. Nature Electronics 1, 183–190 (2018).
9. Nie, B., Li, R., Brandt, J. D. & Pan, T. Microfluidic tactile sensors for three-dimensional contact force measurements. Lab Chip 14, 4344–4353 (2014).
10. Chou, H.-H. et al. A chameleon-inspired stretchable electronic skin with interactive colour changing controlled by tactile sensing. Nat. Commun. 6, 8011 (2015).
11. Chen, X. et al. CVD-grown monolayer MoS2 in bioabsorbable electronics and biosensors. Nat. Commun. 9, (2018).
12. Han, S. et al. Battery-free, wireless sensors for full-body pressure and temperature mapping. Sci. Transl. Med. 10, (2018).
13. Lee, J. et al. Conductive fiber-based ultrasensitive textile pressure sensor for wearable electronics. Adv. Mater. 27, 2433–2439 (2015).

14. Dagdeviren, C. et al. Conformal piezoelectric systems for clinical and experimental characterization of soft tissue biomechanics. Nat. Mater. 14, 728–736 (2015).
15. Yokota, T. et al. Ultraflexible organic photonic skin. Sci Adv 2, e1501856 (2016).
16. Lochner, C. M., Khan, Y., Pierre, A. & Arias, A. C. All-organic optoelectronic sensor for pulse oximetry. Nat. Commun. 5, 5745 (2014).
17. Wang, C. et al. Monitoring of the central blood pressure waveform via a conformal ultrasonic device. Nature Biomedical Engineering 2, 687–695 (2018).

Chapter 2 Wearable point-of-person biochemical monitoring

2.1 Wearable biofluid sampling

2.1.1 Introduction

To achieve wearable biochemical monitoring in a wearable format, the first step is to collect biofluid *in situ* (*e.g.* collection of sweat should be directly on top of the skin). Accordingly, wearable bioanalytical devices utilize mechanically flexible microfluidic housings to collect and analyze the biofluid samples, while minimizing sample evaporation and external contamination [1-3]. Numerous device fabrication-related criteria including scalability, cost-effectiveness, flexibility, compactness, and ease-of-integration are yet to be addressed to catalyze the large-scale deployment of demonstrated and envisioned bioanalytical devices for general population monitoring [4-6]. Specifically, high throughput manufacturing-amenable fabrication schemes are required to render low-cost and skin-conformal microfluidic modules. That is because, to eliminate the fundamental challenges such as contamination (from residues of old samples) and sensor biofouling, the microfluidic modules are implemented as disposable units, which are to be replaced frequently to perform longitudinal monitoring. Furthermore, the fabrication scheme must be capable of rapidly realizing and integrating a variety of bioanalytical components, including biofluid manipulation, actuation, and sensing interfaces within a compact footprint to allow for the quantification of a panel biomarkers, which is key to providing a comprehensive view of the user's physiological state.

The majority of reported wearable bioanalytical device implementations rely on conventional Polydimethylsiloxane (PDMS)-based soft-lithography methods [7-9], which require access to resource-intensive facilities for device fabrication and assembly. Specifically, for such approaches, the mold is fabricated in nanofabrication and cleanroom facilities, following timeconsuming and multi-step protocols, with designs that are fixed by corresponding mask designs, which often need to be separately custom-ordered and purchased from third-party vendors (for each design) [10,11]. Additionally, the device assembly requires surface activation by oxygen plasma treatment, which provides a short time-window for alignment and bonding. Furthermore, the reported wearable biomarker sensors relied on the analysis of the sample biofluid, collected in 2D microfluidic devices [7-9]. The spatial constraints of these sensors inherently limits the versatility and quantity of bioanalytical operations, consequently constraining the diversity and frequency of end-point assessments.

To address these limitations, we devise a simple, scalable, and low-cost "CAD-to-3D Device" fabrication and integration scheme, which renders 3D, flexible, and complex microfluidic architectures for wearable sweat sampling. The devised scheme is based on laser-cutting and vertical assembly of thin layers of tape-based substrates. The laser-cutter can be programmed at the software-level to rapidly define microfluidic features such as biofluid collection interface, microchannels, and VIAs (vertical interconnect access), with different dimensions. By leveraging the adhesive property of the substrates and elaborate positioning of microfluidic VIAs, the 2D-patterned layers can simply be stacked and fluidically routed to form leakage-free, multilayered, and 3D architectures.

The devised fabrication and integration scheme can be adapted to implement the reliable and leakage-free epidermal sweat sampling capability. To demonstrate this point, a flexible and adhesive sweat collector interface is designed that can simply attach to the skin as a standalone unit. The interface is based on a microfluidic epidermal configuration, which harvests sweat, with minimized dead volume, and uses a fluidic VIA to route the collected sample through a microfluidic channel with the planar Archimedean Spiral design. This configuration allows for the visualizing the sweat secretion profile and inferring the secretion rate through optical imaging.

2.1.2 CAD-to-3D wearable microfluidic device fabrication and integration

Unlike conventional soft lithography PDMS-based microfluidic devices, which require resource-intensive cleanroom procedures and photomasks (with fixed designs) to create the master mold, laser-cutting involves only two simple steps: 1) designing the microfluidic layers of the device using a computer-aided design (CAD) software and 2) laser-cutting the loaded substrates (tape- or PET-based) to pattern the designed microfluidic features on a sequence of layers (Fig. 2.1a, Appendix A). The whole procedure typically takes on the order of a few minutes, which is significantly faster than soft lithography that takes on the order of at least a few hours. After laser-cutting the microfluidic layers, the device is assembled by sequentially and vertically stacking the layers (Fig. 2.1b). The laser-cut 2D embodiments within the tape- and PET-based layers (optionally, pre-patterned with electrodes) form microchannels and VIAs. Scanning electron microscope (SEM) and optical microscope images of the top and cross-section view of a representative laser cut tape based microchannel are shown in Fig. 2.2. With proper alignment of VIAs and microchannels (Fig 2.1c), fluidic connections in the vertical direction were achieved, rendering complex and spatially efficient 3D microfluidic structures. For example, as shown in (Fig 2.1d), the VIAs were designed to connect microfluidic pathways in different layers. Specifically, as shown in Fig. 2.1e, the red-dyed biofluid in the U-shaped channel weaved over and under the blue-dyed biofluid in the C-shaped channel while keeping the two liquids physically isolated. To validate the ability of our scheme to render well-sealed 3D microfluidic devices, an example microfluidic configuration is fabricated (with an interwoven over/under-pass design) and filled with color dyes. As can be seen in Fig. 2.1e, no leakage was found during the characterization period of > 72 hours. The flexible and the adhesive nature of the rendered microfluidic devices allow for their ease of mating/integration with different types of surfaces, including curved glass, flexible printed circuit board (PCB), and human skin (Fig. 2.1f).

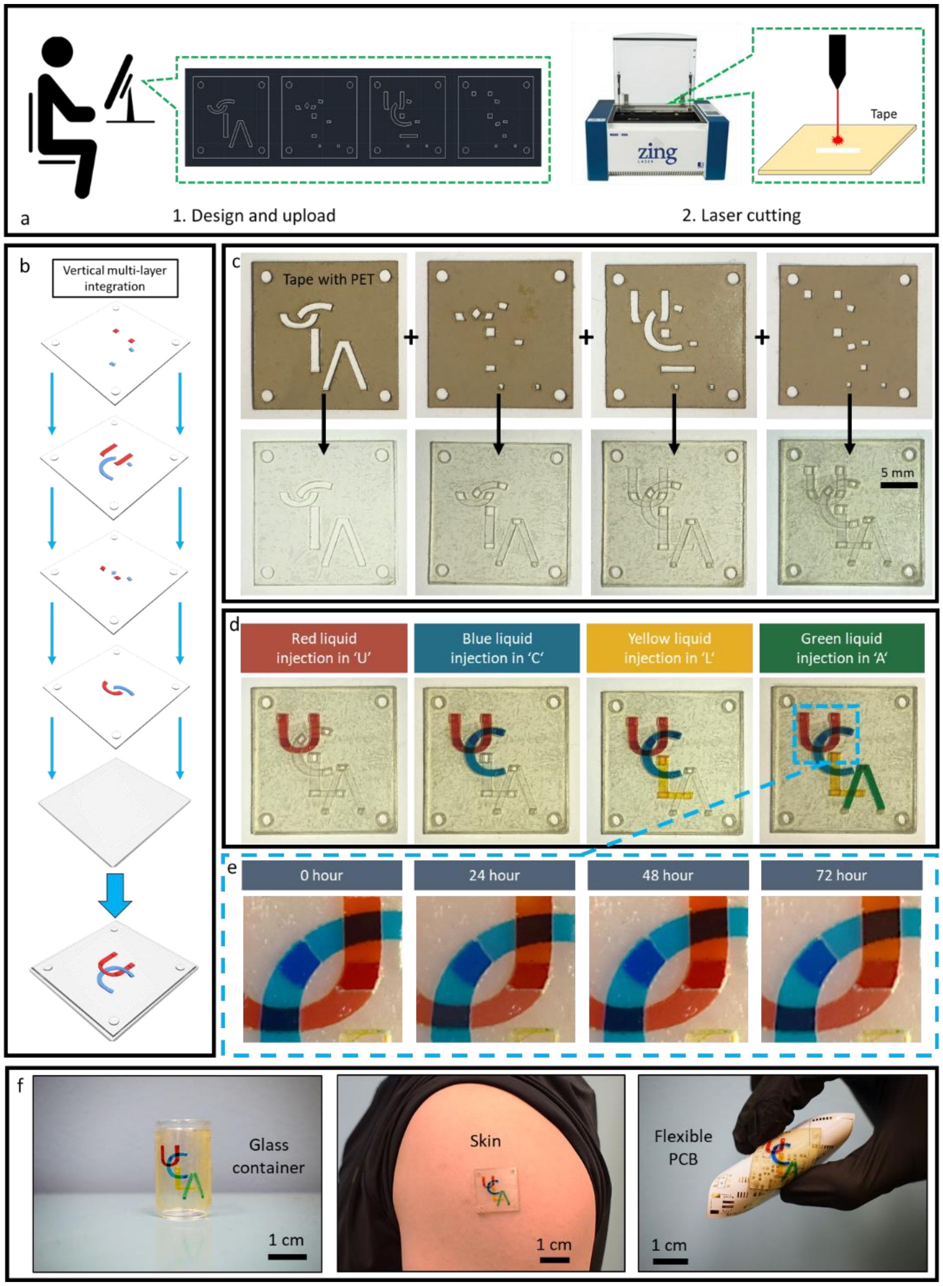

a
1. Design and upload
zing
Tape
2. Laser cutting
b
Vertical multi-layer integration
c
Tape with PET
+
5 mm
d
Red liquid injection in 'U'
Blue liquid injection in 'C'
Yellow liquid injection in 'L'
Green liquid injection in 'A'
e
0 hour
24 hour
48 hour
72 hour
f
Glass container
1 cm
Skin
1 cm
Flexible PCB
1 cm

Figure 2. 1 *Overview of the CAD-to-3D flexible and adhesive microfluidic device fabrication and integration scheme: a) Conceptualized two-step fabrication of the microfluidic layers; b) Vertical assembly of the laser-cut microfluidic layers; c) Assembly of a representative 3D flexible and adhesive microfluidic device; d) Red-, Blue-, Yellow-, and Green- dyed artificial sweat samples are injected in U-, C-, L-, and A-shaped microfluidic channels to visualize the 3D integrated* *microfluidic module; e) Top-view and magnified images of the interwoven microfluidic region of the device, performed over 72 hours, illustrating that no leakage has occurred; f) Device mating/integration with curved glass, human skin, and flexible PCB.*

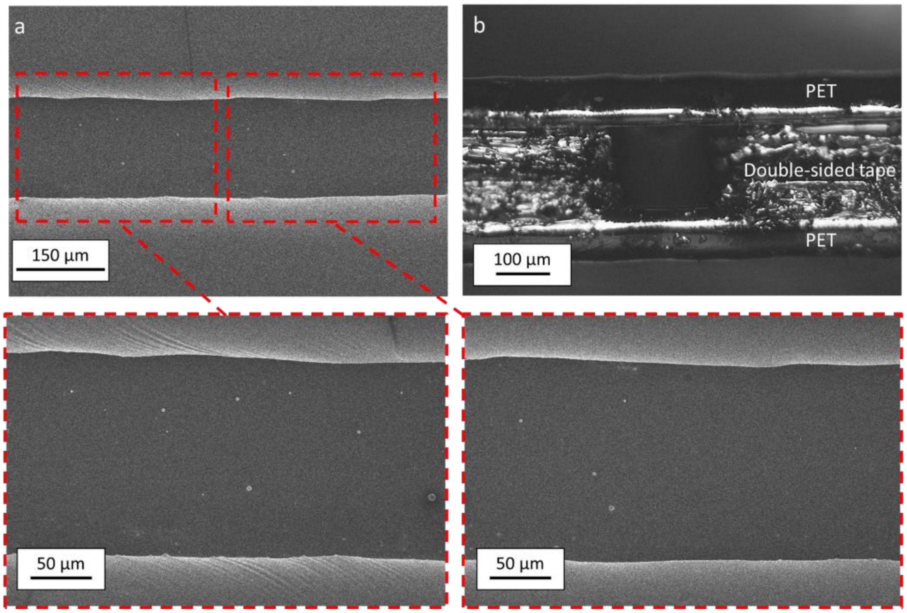

Figure 2. 2 *a) SEM images of the laser-cut tape-based microchannel (top view, microchannel bottom is PET and walls are double-sided tape) with corresponding zoomed-in images outlined. b) Optical microscope image of the cross section view of the laser-cut tape-based channel.*

To demonstrate the robustness of the microfluidic device adhesion to the body, first, an illustrative microfluidic device (composed of PET, double-sided tape, and skin adhesive medical tape) was adhered onto various body parts such as the forearm, thumb metacarpal, and thumb knuckle (with bending angles ranging from 18^o to 108^o, Fig. 2.3a-c). Next, compression and twisting tests on the body-worn device indicated the preservation of the device's structural integrity and skin adhesion (no delamination) after application of external forces (Fig. 2.3d-f). Lastly, the adhesion forces between multiple material interfaces were characterized using 180° peeling adhesion force characterization setup (Fig. 2.3g, h). As shown in Fig. 2.3i, the results indicate that the adhesion forces between all device internal layers are all significantly stronger than the adhesion force between skin and skin adhesive medical tape (which is commonly used in the reported literature and for medical use).

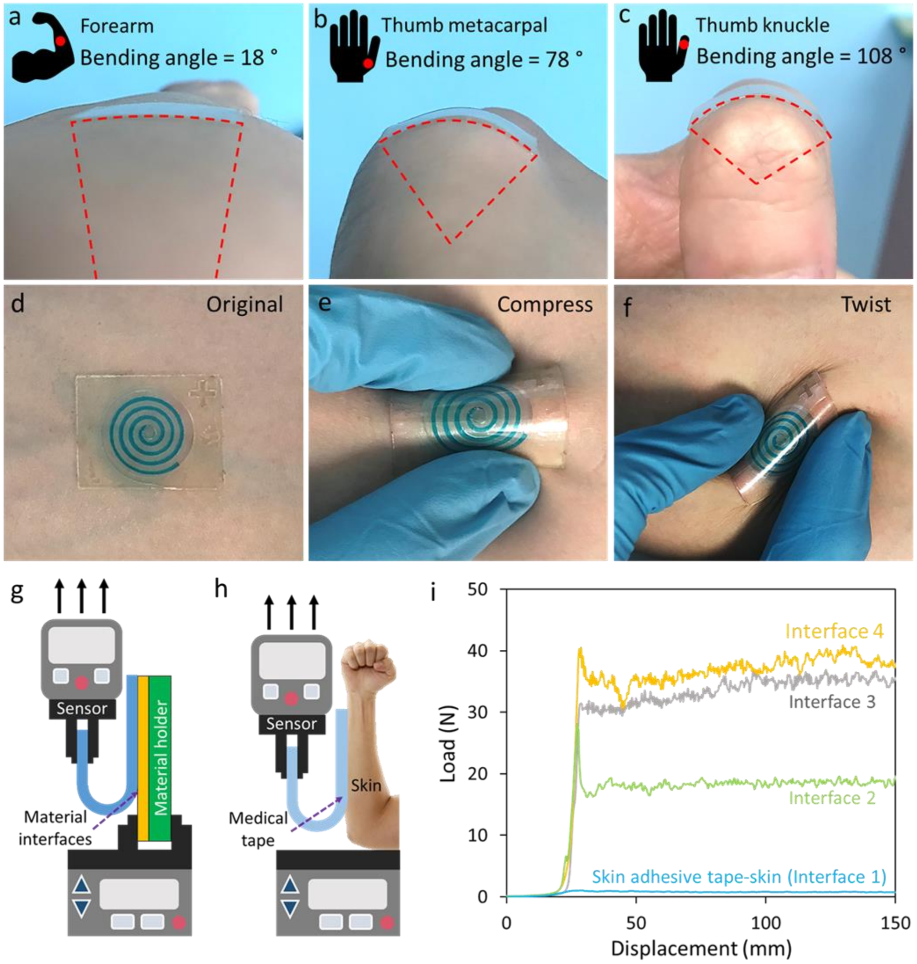

Figure 2. 3 *On-body bending test of an illustrative multilayered device (composed of PET/double-sided tape/skin adhesive medical tape layers) on different body parts: a) forearm, b) thumb metacarpal, and c) thumb knuckle with bending angles of a) 18°, b) 78°, and c) 108°, respectively. Conformal device-skin adherence under different conditions: d) no strain, e) compressing, and f) twisting. g) 180° peeling adhesion force characterization setup using Instron 5943 for different material interfaces (used in device construction). h) 180° peeling adhesion force characterization setup using Instron 5943 for the skin-skin adhesive medical tape interface. i) Force characterization results (device displacement rate: 5 mm/s, material peeling width: 3 cm). Interface 1: skin adhesive medical tape and skin. Interface 2: double-sided tape and skin adhesive medical tape. Interface 3: double-sided tape and PET. Interface 4: double-sided tape and double-sided tape.*

2.1.3 Wearable microfluidic sweat sampling

A sweat collector for on-body application is designed with the Archimedean Spiral shape. As shown in Fig. 2.4a, the on-body collector is composed of two fluid layers: 1) the sweat collection chamber with the double-sided tape wall, PET ceiling, and the skin treated as substrate, and 2) the sweat flow channel with the double-sided tape wall and PET as both substrate and ceiling. In order to minimize the sample volume wasted in the chamber layer, a spacer layer (Scotch single sided self-seal laminating sheets, 3M, USA) was added to occupy liquid space in the chamber (reducing the dead volume to 1.7 μL/cm^2). Blue dye was embedded into the spiral channel layer during device assembly for visualization of the sweat sampling and progression. In comparison to the commercialized sweat collector (Fig. 2.4b), the designed collector is smaller, lighter, fully flexible (without any rigid part), and can stay attached to the skin as a standalone unit sweat collection steps are shown in Fig.2.5.

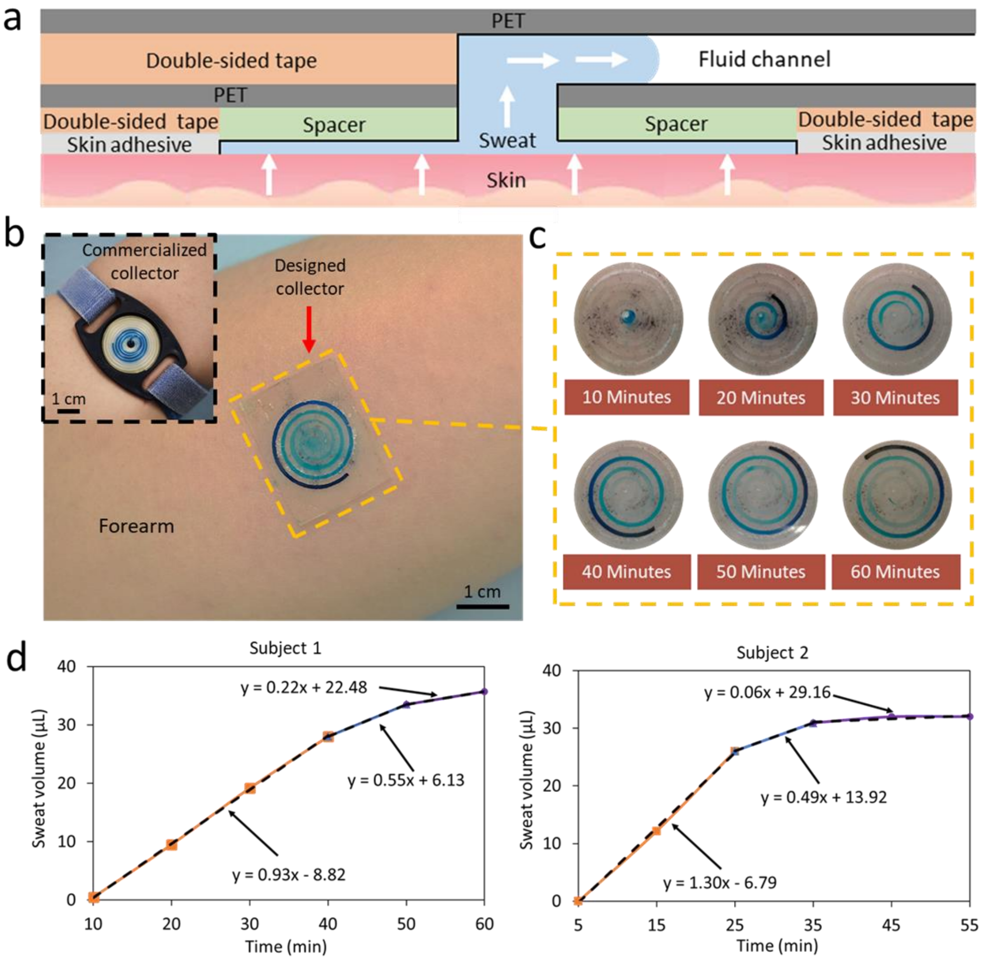
a
PET
Double-sided tape
Fluid channel
PET
Double-sided tape
Spacer
Sweat
Spacer
Double-sided tape
Skin adhesive
Skin adhesive
Skin
b
Commercialized collector
1 cm
Designed collector
Forearm
1 cm
c
10 Minutes
20 Minutes
30 Minutes
40 Minutes
50 Minutes
60 Minutes
d
Subject 1
Sweat volume (μL)
Time (min)
0
10
20
30
40
10
20
30
40
50
60
y = 0.22x + 22.48
y = 0.55x + 6.13
y = 0.93x - 8.82
Subject 2
Sweat volume (μL)
Time (min)
0
10
20
30
40
5
15
25
35
45
55
y = 0.06x + 29.16
y = 0.49x + 13.92
y = 1.30x - 6.79

Figure 2. 4 *Wearable microfluidic sweat collector: a) Cross-section of the tape-based sweat collector structure; b) On-body application of the collector for sweat sampling, as a standalone unit. Inset shows the commercialized sweat collection device (Macroduct, ELITechGroup, France), which requires straps for holding down the device; c) Sequential optical images of the sweat secretion and in-situ collection in the designed sweat collector; d) Measured sweat volume vs. time profiles for two subjects (the sweat secretion rate is inferred from the slope of the curve-fitted lines at the desired time-points).*

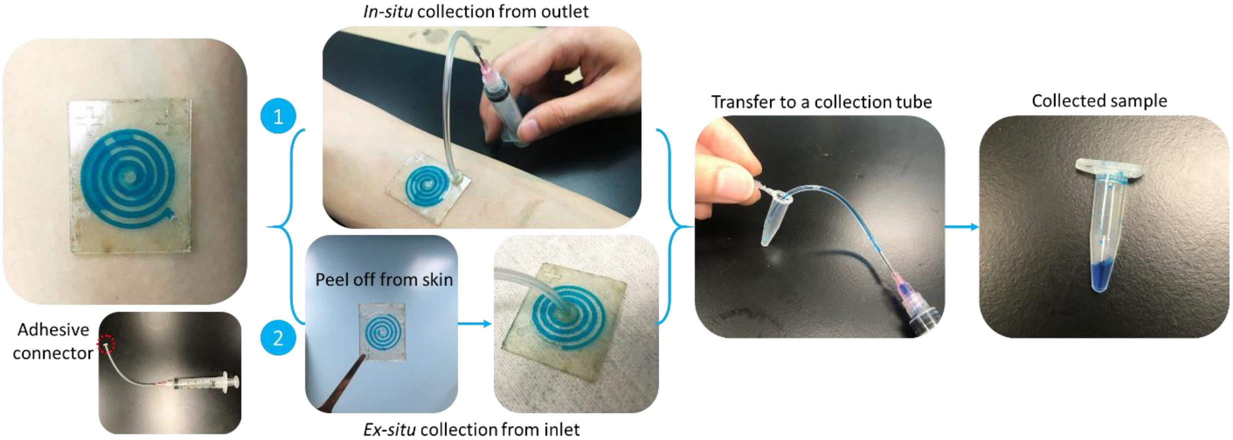
In-situ collection from outlet
1
2
Adhesive connector
Peel off from skin
Ex-situ collection from inlet
Transfer to a collection tube
Collected sample

Figure 2. 5 *Demonstration of two sweat sample collection and transfer processes with the aid of the sweat collection device and a syringe with an adhesive-connector: 1) In-situ collection directly from the device while it is attached on-body. 2) Ex-situ collection with the device after removed from the body.*

To validate the robustness of sweat sampling on-body, the sweat collector was placed on an iontophoretically-stimulated area of the volar surface of the forearm of human subjects (two subjects, following standard iontophoresis protocol for sweat gland stimulation [12]).

Figure 2.4c demonstrates our device’s capability to reliably harvest sweat (no leakage in any of the composed layers) and to visualize the secretion process. To conduct the sweat rate measurement test, first, the volar surface of the forearm of the subject was cleaned with Isopropyl alcohol (IPA, Thermo Fisher Scientific Inc, USA), then stimulated with iontophoresis (ITP, ELITechGroup, France) to induce sweat following the standard protocol [12]. Next, the sweat collector was securely placed on the stimulated area. The complete process of sweat filling the spiral channel can be optically tracked through imaging. The real-time volume of the secreted sweat in the channel was determined based on the designed geometry (Archimedean Spiral: $r = a + b\theta$, where r and θ are polar coordinates, and $a = 1.1\ mm$ and $b = \frac{1}{\pi}\ mm$, as per our design). Sweat rate information can be inferred by calculating the slope of the sweat volume *vs.* time curve at the desired time-point. As shown in Fig. 2.4d, for both subjects, the sweat secretion began at a maximal constant rate, followed by a decreasing trend with time.

2.1.4 References

1. Koh, A. et al. A soft, wearable microfluidic device for the capture, storage, and colorimetric sensing of sweat. Science Translational Medicine vol. 8 366ra165–366ra165 (2016).
2. Choi, J. et al. Soft, skin-mounted microfluidic systems for measuring secretory fluidic pressures generated at the surface of the skin by eccrine sweat glands. Lab on a Chip vol. 17 2572–2580 (2017).
3. Kim, S. B. et al. Super-Absorbent Polymer Valves and Colorimetric Chemistries for Time-Sequenced Discrete Sampling and Chloride Analysis of Sweat via Skin-Mounted Soft Microfluidics. Small vol. 14 1703334 (2018).
4. Nath, P. et al. Rapid prototyping of robust and versatile microfluidic components using adhesive transfer tapes. Lab on a Chip vol. 10 2286 (2010).
5. Walsh, D. I., Kong, D. S., Murthy, S. K. & Carr, P. A. Enabling Microfluidics: from Clean Rooms to Makerspaces. Trends in Biotechnology vol. 35 383–392 (2017).
6. Kundu, A., Ausaf, T. & Rajaraman, S. 3D Printing, Ink Casting and Micromachined Lamination (3D PICLμM): A Makerspace Approach to the Fabrication of Biological Microdevices. Micromachines vol. 9 85 (2018).
7. Martín, A. et al. Epidermal Microfluidic Electrochemical Detection System: Enhanced Sweat Sampling and Metabolite Detection. ACS Sensors vol. 2 1860–1868 (2017).

8. Choi, J. et al. Soft, Skin-Integrated Multifunctional Microfluidic Systems for Accurate Colorimetric Analysis of Sweat Biomarkers and Temperature. ACS Sensors vol. 4 379–388 (2019).
9. Zhang, Y. et al. Passive sweat collection and colorimetric analysis of biomarkers relevant to kidney disorders using a soft microfluidic system. Lab on a Chip vol. 19 1545–1555 (2019).
10. Duffy, D. C., Cooper McDonald, J., Schueller, O. J. A. & Whitesides, G. M. Rapid Prototyping of Microfluidic Systems in Poly(dimethylsiloxane). Analytical Chemistry vol. 70 4974–4984 (1998).
11. Qin, D., Xia, Y. & Whitesides, G. M. Soft lithography for micro- and nanoscale patterning. Nature Protocols vol. 5 491–502 (2010).
12. Sample Collection, Transport and Storage. Quantitative Chromatographic Analysis (2000) doi:10.1201/9780203910788.ch2.

2.2 Wearable biofluid management

2.2.1 Introduction

Previously reported wearable microfluidic biomarker sensors successfully demonstrated electrochemical and colorimetric sensing interfaces for the on-body detection of analytes [1-3]. These sensors rely on the analysis of biofluid samples that are passively collected in predefined microfluidic structures to minimize evaporation [4-8]. Their lack of active control on biofluid flow fundamentally renders them 1) susceptible to operationally relevant confounders such as flow rate variability, 2) incapable of performing diverse bioanalytical operations (*e.g.*, incubation), and 3) incapable of delivering programmable biofluid management functionalities (*e.g.*, biofluid routing and compartmentalization) that are critical to the operational autonomy of the envisioned systems, such as capturing biomarker readings at contextually-relevant timepoints.

To this end, valving is fundamental to active biofluid management, because it enables flow control. The significance of valving has already been demonstrated in microfluidic-based lab-on-a-chip platforms [9-12]. Specifically, programmable valving systems delivered active manipulation and control of small-scale (~nano/microliter) fluid flow within networks of microfluidic channels, forming separated compartments to perform biochemical reactions in an addressable manner [13-15]. Such valving systems were positioned to execute synchronous/asynchronous sequential and parallel fluid manipulation tasks autonomously, leading to the creation of new microfluidic solutions for various applications including diagnostics and -omics [16,17]. To date, such programmable valving systems have not been adapted for integration into lab-on-the-body-like wearable platforms, which is primarily due to the bulkiness of the actuation instruments [18] (*e.g.*, external mechanical pumps and optical excitation systems). Recently, in the context of wearable platforms, valving interfaces—embedded within sophisticated flexible epidermal microfluidic configurations—were reported, which successfully demonstrated on-body biofluid routing, but they were either passive or required manual mechanical activation [19-21].

To render active biofluid management in a wearable format, here, we devise an electronically-programmable microfluidic valving system, which is capable of biofluid sampling, routing, and compartmentalization for biomarker analysis. The core of the microfluidic system is a network of individually-addressable microheater-controlled thermo-responsive poly(N-isopropylacrylamide) (PNIPAM) hydrogel valves. To realize this system, we devise a simple, high-throughput, and low-cost fabrication scheme to develop hydrogel arrays on a tape-based flexible substrate. The fabricated hydrogel arrays can be incorporated within a 3D flexible microfluidic module, following an extensible vertical integration scheme, which allows for the assembly of microfluidic embodiments and actuation/sensing electrode arrays within a compact footprint. To adapt the valving system for on-body biofluid harvesting, specifically, in the context of interfacing with pressure-driven bio-interfaces (*e.g.*, sweat glands), a pressure regulation mechanism is devised, informed by an electronic-hydraulic analogy.

The active fluid control achieved by this system is harnessed to create new wearable bioanalytical capabilities at system levels which is leveraged to render addressable biofluid routing and compartmentalization. These capabilities can be positioned to render context-based sensor selection/protection, where the mode of analysis will be selected depending on the user's need, behavior, and activity.

2.2.2 Operational principles of the wearable valving system

Figure 2.6a illustrates a representative pressure-regulated six-compartment valving system—with a sweat collection inlet at the center and an electrochemical sensing interface within each compartment—interfacing a wireless flexible circuit board to form a fully-integrated wearable bioanalytical platform. To construct the valve, we specifically use a PNIPAM-based hydrogel (Fig. 2.6b and Fig. 2.7a, synthesized from a NIPAM monomer and N,N′-methylenebis(acrylamide), BIS crosslinker), which significantly shrinks/expands in response to local temperature increments/decrements, above/below its lower critical solution temperature (LCST) [22]. By embedding this hydrogel within a microfluidic channel, the volumetric thermal responsiveness of the hydrogel can be exploited to effectively permit/block fluid flow via activation/deactivation of the heater. Previous efforts have already demonstrated the utility of thermo-responsive hydrogel-based valving for controlling fluid flow within conventional lab-on-a-chip devices [9,10,14,18]. However, they required manually-operated and bulky external instrumentation to actuate the hydrogels, preventing their translation into wearable platforms. Here, we devised a circuit-controlled micropatterned heater (on a flexible substrate) to actuate the hydrogels. In this way, we formed a miniaturized programmable valve, which can be extended into an addressable array, and subsequently, exploited to realize a valve-gated multicompartment bioanalytical platform amenable for wearable applications.

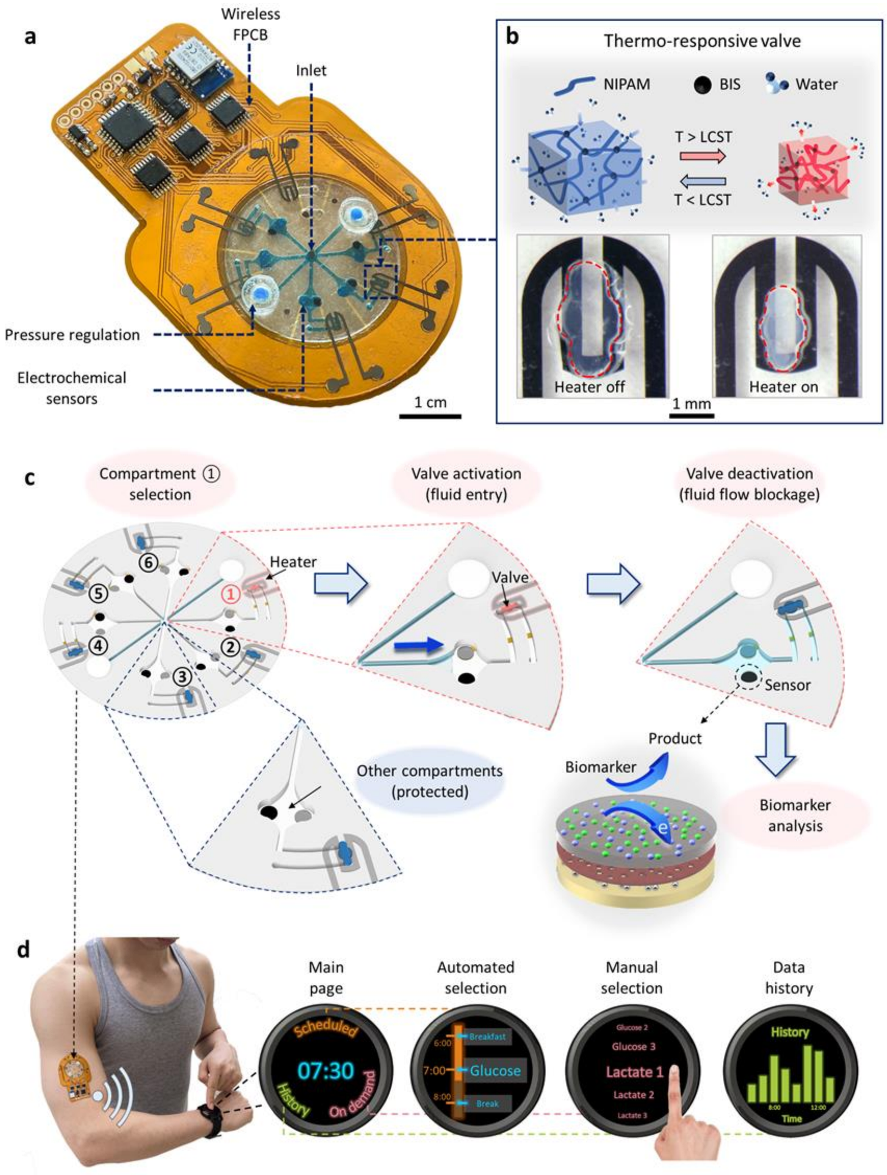
a
Wireless FPCB
Inlet
Pressure regulation
Electrochemical sensors
1 cm
b
Thermo-responsive valve
NIPAM
BIS
Water
T > LCST
T < LCST
Heater off
Heater on
1 mm
c
Compartment ① selection
Valve activation (fluid entry)
Valve deactivation (fluid flow blockage)
Heater
Valve
Sensor
Product
Biomarker
Other compartments (protected)
Biomarker analysis
d
Main page
Automated selection
Manual selection
Data history
Scheduled
07:30
History
On demand
6:00
7:00
8:00
Breakfast
Glucose
Break
Glucose 2
Glucose 3
Lactate 1
Lactate 2
Lactate 3
History
Time

__Figure 2. 6__ A fully-integrated wearable valving system (concept and operational principle). a) Illustration of a representative wearable bioanalytical platform, consisting of an integrated programmable microfluidic valving system interfacing a FPCB; b) Illustration of PNIPAM hydrogel shrinkage/expansion in response to temperature change above/below its LCST (induced by activation/deactivation of the microheater); c) A schematic operation example of the programmable microfluidic valving system, demonstrating biofluid routing, compartmentalization, and analysis in the selected compartment and sensor protection in the non-selected compartments; d) Illustration of control commands (automated and manual) communication for scheduled and on-demand biomarker data acquisition with the aid of user interfaces preloaded on smart consumer electronics.

An example operation of our valving system is shown in Fig. 2.6c. In this example, the valve (downstream of the microfluidic channel) in compartment 1 is first activated (while others remain deactivated) to route and sample biofluid. Then, it is deactivated to block the flow, allowing for biofluid compartmentalization and analysis (using an electrochemical sensor positioned upstream of the channel). Accordingly, sample analysis can be performed—without the confounding influence of flow rate variability—by the sensor(s) in the addressed compartment, while the sensors in the other compartments remain protected.

This addressable compartmentalization capability can be exploited to take biomarker readings at scheduled/on-demand timepoints, thus enabling contextual biomarker analysis. In the presented wearable bioanalytical platform, valve activation and sensor output signal processing are delivered with the aid of a circuit board, which is equipped with a multi-channel programmable current source and analog front-end circuits. Through bilateral Bluetooth communication with personal smart electronics (e.g., smartwatch), preloaded with a custom-designed user interface, biomarker data acquisition timepoints (pre-scheduled/on-demand) can be programmed (via automated/manual commands) and biomarker data can be displayed in real-time (Fig. 2.6d).

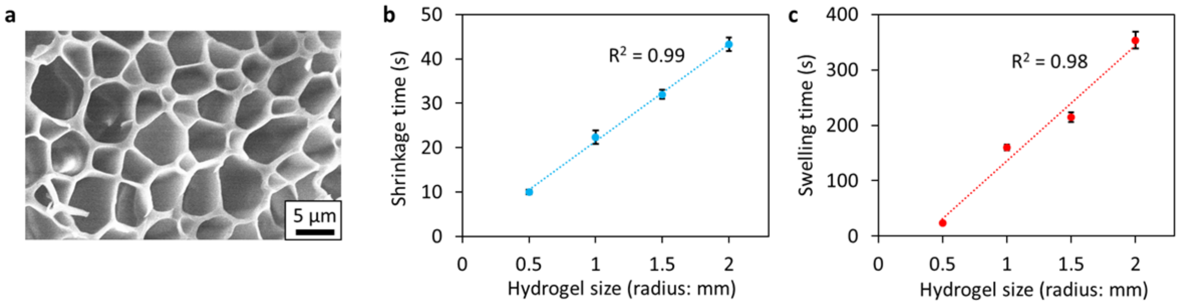

Figure 2. 7 *a) An illustrative Scanning Electron Microscopy (SEM) of a freeze-dried hydrogel with 4% BIS (imaged once). The features are consistent with previously reported observations3; b,c) Characterization of the hydrogel volume transition time vs hydrogel size upon activation/deactivation of the microheater for shrinkage (b) and swelling (c). Shrinkage and swelling times are defined as the time it takes for the hydrogel shrinkage/expansion to settle within*

1% of its steady-state volume upon (activation/deactivation of the microheater). Error bars, mean ± s.e (n = 3 measurements from different hydrogels).

2.2.3 Wearable valve-gated microfluidic networks

For fluid valving, ideally, a binary off/on valve operation is desired, where fluid flow is completely blocked with no leakage in the off-state (when the valve is deactivated), and fluid flow is permitted in the on-state (when the valve is activated). In the context of our thermo-responsive PNIPAM-based hydrogel, off/on transition is achieved upon decreasing/increasing the temperature below/above the LCST. The thermo-responsive property of PNIPAM stems from the coexistence of hydrophilic amide and hydrophobic propyl groups within its polymer structure [23]. When the hydrogel's temperature is lower than its LCST, the hydrogen-bonding interactions between the amide group and the water molecules are dominant. Therefore, the hydrogel becomes highly hydrated, leading to its structural expansion. Conversely, when the hydrogel's temperature is higher than its LCST, the hydrogen-bonding interactions become weaker and the interactions between the hydrophobic propyl group and the water molecules are dominant. As a result, the water is released from the hydrogel structure, leading to hydrogel shrinkage.

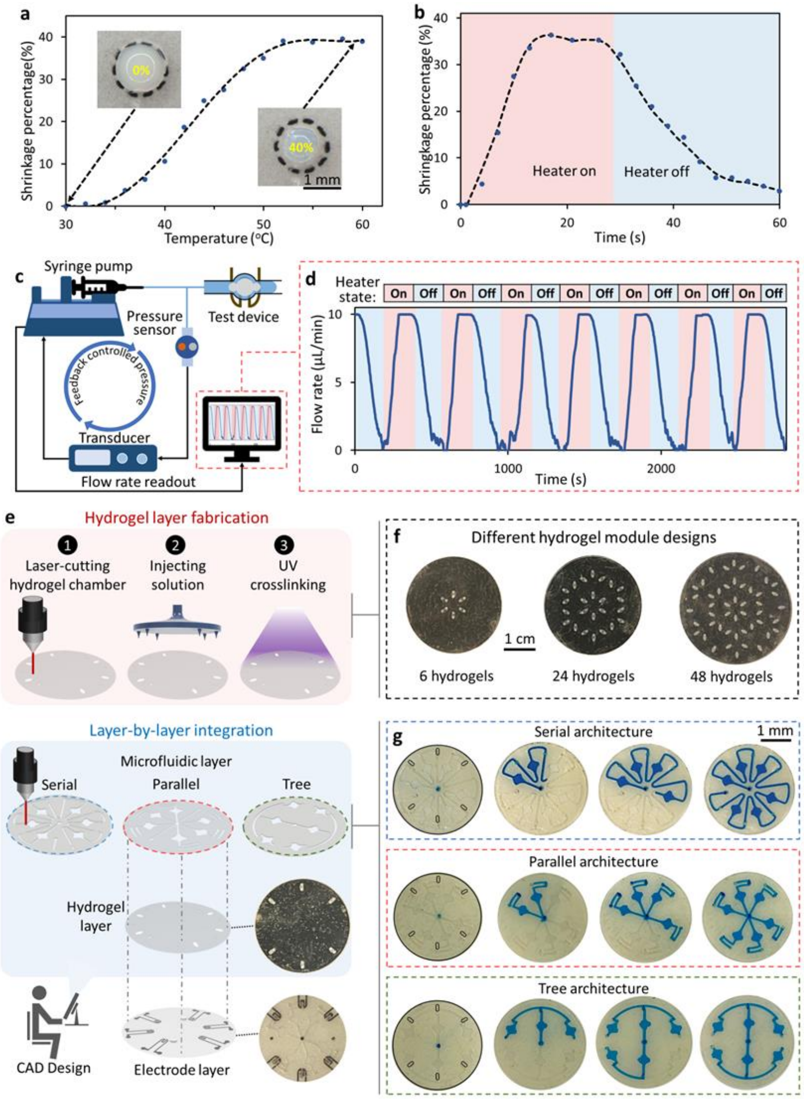
a
Shrinkage percentage(%)
Temperature (°C)
0%
40%
1 mm
b
Shrinkage percentage (%)
Time (s)
Heater on
Heater off
c
Syringe pump
Pressure sensor
Test device
Feedback controlled pressure
Transducer
Flow rate readout
d
Heater state:
On
Off
Flow rate (µL/min)
Time (s)
e
Hydrogel layer fabrication
Laser-cutting hydrogel chamber
Injecting solution
UV crosslinking
Layer-by-layer integration
Microfluidic layer
Serial
Parallel
Tree
Hydrogel layer
CAD Design
Electrode layer
f
Different hydrogel module designs
1 cm
6 hydrogels
24 hydrogels
48 hydrogels
g
Serial architecture
1 mm
Parallel architecture
Tree architecture

Figure 2. 8 *Fabrication and characterization of valve-gated microfluidic networks. a) Standalone PNIPAM hydrogel shrinkage percentage vs. temperature profile (polynomial fitted curve illustrates the trend). Microscopic images of the standalone hydrogel at the annotated temperatures are shown as insets; b) Reversible hydrogel (standalone) volume transition upon activation/deactivation of the microheater (polynomial fitted curve illustrates the trend); c) A microfluidic valving characterization setup with a feedback-controlled pressure configuration; d) The measured flow rate profile through a valve-gated microfluidic channel upon the periodic activation/deactivation of the valve; e) Hydrogel layer fabrication procedure and layer-by-layer device integration scheme to realize microfluidic valving systems with different architectures; f) Optical images of the representative fabricated hydrogel layers with different numbers/arrangements of hydrogels (a black substrate background is used to visualize the transparent hydrogel features); g) Sequential optical images of progressive microfluidic routing and compartmentalization through illustrative serial, parallel, and tree microfluidic networks (constructed through integration with the same arrangement of hydrogels).*

For robust on-body valving, the temperature at which the hydrogel's volumetric transition occurs should be sufficiently above the skin temperature (~35 °C), such that the heat transfer from the skin to the valve does not result in significant hydrogel shrinkage and subsequent fluid leakage. By incorporating an ionizable monomer (MAPTAC) in the hydrogel structure [24], the volumetric transition temperature of about 45 °C is achieved. As shown in Fig. 2.8a, the modified PNIPAM-based hydrogel exhibits about 40% shrinkage from its original size (based on the 2D imaged area) after ramping up its temperature above the LCST point. Reversibly, the hydrogel can recover back to its original volume, simply by deactivating the microheater (Fig. 2.8b). The observed asymmetry in the hydrogel shrinkage and recovery rates can be attributed to the difference between the outward and inward diffusion rates of the surrounding buffer solution that is leaving and entering the hydrogel, respectively [25]. Moreover, the corresponding shrinkage and recovery rates are found to be proportional to the hydrogel size as demonstrated in Fig. 2.7b,c. In order to maintain a fast valve responsive time, we minimized the size of the hydrogel embedded inside the channel (circle-shaped with radius < 1 mm). By setting up a pressure-controlled fluid flow configuration (Fig. 2.8c), the flow rate within a hydrogel-embedded and microheater-coupled microfluidic channel was monitored. As shown in Fig. 2.8d, upon deactivation/activation of the microheater, the flow rate within the channel correspondingly dropped to zero/recovered to its default value, illustrating the reversible, consistent, and periodic switching capabilities of the formed valve. The slower transient characteristic of the embedded hydrogel as compared to that of the standalone hydrogel (Fig. 2.8b vs. Fig. 2.8d) can be attributed to the surface contact forces acting on the embedded hydrogel. Furthermore, our device temperature characterization results show that operationally the valve opens at temperatures $\gtrsim 45\ ^{o}$C (Fig. 2.9).

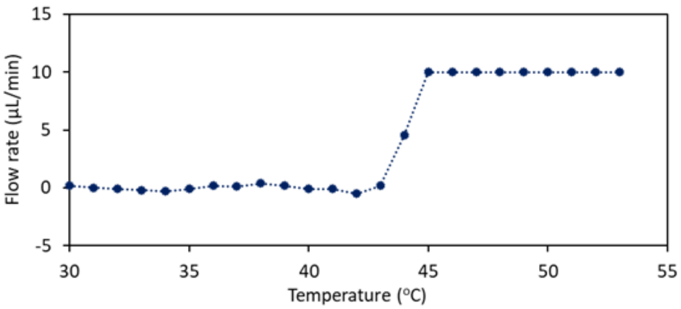

Figure 2. 9 *Flow rate vs. hydrogel valve temperature profile (pressure is set as 15 mmHg). The valve is opened when the temperature exceeds 44 °C. Y-axis indicates the averaged continuous recordings of the flow rate for each temperature condition.*

To fabricate the valve interface in an array format and within a tape-based flexible microfluidic module, a simple and high-throughput fabrication and integration scheme is devised (Fig. 2.8e and Fig. 2.10 and Fig. 2.11). The scheme (Appendix B) involves fabricating the hydrogel array, microfluidic network structure, and electrode array on separate layers, followed by the vertical alignment and assembly of the layers [26]. We particularly positioned the microheater electrode array layer as the top layer (i.e., away from the skin, in which case intermediary layers serve as insulators), to minimize the heat conduction to skin. In our scheme, the hydrogel array and microfluidic network features are defined by a laser-cutter, which can be programmed at a software level to rapidly render various arrangements and dimensions. The hydrogel arrays can be developed by simultaneously injecting PNIPAM precursor solutions into the respective defined features, followed by a one-step ultraviolet crosslinking procedure, altogether rendering the development process low-cost and highly scalable (Fig. 2.8f). Our vertical integration approach also allows the same arrangement of hydrogel arrays to form various microfluidic routing and compartmentalization networks, simply by integrating microfluidic layers with different architectures. For example, as shown in Fig. 2.8g, an arrangement of six hydrogels are used to gate microfluidic networks with serial, parallel, and tree-like architectures (for visualization purposes, a blue dye is embedded within the channels and the hydrogels are externally/locally heated).

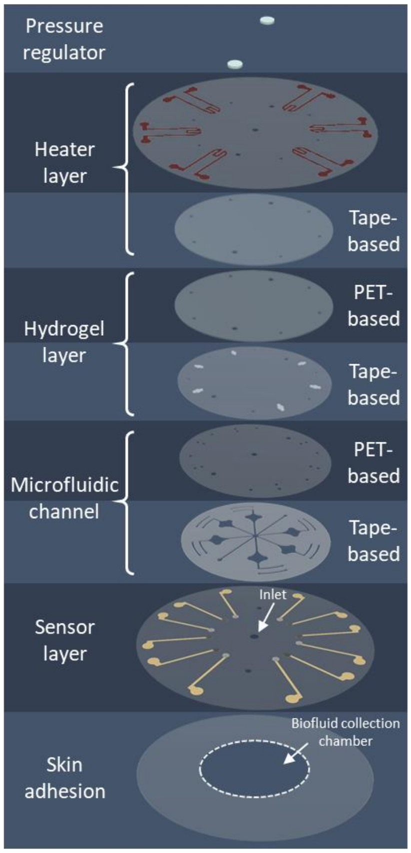
Pressure regulator
Heater layer
Tape-based
Hydrogel layer
PET-based
Tape-based
Microfluidic channel
PET-based
Tape-based
Inlet
Sensor layer
Biofluid collection chamber
Skin adhesion

Figure 2. 10 *Exploded view of the epidermal microfluidic valving system, which is constructed by the vertical integration of pressure regulator/hydrogel embodiments, laser-cut microfluidic channel layers, microheater/sensor array layers, and a double-sided adhesive skin adhesion layer.*

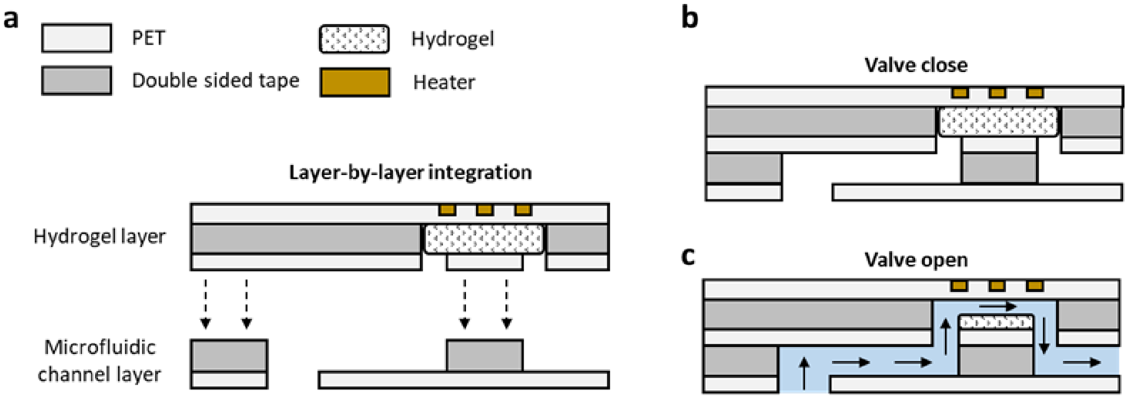
a
PET
Double sided tape
Hydrogel
Heater
Layer-by-layer integration
Hydrogel layer
Microfluidic channel layer
b
Valve close
c
Valve open

Figure 2. 11 *a) Demonstration of the layer-by-layer integration method to form the valve interface; b,c) Illustrations of (b) valve closure when the microheater is off, and (c) valve opening when the* *microheater is on. Microheater activation causes hydrogel shrinkage, allowing incoming biofluid to travel through the channel.*

2.2.4 Active biofluid sampling from pressure-driven sources

In order to adapt the demonstrated valving operation to actively sample, route, and compartmentalize epidermally retrievable biofluids from pressure-driven sources, pressure release mechanisms are necessary. Specifically, in the context of sweat as the target biofluid, a pressure release mechanism is devised to avoid excess pressure build-up from the sweat glands. Without such mechanism in place, valve breakage would occur, due to the high pressure caused by the accumulated sweat (as high as ~500 mmHg with an air-tight sealed interface) [27]. The problem at hand can be formulated with the aid of an electrical circuit-hydraulic analogy (Fig. 2.12a), involving a current source (delivering current level IS) and a transistor switch. Here, the minimum turn-on voltage for the transistor switch is denoted as V_{min} and its maximum tolerable voltage is denoted as V_{max} (corresponding to its breakdown voltage). When directly connecting the transistor (in its off mode) to the current source, the built-up high voltage difference across the transistor (V) inevitably leads to transistor breakdown ($> V_{max}$). Similarly, as shown in Fig. 3b (left), when directly interfacing the air-tight closed valve (microfluidic transistor switch) with actively secreting sweat glands (with secretion rate Q_S), the built-up high-pressure difference (P) across the valve inevitably leads to the valve breakage ($P > P_{max}$, where P_{max} denotes the valve's maximum tolerable pressure).

In both scenarios, the addition of a secondary parallel electric/hydraulic conductive path allows for redirecting the electrical current/fluid flow as a relief mechanism (Fig. 2.12b, center). However, the electric/hydraulic resistance of these paths must be tuned to ensure that the voltage/pressure across the respective switches is maintained above V_{min}/P_{min} (where the switches are turned on). Electrically, this can be achieved by adding a parallel resistor (R_e). Hydraulically, here, we use a membrane filter incorporated within an auxiliary microfluidic channel to render the desired hydraulic resistance, which effectively serves as a pressure regulation mechanism (Fig. 2.12b right and Fig. 2.12c).

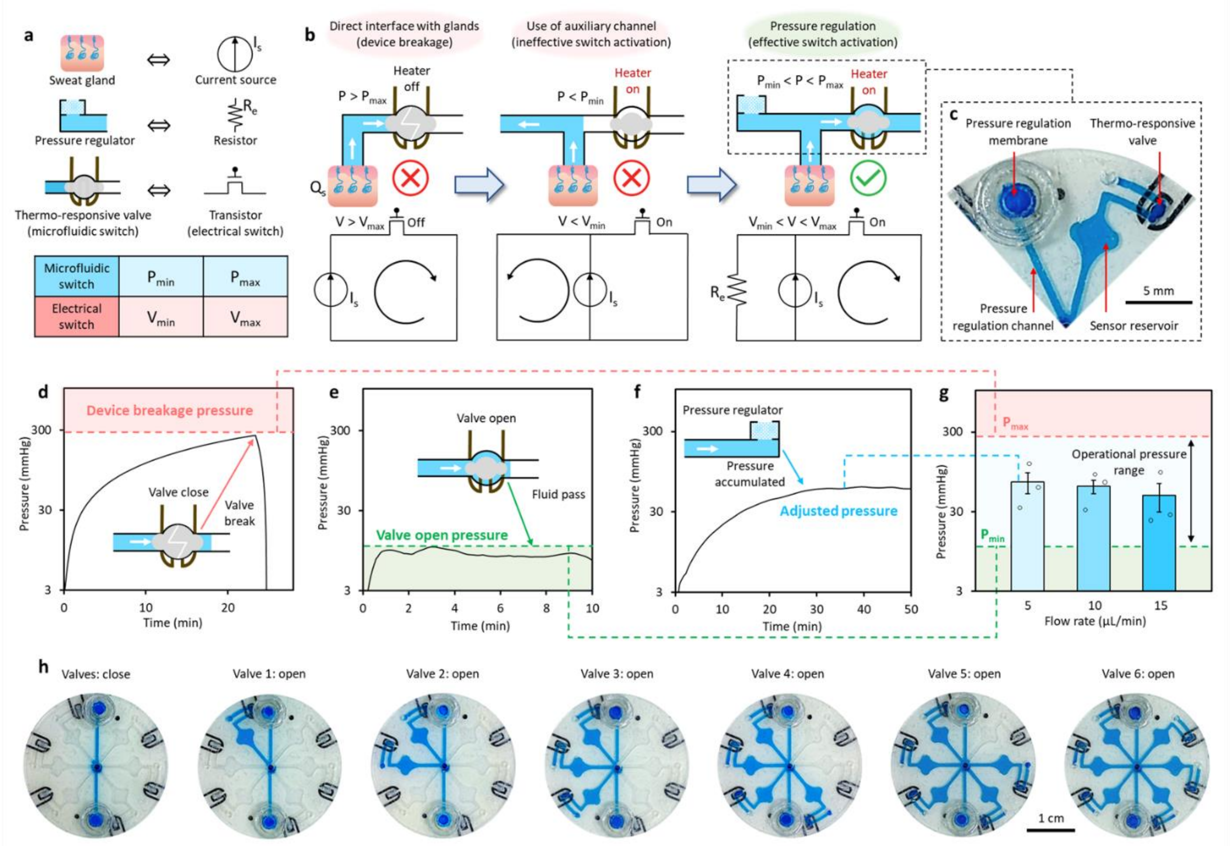

a
Sweat gland
⇔
Current source
I_s
Pressure regulator
⇔
Resistor
R_e
Thermo-responsive valve (microfluidic switch)
⇔
Transistor (electrical switch)
Microfluidic switch
P_{min}
P_{max}
Electrical switch
V_{min}
V_{max}
b
Direct interface with glands (device breakage)
Use of auxiliary channel (ineffective switch activation)
Pressure regulation (effective switch activation)
Heater off
$P > P_{max}$
Heater on
$P < P_{min}$
$P_{min} < P < P_{max}$
Heater on
Q_s
$V > V_{max}$ Off
$V < V_{min}$ On
$V_{min} < V < V_{max}$ On
I_s
R_e
c
Pressure regulation membrane
Thermo-responsive valve
5 mm
Pressure regulation channel
Sensor reservoir
d
Device breakage pressure
Pressure (mmHg)
300
30
3
Valve close
Valve break
0
10
20
Time (min)
e
Valve open
Fluid pass
Valve open pressure
Pressure (mmHg)
0
2
4
6
8
10
Time (min)
f
Pressure regulator
Pressure accumulated
Adjusted pressure
Pressure (mmHg)
0
10
20
30
40
50
Time (min)
g
P_{max}
Operational pressure range
P_{min}
Pressure (mmHg)
5
10
15
Flow rate (μL/min)
h
Valves: close
Valve 1: open
Valve 2: open
Valve 3: open
Valve 4: open
Valve 5: open
Valve 6: open
1 cm

***Figure 2. 12** Elaboration, characterization, and demonstration of pressure regulated-valving. a) An electric-hydraulic analogy. (V_{min}: minimum turn-on voltage of the transistor switch; Vmax: maximum tolerable voltage of the transistor switch; P_{min}: minimum required pressure to open the valve; P_{max}: maximum tolerable pressure of the hydraulic valve); b) Design rationale of the pressure regulation mechanism (assisted by the electrical circuit analogy); c) Optical image of the implemented pressure regulated valve; d-f) Real-time pressure recording for the characterization of the (d) maximum tolerable pressure, (e) minimum required pressure, and (f) regulated pressure. Input flow rate was set to 5 μL min^{-1}; g) Characterized accumulated pressure across pressure regulated-microfluidic channels at different flow rates. Error bars, mean ± s.e (n = 3 measurements from different devices); h) Sequential optical images of progressive microfluidic routing and compartmentalization through an illustrative pressure-regulated six-compartment valving system (performed ex-situ).*

To characterize P_{max} and P_{min} for our pressure regulated valving interface, the same setup as that of Fig. 2.8c is used (with a programmed input flow rate of 5 μL min^{-1}). As shown in Fig. 2.12d, the direct injection of fluid through the closed-valve microfluidic device (using a syringe pump) resulted in pressure built-up on the order of 300 mmHg (corresponding to P_{max}), beyond which the device failed (due to leakage), as evident from the annotated drop in the measured pressure. Furthermore, the injection of fluid through the opened-valve microfluidic device resulted in approximately 10 mmHg pressure (corresponding to P_{min}) across the device (Fig. 2.12e). Characterization of a microfluidic pathway, with the pressure regulation mechanism in place (Fig. 2.12f), illustrates the mechanism's ability to effectively maintain the operational pressure (P) within the permissible pressure range ($P_{min} < P < P_{max}$, Fig. 2.13) for different input flow rates (Fig. 2.12g). In addition, Fig. 2.12h shows that a fully formed valving system (consisting of heater-coupled hydrogel valves and pressure regulating embodiments) can be successfully used to route and compartmentalize fluid in an addressable and electronically programmable manner.

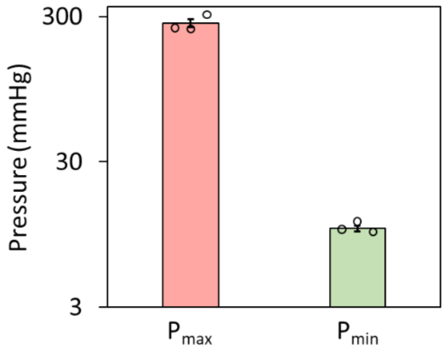

Figure 2. 13 *Characterization of the maximum tolerable pressure (P_{max}) and minimum required pressure (P_{min}). Error bars, mean ± s.e (n = 3 measurements from different devices).*

2.2.5 References

1. Gao, W. et al. Fully integrated wearable sensor arrays for multiplexed in situ perspiration analysis. Nature 529, 509–514 (2016).

2. Emaminejad, S. et al. Autonomous sweat extraction and analysis applied to cystic fibrosis and glucose monitoring using a fully integrated wearable platform. Proc. Natl Acad. Sci. USA 114, 4625–4630 (2017).
3. Imani, S. et al. A wearable chemical–electrophysiological hybrid biosensing system for real-time health and fitness monitoring. Nat. Commun. 7, 1–7 (2016).
4. Koh, A. et al. A soft, wearable microfluidic device for the capture, storage, and colorimetric sensing of sweat. Sci. Transl. Med. 8, 366ra165 (2016).
5. Kim, J., Campbell, A. S., de Ávila, B. E.-F. & Wang, J. Wearable biosensors for healthcare monitoring. Nat. Biotechnol. 37, 389–406 (2019).
6. Martín, A. et al. Epidermal microfluidic electrochemical detection system: enhanced sweat sampling and metabolite detection. ACS Sens. 2, 1860–1868 (2017).
7. Mostafalu, P. et al. A toolkit of thread-based microfluidics, sensors, and electronics for 3D tissue embedding for medical diagnostics. Microsyst. Nanoeng. 2, 16039 (2016).
8. Bandodkar, A. J. et al. Battery-free, skin-interfaced microfluidic/electronic systems for simultaneous electrochemical, colorimetric, and volumetric analysis of sweat. Sci. Adv. 5, eaav3294 (2019).
9. Thorsen, T., Maerkl, S. J. & Quake, S. R. Microfluidic large-scale integration. Science 298, 580–584 (2002).
10. Unger, M. A., Chou, H.-P., Thorsen, T., Scherer, A. & Quake, S. R. Monolithic microfabricated valves and pumps by multilayer soft lithography. Science 288, 113–116 (2000).

11. Haefner, S., Koerbitz, R., Frank, P., Elstner, M. & Richter, A. High integration of microfluidic circuits based on hydrogel valves for MEMS control. Adv. Mater. Technol. 3, 1700108 (2018).
12. Greiner, R., Allerdissen, M., Voigt, A. & Richter, A. Fluidic microchemomechanical integrated circuits processing chemical information. Lab Chip 12, 5034–5044 (2012).
13. Beebe, D. J. et al. Functional hydrogel structures for autonomous flow control inside microfluidic channels. Nature 404, 588–590 (2000).
14. Brower, K. et al. An open-source, programmable pneumatic setup for operation and automated control of single-and multi-layer microfluidic devices. HardwareX 3, 117–134 (2018).
15. Chen, C.-F., Liu, J., Chang, C.-C. & DeVoe, D. L. High-pressure on-chip mechanical valves for thermoplastic microfluidic devices. Lab Chip 9, 3511–3516 (2009).
16. Deng, Y., Finck, A. & Fan, R. Single-cell omics analyses enabled by microchip technologies. Annu. Rev. Biomed. Eng. 21, 365–393 (2019).
17. Szulwach, K. E. et al. Single-cell genetic analysis using automated microfluidics to resolve somatic mosaicism. PloS One 10, e0135007 (2015).
18. Haefner, S., Koerbitz, R., Frank, P., Elstner, M. & Richter, A. High integration of microfluidic circuits based on hydrogel valves for MEMS. Control. Adv. Mater. Technol. 3, 1700108 (2018).
19. Choi, J., Kang, D., Han, S., Kim, S. B. & Rogers, J. A. Thin, soft, skin-mounted microfluidic networks with capillary bursting valves for chrono-sampling of sweat. Adv. Healthc. Mater. 6, 1601355 (2017).

20. Reeder, J. T. et al. Resettable skin interfaced microfluidic sweat collection devices with chemesthetic hydration feedback. Nat. Commun. 10, 1–12 (2019).
21. Kim, S. B. et al. Super-absorbent polymer valves and colorimetric chemistries for time-sequenced discrete sampling and chloride analysis of sweat via skin-mounted soft microfluidics. *Small* **14**, 1703334 (2018).
22. Taylor, L. D. & Cerankowski, L. D. Preparation of films exhibiting a balanced temperature dependence to permeation by aqueous solutions—a study of lower consolute behavior. J. Polym. Sci. A Polym. Chem. 13, 2551–2570 (1975).
23. Haq, M. A., Su, Y. & Wang, D. Mechanical properties of PNIPAM based hydrogels: a review. Mater. Sci. Eng. C. 70, 842–855 (2017).
24. Dong, L., Agarwal, A. K., Beebe, D. J. & Jiang, H. Variable-focus liquid microlenses and microlens arrays actuated by thermoresponsive hydrogels. Adv. Mater. 19, 401–405 (2007).
25. Harmon, M. E., Tang, M. & Frank, C. W. A microfluidic actuator based on thermoresponsive hydrogels. Polymer 44, 4547–4556 (2003).
26. Lin, H. et al. A rapid and low-cost fabrication and integration scheme to render 3D microfluidic architectures for wearable biofluid sampling, manipulation, and sensing. Lab Chip 19, 2844–2853 (2019).
27. Sonner, Z. et al. The microfluidics of the eccrine sweat gland, including biomarker partitioning, transport, and biosensing implications. Biomicrofluidics 9, 031301 (2015).

2.3 Wearable biofluid processing

2.3.1 Introduction

The conventional passive control of fluid not only limits their fluid management capabilities, it also inherently limits their analytical processing operations. As previously shown in the context of lab-on-a-chip devices, active fluidic control (*e.g.*, mixing) can create new degrees of freedom for the implementation of auxiliary sample processing operations to realize a broad range of assays in order to target a diverse set of biomarkers [1-4]. Such assays can in principle be adapted for wearable biomarker analysis by exploiting the readily small footprint of their transduction interfaces. However, the challenge remains in creating active biofluid processing capabilities that can be performed in a wearable format.

To this end, electrofluidic-based actuation techniques are suitable, given their miniaturized interface and electronic programmability [5-11]. In that regard, two main problems need to be addressed: 1) devising a durable, corrosion-resistant and flexible electrofluidic interface, which can reliably perform actuation in biofluidic conditions and 2) developing a wearable and battery-powered control electronic circuitry that can deliver the required excitation voltage levels at relatively high frequencies (~ in MHz range). The latter, essentially, necessitates miniaturization of bulky and power outlet-connected excitation instruments, which are used by conventional lab-on-a-chip-based platforms to perform electrofluidic actuation [12].

Here, we particularly exploit the alternating current electrothermal (ACET) flow phenomenon to render on-demand, programmable, and precise microfluidic actuation. ACET-based actuation techniques have been proven to be effective in manipulating microfluidics with high conductivity [6-8] (*e.g.*, biofluids). Alternative electro-fluidic flow actuation techniques such as AC electroosmosis (ACEO) [11] and electrowetting-on-dielectric (EWOD) [13,14] may not be suitable for wearable applications due to their stringent requirements for low-conductive fluids and/or high operation voltages.

To realize wearable ACET actuation, we fabricated and embedded flexible electrode configurations within a microfluidic device, and custom-developed a wirelessly programmable high frequency (MHz) excitation circuitry. The performance of the ACET electrode configurations were characterized in relation to the induced flow profiles, and a representative on-body actuation operation was validated through human subject testing with our wearable actuation system.

2.3.2 Operational principles of wearable ACET actuation

ACET flow arises in the presence of a temperature gradient induced by a non-uniform electric field. By applying an AC voltage across a pair of coplanar electrodes, a non-uniform electric field $\mathbf{E}$ (magnitude represented as E) is established, which results in a temperature gradient profile (∇T) inside the microfluidic channel (Fig. 2.14a,b). This temperature gradient correspondingly produces gradients in permittivity ($\boldsymbol{\nabla}\varepsilon = (\partial\varepsilon/\partial T)\boldsymbol{\nabla}T$) and conductivity ($\boldsymbol{\nabla}\sigma = (\partial\sigma/\partial T)\boldsymbol{\nabla}T$)). The interaction of the electric field with these gradient profiles results in a body force ($\mathbf{f}_\mathrm{E}$) acting on the fluid, governed by the equation (Appendix C, [6]):

$$\mathbf{f}_\mathrm{E} = [\frac{\sigma_0\boldsymbol{\nabla}\varepsilon - \varepsilon_0\boldsymbol{\nabla}\sigma}{\sigma_0 + i\omega\varepsilon_0} \cdot \mathbf{E}_0]\mathbf{E}_0 - \frac{1}{2}E_0^2\boldsymbol{\nabla}\varepsilon \quad (1)$$

, where subscript 0 describes the physical variable at a spatially constant temperature (*e.g.*, $\mathbf{E}_0$ is the electric field at a spatially constant temperature, $T = T_0$). The generated body force induces fluid motion (Fig. 2.14c) with a velocity that is proportional to $E_0^2\nabla T$ (as described supplementary materials). In this case, since ∇T is induced by the electric field (where $\nabla T \propto E^2$), the velocity becomes proportional to E^4, or the 4th power of the applied voltage. To exploit the ACET flow phenomenon for inducing a net flow, asymmetric configurations can be utilized. As conceptualized in Fig. 14 and Fig. 2.15a,b, by changing the symmetric ACET electrode design to an asymmetric configuration, imbalanced electric and temperature field profiles can be generated, which in turn leads to breaking the symmetry of competitive flow vortices and inducing a net flow (Fig. 2.15a,b).

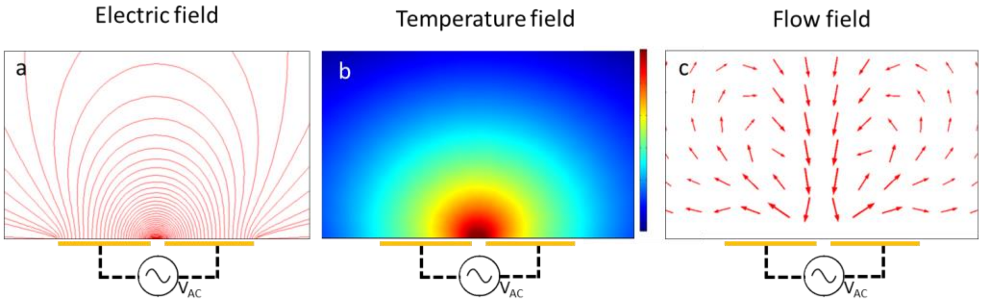
Electric field
Temperature field
Flow field
a
b
c
V_{AC}
V_{AC}
V_{AC}

Figure 2. 14 *Conceptual illustrations of the a) ACET-based electric field, b) temperature field , and c) flow field profiles, generated by equally-sized coplanar pair of electrodes.*

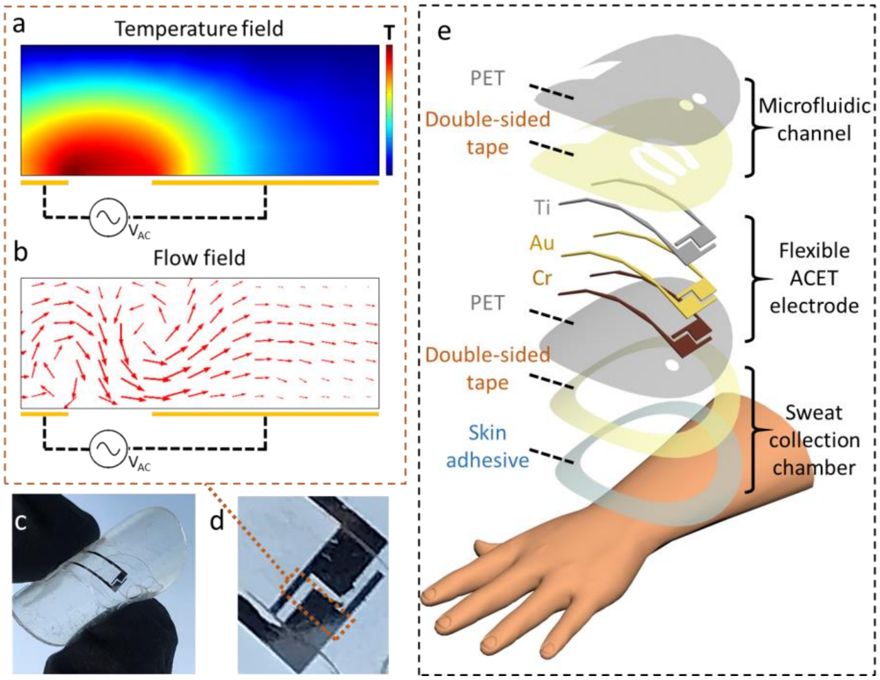
a
Temperature field
T
V_{AC}
b
Flow field
V_{AC}
c
d
e
PET
Double-sided tape
Microfluidic channel
Ti
Au
Cr
PET
Flexible ACET electrode
Double-sided tape
Skin adhesive
Sweat collection chamber

Figure 2. 15 *Wearable ACET actuation: a,b) Conceptual illustrations of the ACET-induced temperature (a) and flow field (b) profiles, generated by an asymmetric coplanar pair of electrodes; c,d) Epidermal microfluidic device with an embedded ACET electrode pair; e) Exploded view of the epidermal microfluidic device structure.*

To realize ACET flow within a wearable electrofluidic actuation platform, a flexible tape-based epidermal microfluidic device is developed (Fig. 2.15c, d). The ACET electrodes are patterned onto a flexible polyethylene terephthalate (PET) substrate and incorporated into a tape-based flexible microfluidic device (Fig. 2.15e). The electrode layers are fabricated by deposition and patterning of 20 nm Cr (for metal adhesion), 100 nm Au, and 20 nm Ti. The incorporation of the Ti layer was to realize a biofluid-facing electrolysis-resistant layer to ensure long-term and stable operation. The microfluidic system is constructed by stacking layers of laser-patterned double-sided tape (forming the microfluidic channel) on the ACET electrode-patterned PET substrate, followed by a PET ceiling to seal the device. To further avoid electrolysis and to bypass the double layer capacitance formed at the interface of the electrode-biofluid [8], the electrodes are excited with an AC voltage source at a sufficiently high frequency (8 MHz).

2.3.3 ACET pumping

To verify the ACET actuation phenomenon, two configurations of asymmetric electrodes are devised, which induce directional fluid flow, and allow for characterizing their velocity profiles in response to the excitation voltage levels. The first configuration is based on a previously reported asymmetric parallel electrode pair consisting of a narrow electrode (width: 40 μm) and a wide electrode (width: 90 μm), separated by 10 μm (Fig. 2.16a, c) [6]. In that regard, it is postulated that the wide electrode has a larger effective area of fluid induction compared to the narrow electrode, thus driving the direction of the flow. The second design (Fig. 2.16b, d) is based on our devised three identical parallel electrodes (width and spacing: 250 μm) positioned 250 μm away from a single orthogonally oriented electrode (width: 250 μm). It can be noted that in this configuration, the region with highest ∇T appears between the tips of the parallel electrodes and the single orthogonally oriented electrode. As a result, the induced flow in the middle region (between the orthogonal electrodes) dominates the surrounding region and creates a directional flow. The electrothermal simulation, shown in Fig. 2.16a-d, verifies that the devised asymmetric electrode configurations result in directional flow profiles (the simulation details are explained in the supplementary materials.). To validate and characterize the flow induced by these configurations, 6 µm-diameter beads were introduced into the ACET electrode-patterned channel, and by applying different voltage levels, a range of flow velocities were achieved and characterized. Here, the corresponding induced velocities were estimated by sequentially imaging the advective motion of the beads. Figure 2.16g,h illustrate that the measured velocity values for both configurations are proportional to the 4th power of the applied voltage, which is in agreement with the expected electrothermal flow velocity-voltage relationship (as described above). Fundamentally, the maximum voltage for ACET-based operations is limited by electrolysis and degassing/boiling, as previously thoroughly analyzed in the context of conventional microfluidic devices [15].

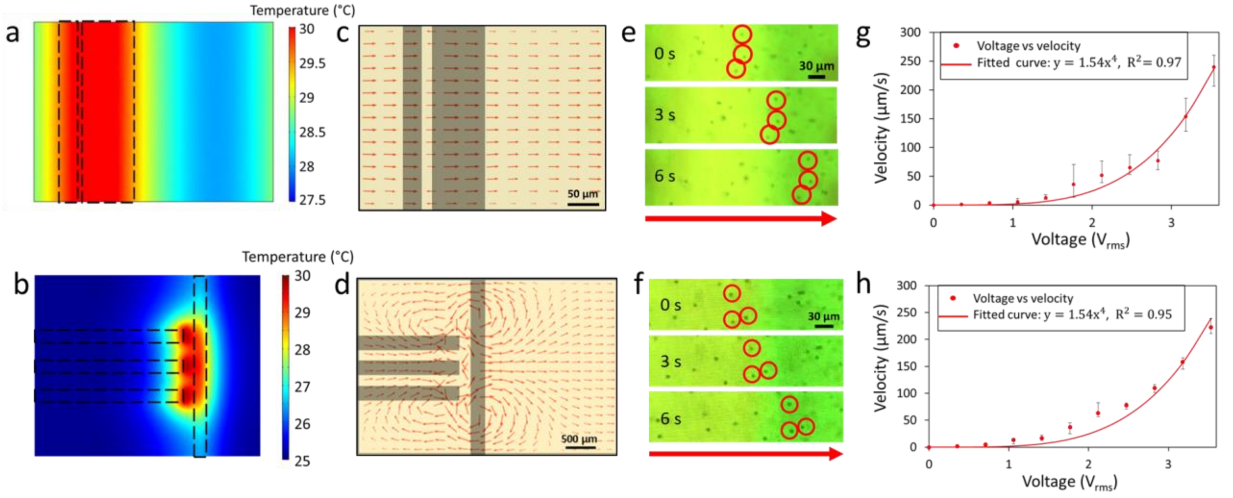

Figure 2. 16 *Directional ACET flow simulation and characterization: a, b) Simulated thermal profiles of parallel (a) and orthogonal (b) electrode configurations (top-view); c, d) The respective simulated ACET-induced velocity profiles illustrating net fluid direction (top-view); e, f) Sequential images of microbeads moving downstream of the channel due to the ACET directional flow (at t = 0 s, 3 s, 6 s); g, h) Characterization of the induced velocities for a range of applied voltages, indicating velocity is proportional to the 4th power of applied voltage.*

2.3.4 ACET mixing

Through the elaborate design of the ACET electrode configurations, the induced flow profile can be engineered to deliver the intended fluidic processing operations. For example, to achieve mixing of neighboring laminar flow streams, a rotationally symmetric electrode pair configuration can be used [10], which induces local in-plane micro-vortex flow profile. As shown in the context of conventional lab-on-a-chip devices, electrofluidic mixing can be used to overcome laminar flow limitations when introducing external reagents to implement complex bioassay, as well as to enhance analyte transport onto the sensing interface, both of which can be potentially adopted for on-body applications [9,10]. As shown in Fig. 2.17a, b, the electrothermal simulation validates the induction of stirring-like fluid flow profile. In order to evaluate the mixing performance of this configuration, the mixing electrode pair is used to induce mixing of two neighboring injected laminar fluid flows (one 1X phosphate buffered saline, PBS, another 0.2X PBS dyed with Rhodamine B for visualization, injected by two syringe pumps in parallel) downstream of a reverse-bifurcated channel (Fig. 2.17c). In this way, the effect of locally generated flow vortices (as induced by these electrodes) can be characterized against pressure-driven flow profiles. As observed experimentally (Fig. 2.18), the induced vortices are initially most significant at the end-junctions in-between the narrow and wide electrodes, where the flow field is strongest (as visualized by the simulation results in Fig. 2.17b). This phenomenon can also be observed for different scaled configurations, as illustrated in Fig. 2.18, where we simulated the effect of device/channel scaling on ACET actuation performance.

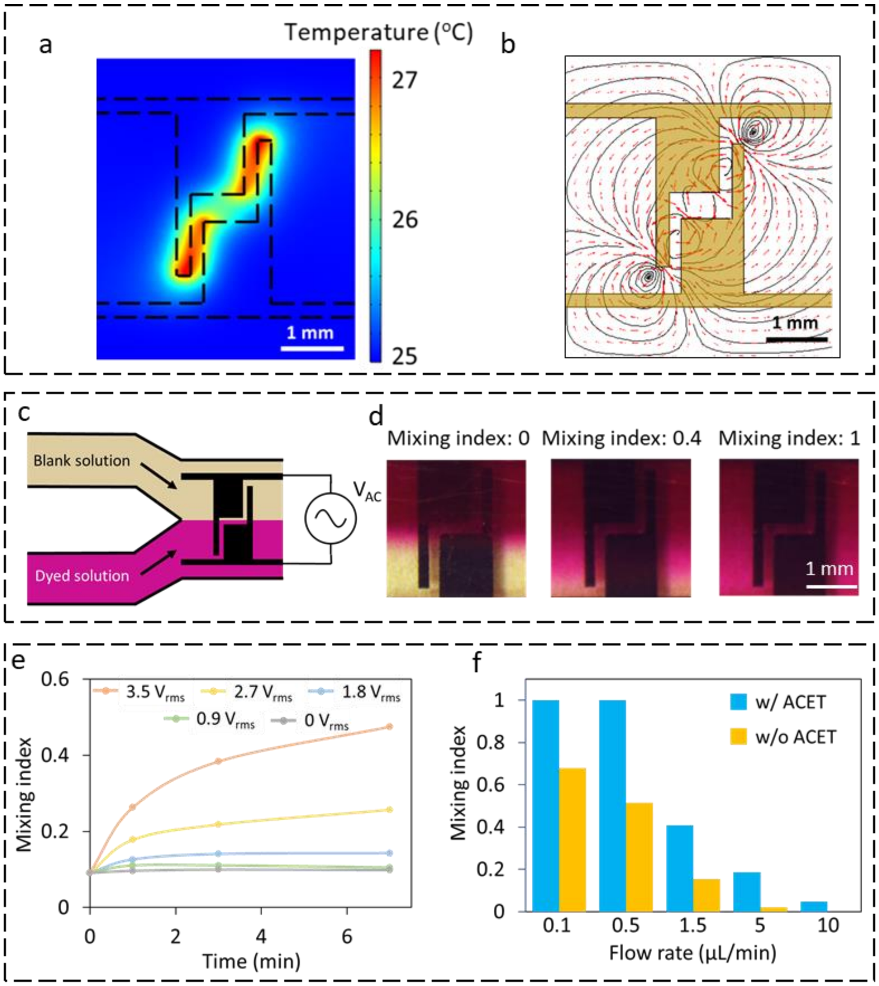

Figure 2. 17 *ACET mixing simulation and characterization. a) Simulated thermal profile of rotationally symmetric electrodes for ACET mixing (applied voltage: 3.5 V_{rms}); b) The respective simulated ACET-induced velocity profile, illustrating a vortex-like fluid motion (velocity field and vector are correspondingly shown with streamlines and arrows); c) Experimental setup for the ACET mixing of two fluids (blank and dyed solutions); d) Optical images corresponding to mixing indices of 0, 0.4 and 1; e) Mixing index vs. time for a range of applied voltages (externally driven flow rate: 1.5 µL/min); f) Comparison of mixing index vs. flow rate with and without ACET actuation (captured at t = 2 min, applied voltage: 3.5 V_{rms}).*

A mixing index is defined, which effectively captures the reciprocal of the standard deviation of the local dye density in the imaged region (the higher the index value, the lower the standard deviation, and the more uniform the local dye density in the imaged region). This index is linearly mapped over the range of 0 to 1, where 0 corresponds to the initial state with flow rate of 10 uL/min (negligible passive mixing), and 1 corresponds to the fully-mixed steady state where the whole image is homogeneous (*e.g.*, at minute 2 of mixing for flow rate of 0.5uL/min) (Fig. 2.17d). Due to its electro-fluidic nature, this mixing capability can be precisely tuned by programming the applied voltage at the electrodes.

The temporal mixing progression was characterized under different applied voltage levels (at constant flow rate of 1.5 μL/min, corresponding to the typical sweat rate induced when iontophoretically stimulating 1 cm^2 of skin area). As shown in Fig. 2.17e, an increasing mixing index with the applied voltage can be observed, where the steady state is reached within about three minutes upon activation of ACET. The ACET-induced stirring capability was further characterized under a range of flow rates (at constant applied voltage of 3.5 V_{rms}) and compared with passive mixing (without ACET actuation). As shown in Fig. 2.17f, the mixing index in both cases of passive and active mixing increases with decreasing flow rate (as expected, because of the smaller Péclet number), while in all scenarios, the induction of ACET flow results in the enhancement of the mixing efficiency.

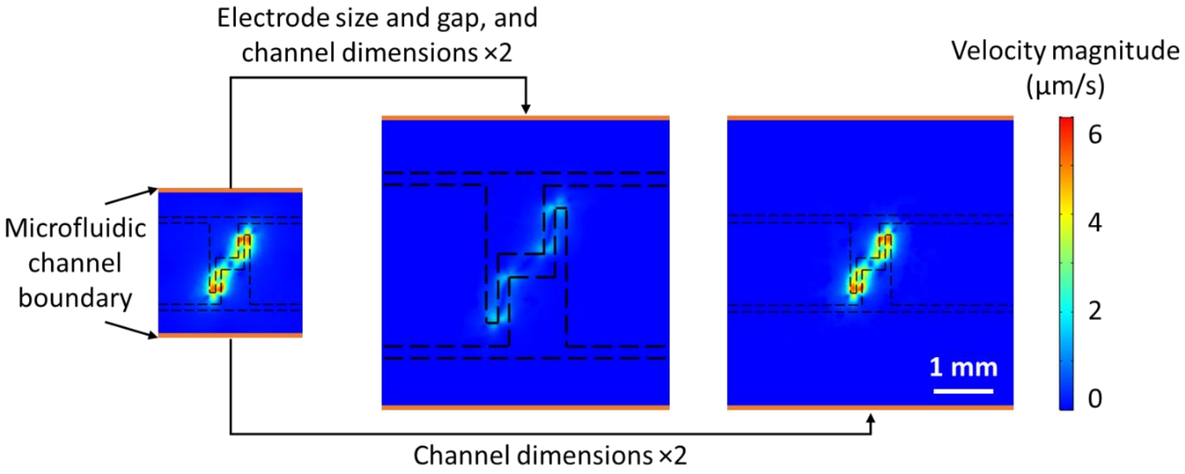

Figure 2. 18 *Effect of device size scaling on ACET actuation. Simulated fluid velocity magnitude profiles of ACET mixing for three configurations (top view, microfluidic channel boundary defined by the brown line, at the 100 μm above the rotationally symmetric electrodes, applied voltage: 3.5* V_{rms}*, fluid conductivity: 0.6 S/m): 1) original design (left, discussed in the main text, Fig. 3), 2)*

design with electrode size and gap, and channel dimensions ×2 (center), and 3) design with channel dimensions ×2 only (right). Comparison of the results of the configurations 1 and 2 yields that the increased scaling of the dimensions leads to a substantial decrease in the ACET-induced velocities (because of the reduction in electric field magnitude). Comparison of the results of the configurations 1 and 3 yields that the increased scaling of the channel (without scaling the electrode dimensions) leads to negligible decrease in the ACET-induced velocities (because the electric field concentrated region between the two electrodes is minimally affected).

The stability and robustness of the ACET actuation system for envisioned wearable applications is illustrated in Fig. 2.19a, where it can be observed that the intended mixing operation is achieved over an extended amount of time (> 8 hr) and at high ambient temperatures (*e.g.*, 40 °C). Additionally, the mixing performance is evaluated by placing the device at various angles (0-90^o, to simulate the device orientation conditions on body) and characterizing the mixing index for both cases of with and without ACET actuation. The results show that for all orientation angles, mixing takes place at significantly faster rate for the ACET-induced cases as compared to that of the passive mixing cases (Fig. 2.19b). For practical applications, the influence of variation in biofluid ionic strength on the intended ACET actuation performance must also be considered. Generally, higher biofluid ionic strength (*i.e.*, higher biofluid salt concentration) results in higher conductivity of the solution, and thus, higher temperature, which leads to establishing greater temperature gradient and stronger electrothermal body forces inside the channel. Therefore, in the context of ACET mixing, a higher mixing efficiency should be expected for higher solution conductivity. To demonstrate this point, we specifically repeated the ACET mixing efficiency characterization experiment for solutions with different salt concentration levels, and simulated the corresponding ACET-induced velocity. The results indicate that with higher fluid conductivity, both the mixing efficiency and induced velocity enhance (Fig. 2.20). While the results demonstrate that the intended mixing profile is achieved, if precise control on the biofluid actuation is desired, auxiliary conductivity sensing interface may be incorporated to adjust the excitation level accordingly.

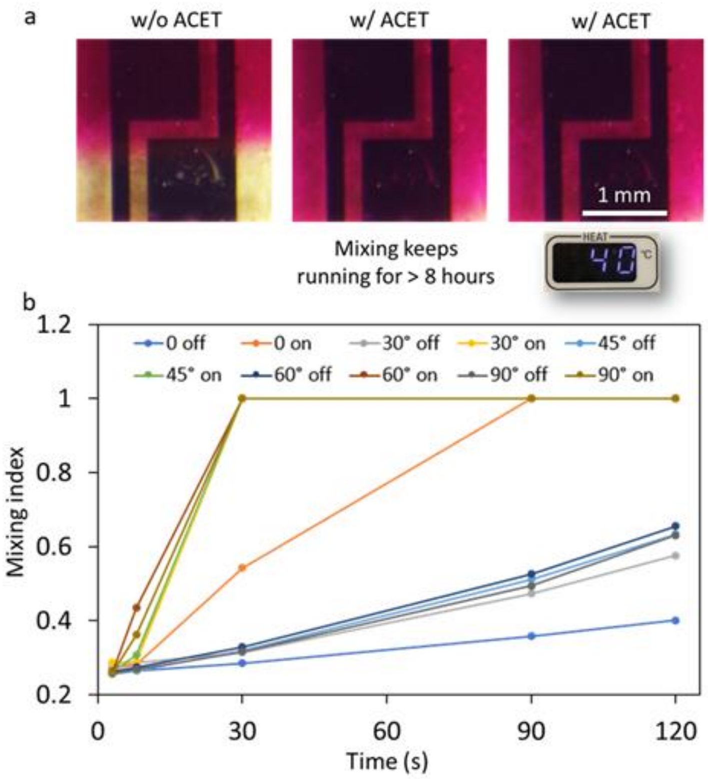

Figure 2. 19 *Stability of ACET actuation. a) Optical images of the ACET mixing process when ACET actuation was deactivated, activated for more than 8 hrs at room temperature, and activated with a surrounding temperature of 40 °C; b) Mixing index vs. time for various device orientations (externally driven flow rate: 0.5 µL/min, ACET Voltage: 3.5* V_{rms}*).*

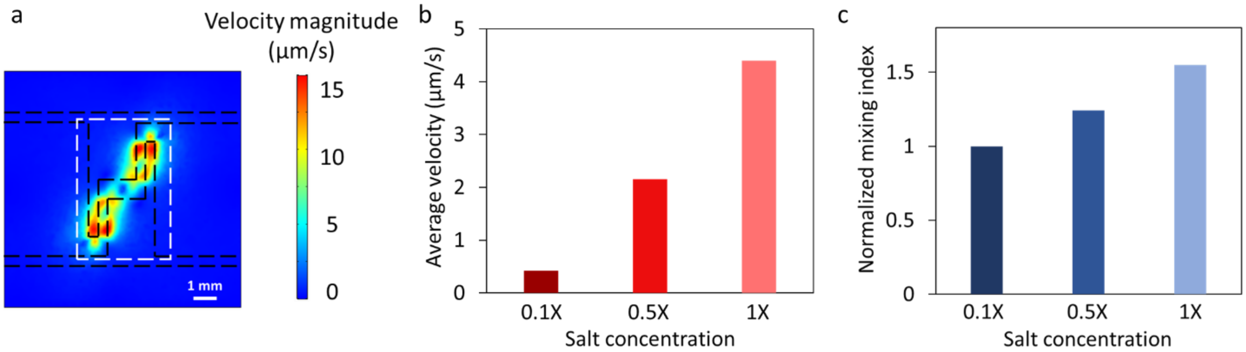

Figure 2. 20 *Influence of the solution salt concentration on ACET actuation. a) Simulated fluid velocity magnitude profile (top view, at the 100 µm above the rotationally symmetric electrodes, applied voltage: 3.5* V_{rms}*, fluid conductivity: 1.6 S/m). The white box outlines the area analyzed in Fig. 2.20; b) Simulated velocity magnitude with different salt concentration levels (averaged over the outlined area in Fig. 2.20, assumed fluid conductivity values of 0.16, 0.8, 1.6 S/m for 0.1X,*

0.5X and 1X PBS solutions, respectively); c) Experimentally characterized mixing index vs. solution salt concentration level (normalized with respect to the 0.1X PBS solution case).

To address the bottleneck of ACET actuation with a wearable high frequency excitation system, we leverage a push-pull transistor-based configuration, which generates a symmetric sinusoidal signal within the required voltage (0-3.5 V_{rms}) and frequency (~1-8 MHz) ranges (Fig. 2.21a-e). This transistor configuration is driven with the aid of a microcontroller unit (MCU, ATmega328 – TQFP, Atmel), which additionally facilitates system level functionalities, including user-initiated command processing and data communication.

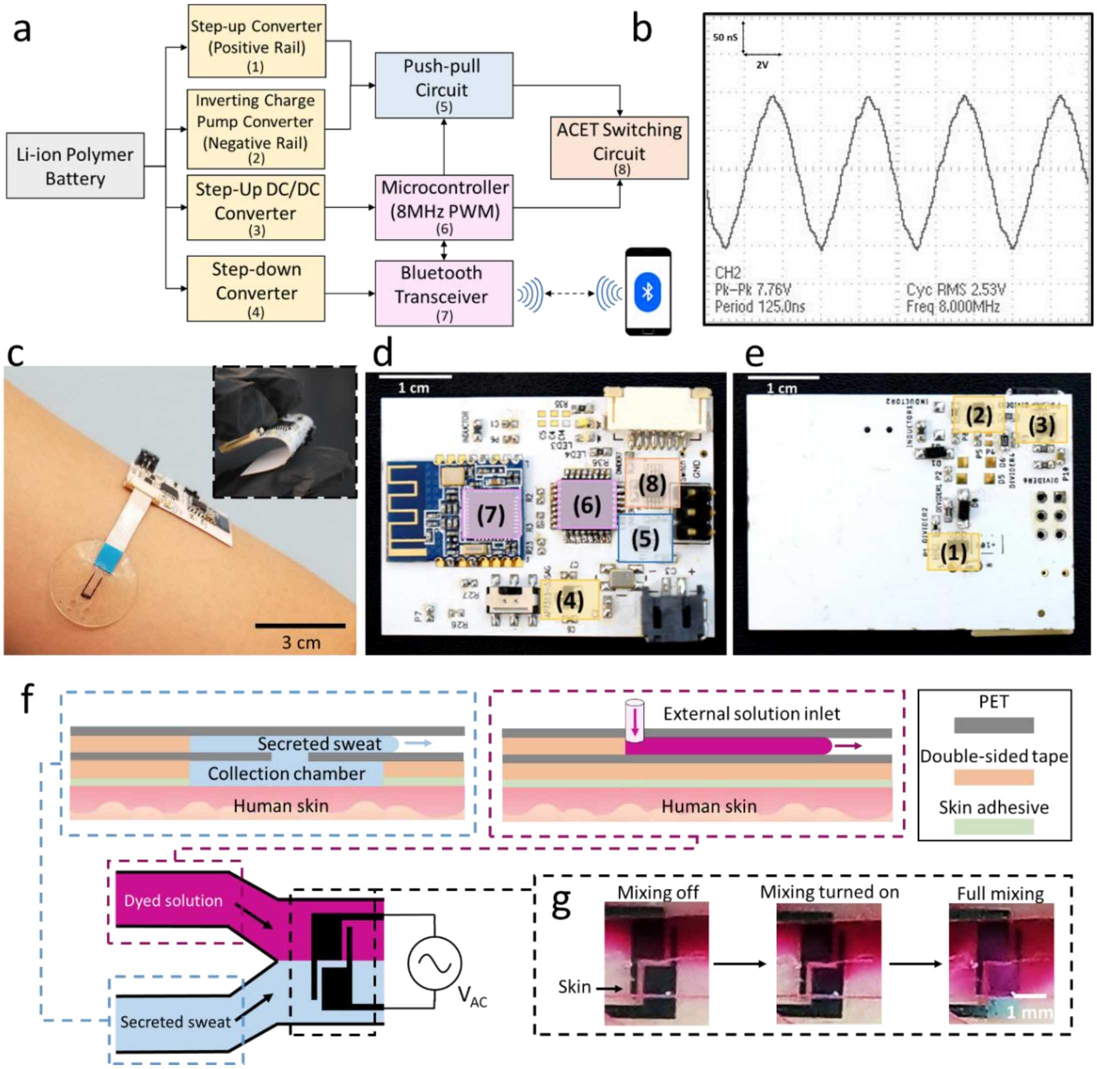
a
Li-ion Polymer Battery
Step-up Converter (Positive Rail) (1)
Inverting Charge Pump Converter (Negative Rail) (2)
Step-Up DC/DC Converter (3)
Step-down Converter (4)
Push-pull Circuit (5)
Microcontroller (8MHz PWM) (6)
Bluetooth Transceiver (7)
ACET Switching Circuit (8)
b
50 nS
2V
CH2
Pk–Pk 7.76V
Period 125.0ns
Cyc RMS 2.53V
Freq 8.000MHz
c
3 cm
d
1 cm
(7)
(6)
(8)
(5)
(4)
e
1 cm
(2)
(3)
(1)
f
Secreted sweat
Collection chamber
Human skin
External solution inlet
Human skin
PET
Double-sided tape
Skin adhesive
Dyed solution
Secreted sweat
V_AC
g
Mixing off
Mixing turned on
Full mixing
Skin
1 mm

Figure 2. 21 *Wearable ACET excitation and visualization on-body. a) System level diagram of the ACET excitation circuit (numbers 1 through 7 indicate corresponding circuitries on the ensuing FPCB images); b) A representative push-pull circuit voltage output for ACET actuation; c) A representative assembled FPCB, integrated with the microfluidic device, placed on a human subject's forearm; d) Front view of the assembled FPCB; e) Rear-view of the assembled FPCB; f) Top view schematic of the experimental setup for the ACET mixing of secreting sweat with an externally pumped red-dyed solution. Corresponding side-views of the two inlets of the device-epidermal interface are shown atop; g) Sequential optical images of the on-body mixing of iontophoretically induced sweat with a red-dyed solution.*

As shown in Fig. 2.21a and Fig. 2.22, the gate signals of the push-pull transistors are controlled by using the MCU's 8 MHz Pulse-Width-Modulation (PWM) output as an input control signal to output an amplified symmetric sinusoidal signal (Fig. 2.21b). The PWM temporal characteristics are defined by programming the MCU's timer prescalers to generate a 50% duty cycle. The step-up and negative charge pump converters provide the voltages needed for the positive and negative rails of the transistors. To achieve a symmetric excitation signal, an AC coupling capacitor is included at the output (Fig. 2.22). A digital switch is incorporated in the system design to facilitate the control of the excitation module (Fig. 2.22).

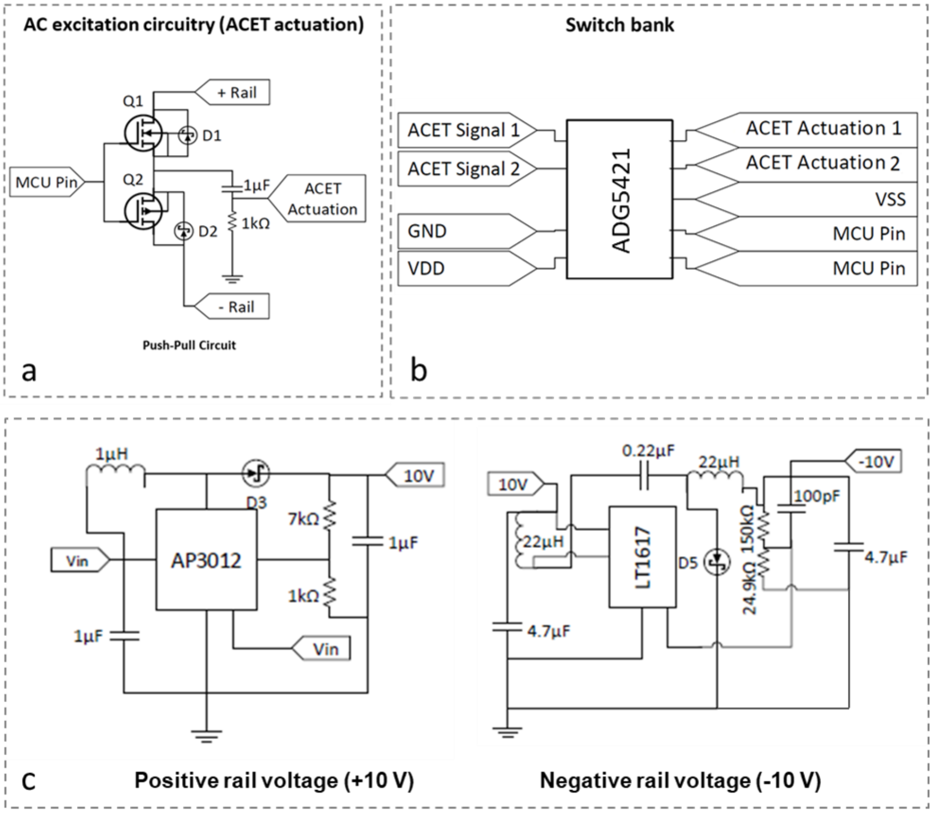
AC excitation circuitry (ACET actuation)
Q1
+ Rail
D1
MCU Pin
Q2
1μF
ACET Actuation
D2
1kΩ
- Rail
Push-Pull Circuit
a
Switch bank
ACET Signal 1
ACET Signal 2
GND
VDD
ADG5421
ACET Actuation 1
ACET Actuation 2
VSS
MCU Pin
MCU Pin
b
1μH
D3
10V
7kΩ
Vin
AP3012
1μF
1kΩ
1μF
Vin
0.22μF
22μH
-10V
10V
100pF
22μH
LT1617
D5
150kΩ
24.9kΩ
4.7μF
4.7μF
c
Positive rail voltage (+10 V)
Negative rail voltage (-10 V)

Figure 2. 22 *Overview of the wireless FPCB. Schematic diagram of the a) AC excitation circuit (including the peripheral components). b) ACET switching circuit (implementing a two-channel activation and actuation). c) Implementation of the positive and negative rails of the push-pull circuit using AP3012 (SOT-23-5 – Diodes Inc.) and LT 1617 (SOT-23 – Linear Technology) integrated circuit chips to generate +10 V and -10 V.*

The aforementioned circuit configurations are implemented onto a Bluetooth-enabled flexible printed circuit board (FPCB), which in turn facilitates wireless and bilateral communication of user commands with a custom-developed interactive smartphone application (Fig. 2.21a-e). To power the FPCB, a single miniaturized rechargeable lithium-ion polymer battery with a nominal voltage of 3.7 V is used. To achieve a power-efficient system, the intended circuit configurations are implemented using the integrated circuit chips that are specifically designed for low-power applications. Based on preliminary characterization results, without further power optimization, the envisioned simultaneous operations (*e.g.*, ACET actuation and bilateral wireless communication) demand supply current levels of approximately 50-100 mA. The battery's capacity should be selected in relation to the duration/frequency of intended operation as well as the desired ACET actuation performance. To illustrate the latter point, we characterized the delivered power for achieving different ACET mixing efficiencies (Fig. 2.23).

Voltage (V_{rms})	Power (mW)	Mixing index
0.9	0.03	0.11
1.8	0.275	0.14
2.7	0.99	0.26
3.5	2.35	0.48

Figure 2. 23 *Power consumption vs. Mixing index for different ACET excitation voltage levels (performed in 1X PBS solution, excited by a function generator Tektronix AFG3102C).*

To realize on-body implementation of the ACET excitation, the electrical connections between the microfluidic and the FPCB modules can be established with a flat flexible cable and a vertically conductive tape or stretchable wires (Fig. 2.21c). To visualize the achievement of the ACET actuation, the aforementioned mixing characterization setup was adopted, where the reverse-bifurcated microfluidic configuration was placed on body (using two externally pumped model solutions: 1X transparent and 0.2X red-dyed PBS, Fig. 2.24a). As shown in Fig. 2.24b, activation of the ACET excitation circuit leads to the mixing of the two neighboring laminar flow streams and rendering a homogenized fluid stream. Furthermore, the utility of the devised wearable ACET actuation interface for epidermally-retrieved biofluid actuation is shown by demonstrating *in-situ* mixing of the secreting sweat with an externally pumped model solution (0.2X red-dyed PBS). For localized sweat induction, the standard iontophoresis protocol was followed [16]. As illustrated in Fig. 2.21f, a sweat collection chamber is incorporated to harvest and route the secreting sweat through one inlet, while the model solution was pumped into the other inlet (where its flow rate was adjusted to match the sweat secretion rate, here, 1.5 µL/min). As shown in Fig.

2.21g, the results indicate that upon activation of the ACET actuation (3.5 V_{rms}), homogeneous mixing of the secreting sweat and the model solution streams was achieved, demonstrating the suitability of ACET actuation for biofluid manipulation.

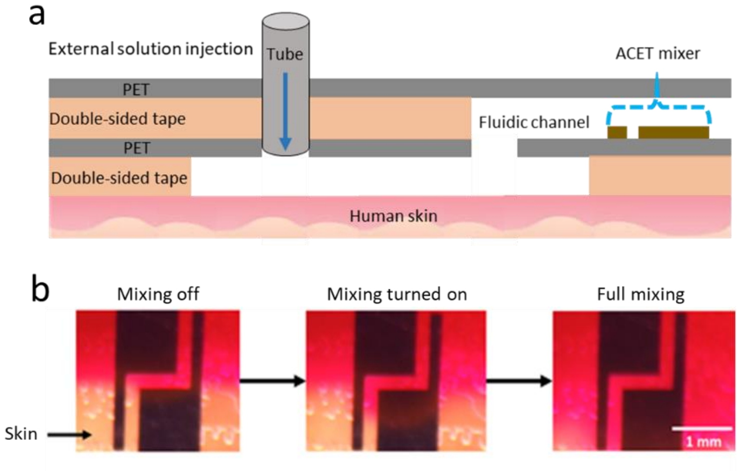
a
External solution injection
Tube
ACET mixer
PET
Double-sided tape
Fluidic channel
PET
Double-sided tape
Human skin
b
Mixing off
Mixing turned on
Full mixing
Skin
1 mm

Figure 2. 24 *Visualization of the ACET actuation with the wireless electrofluidic actuation system, performed on body with externally-pumped model solutions (1X transparent and 0.2X red-dyed PBS solutions); a) Cross-view schematic of the device-epidermal interface (for the channel containing the transparent solution); b) Sequential optical images of the on-body mixing process. For the channel containing the red-dyed solution, a PET layer is used, to physically isolate the solution from the skin.*

2.3.5 References

1. Ajdari, A., Stroock, A. D., Dertinger, S. K. & Whitesides, G. M. Patterning Flows Using Grooved Surfaces: Application to Microfluidics. Micro Total Analysis Systems 2002 620–622 (2002) doi:10.1007/978-94-010-0504-3_6.
2. Lu, L.-H., Ryu, K. S. & Liu, C. A magnetic microstirrer and array for microfluidic mixing. Journal of Microelectromechanical Systems vol. 11 462–469 (2002).
3. Jeong, G. S., Chung, S., Kim, C.-B. & Lee, S.-H. Applications of micromixing technology. The Analyst vol. 135 460 (2010).
4. Frommelt, T. et al. Microfluidic Mixing via Acoustically Driven Chaotic Advection. Physical Review Letters vol. 100 (2008).

5. Wong, P. K., Wang, T.-H., Deval, J. H. & Ho, C.-M. Electrokinetics in Micro Devices for Biotechnology Applications. IEEE/ASME Transactions on Mechatronics vol. 9 366–376 (2004).
6. Wu, J., Lian, M. & Yang, K. Micropumping of biofluids by alternating current electrothermal effects. Appl. Phys. Lett. 90, 234103 (2007).
7. Du, E. & Manoochehri, S. Enhanced ac electrothermal fluidic pumping in microgrooved channels. Journal of Applied Physics vol. 104 064902 (2008).
8. Loire, S., Kauffmann, P., Mezić, I. & Meinhart, C. D. A theoretical and experimental study of ac electrothermal flows. Journal of Physics D: Applied Physics vol. 45 185301 (2012).
9. Chang, C.-C. & Yang, R.-J. Electrokinetic mixing in microfluidic systems. Microfluidics and Nanofluidics vol. 3 501–525 (2007).
10. Huang, S.-H., Wang, S.-K., Khoo, H. S. & Tseng, F.-G. AC Electroosmotic Generated In-Plane Microvortices for Stationary or Continuous Fluid Mixing. TRANSDUCERS 2007 - 2007 International Solid-State Sensors, Actuators and Microsystems Conference (2007) doi:10.1109/sensor.2007.4300392.
11. Lu, Y. et al. AC Electrokinetics of Physiological Fluids for Biomedical Applications. J. Lab. Autom. 20, 611–620 (2015).
12. Dekker, S., Isgor, P. K., Feijten, T., Segerink, L. I. & Odijk, M. From chip-in-a-lab to lab-on-a-chip: a portable Coulter counter using a modular platform. Microsystems & Nanoengineering vol. 4 (2018).
13. Peng, C., Zhang, Z., Kim, C.-J. 'cj' & Sungtaek Ju, Y. EWOD (electrowetting on dielectric) digital microfluidics powered by finger actuation. Lab on a Chip vol. 14 1117 (2014).

14. Cho, S. K., Moon, H. & Kim, C.-J. Creating, transporting, cutting, and merging liquid droplets by electrowetting-based actuation for digital microfluidic circuits. Journal of Microelectromechanical Systems vol. 12 70–80 (2003).
15. Castellanos, A., Ramos, A., González, A., Green, N. G. & Morgan, H. Electrohydrodynamics and dielectrophoresis in microsystems: scaling laws. Journal of Physics D: Applied Physics vol. 36 2584–2597 (2003).
16. [anonymus Ac06619969], Sweat Testing: Sample Collection and Quantitative Analysis, Approved Guideline. (2000).

2.4 Active biofluid sensing and on-body validation

2.4.1 Flow rate-undistorted biomarker analysis based on valve-gated sensing interface

To demonstrate the utility of the devised active biofluid management system in section 2.2, biochemical sensing interfaces are developed and incorporated in the sensing chamber of the valve-gated compartments (upstream of each compartment channel as shown in Fig. 2.25a), following the previously reported mediator-free enzymatic sensor development methodology [1]. We specifically adapted the sensing interfaces to target glucose and lactate as examples of informative metabolites. As illustrated in Fig. 2.25a, the corresponding sensing interfaces comprised of: 1) an enzymatic layer (glucose oxidase or lactate oxidase) to catalyze the oxidation of target molecules and generate hydrogen peroxide (H_2O_2) as a detectable byproduct; 2) a permselective membrane (poly-m-phenylenediamine) to reject interfering electroactive species; and 3) an electroanalysis layer (platinum) to detect the generated H_2O_2. The response of the glucose and lactate sensors were validated within the respective analytes' physiologically relevant concentration range in sweat [2,3]. As shown in Fig. 2.25b and c, for both sensors, linear relationships were observed between the measured current responses and target analytes' concentration levels ($R^2 = 0.99$, for both sensors)

The active biofluid flow control achieved by the valving system can be leveraged to address sensor-level challenges relevant to wearable biomarker sensing. In particular, here, the valving capability was utilized to decouple the confounding influence of flow rate variability on sensor response, an issue which is well-reported in the context of conventional lab-on-a-chip platforms [4-7], but overlooked by previously reported wearable sensors.

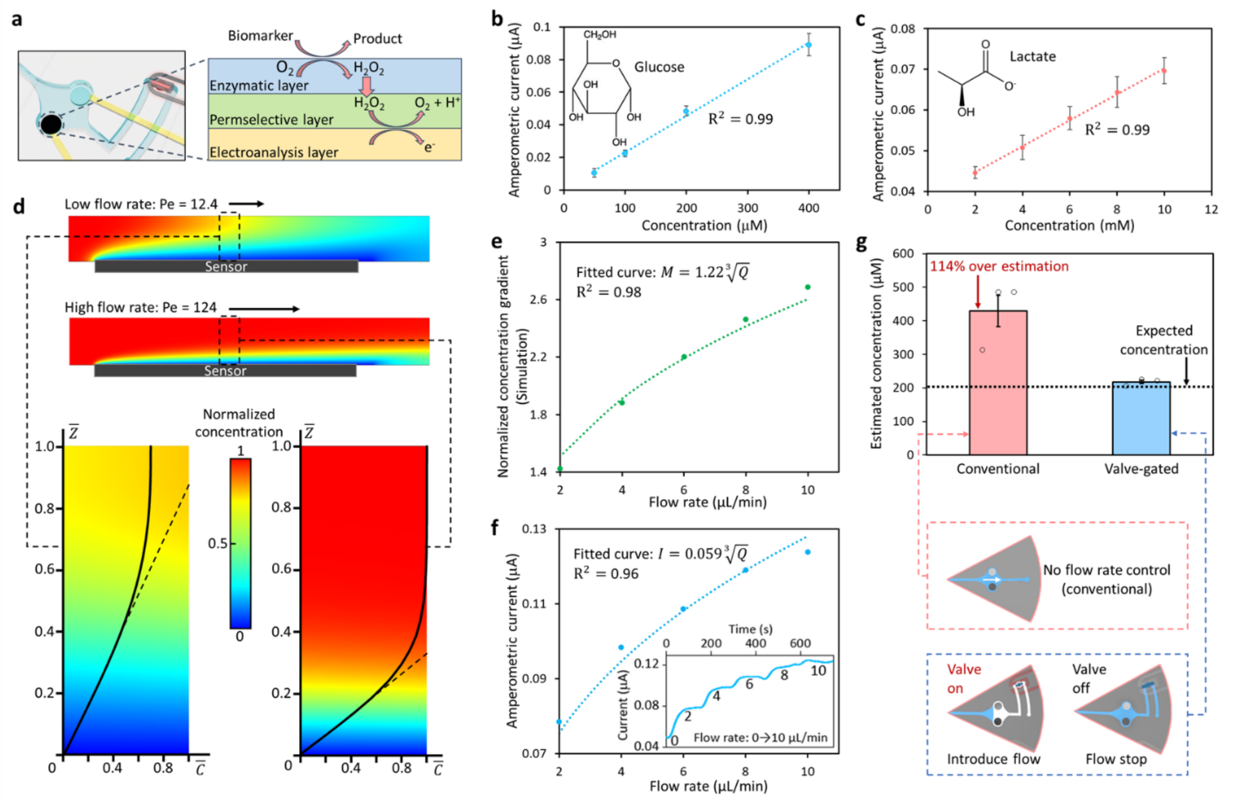

***Figure 2. 25** Demonstration of flow rate-undistorted biomarker analysis. a) Reaction schematic of the developed sensor (embedded within a valve-gated compartment); b, c) Current response to target analytes for (b) a glucose sensor and (c) a lactate sensor. Error bars, mean ± s.e (n = 3 measurements from different sensors); d) Simulated analyte concentration (gradient) profiles for relatively low and high flow rate conditions (low flow rate: $Q = 1\ \mu L\ min^{-1}$, resulting in $P_e = 12.4$, high flow rate: $Q = 10\ \mu L\ min^{-1}$, resulting in $P_e = 124$, assuming a channel transverse width of 2 mm and analyte diffusivity constant of $6.7 \times 10^{-6}\ cm^2\ s^{-1}$). The annotated dashed lines tangent to the normalized concentration curves indicate the local analyte concentration gradient for the respective case; e) Simulated local analyte concentration gradient at various flow rates (the values*

are normalized to that obtained for the case of 1 µL min^{-1}*). The curve fitted line indicates that simulated data points present a* $\sqrt[3]{Q}$ *relationship; f) Measured amperometric current response of a glucose sensor to 200 µM glucose solution introduced at various flow rates. The inset figure shows the corresponding measured real-time amperometric current response in the presence of progressively increasing flow rate (from 0 to 10 µL min*$^{-1}$*). The curve fitted line indicates that simulated data points present a* $\sqrt[3]{Q}$ *relationship; g) Comparison of the estimated glucose concentration of a 200 µM glucose solution introduced at 5 µL min*$^{-1}$ *(no valve) and 0 µL min*$^{-1}$ *(corresponding to valve-gated condition). Error bars, mean ± s.e (n = 3 measurements from different sensors).*

In a generalizable continuous microfluidic electrochemical sensing setting, the response of the sensor is flow rate-dependent, because of the central role of advective flow in transporting analytes to the sensor [8]. In the case of electrochemical sensing, the sensor current response (I) is proportional to the flux of analyte molecules onto the sensor surface, which in turn is directly proportional to the local concentration gradient ($M = \frac{\partial c}{\partial z}$). In that regard, determining the local concentration gradient requires the consideration of various coupled phenomena, including advective and diffusive analyte transport to the sensor surface, and the reaction rate at the sensor surface. As described in the Appendix D, the coupled problem at hand can be simplified by assuming the sensor has a high surface reaction rate, and that advection is the dominant form of analyte transport (manifested as Peclet number >> 1, due to the relatively high sweat rate Q ~ 1-10 µL min^{-1} during active secretion). The theoretical analysis based on these assumptions leads to the $I \propto M \propto \sqrt[3]{Q}$ relationship.

This relationship was validated through finite element analysis (COMSOL), where we simulated the analyte concentration profile at the sensor surface in response to various continuous flow rates (within the physiologically relevant range of sweat secretion rate). As shown in Fig. 2.25d, e, the concentration gradient on the sensor surface increased along with the flow rate in the microfluidic chamber, in which M was proportional to $\sqrt[3]{Q}$ ($R^2 = 0.98$). Similarly, the measured amperometric current of a representative glucose sensor presented a cube-root relationship with Q (Fig. 2.25f, $R^2 = 0.96$), which is in agreement with our theoretical analysis.

Practically, without accommodating for the influence of dynamically varying flow rate (during on-body measurements), if conventional calibration methods are followed (which are performed at zero flow rate, *ex-situ*), inaccurate biomarker measurements will inevitably be obtained. This problem can be resolved by leveraging the devised valving mechanism, as it allows for performing analysis in a sample-and-hold manner. To elaborate, in a valve-gated sensing chamber, the valve can be opened, to allow for the introduction of the sample into the sensing chamber, and closed, to allow for sample compartmentalization and sensing at zero flow rate, thus effectively decoupling the confounding influence of flow rate variability. To demonstrate the influence of flow rate variability, the response of a representative glucose sensor to an introduced sample (containing 200 µM glucose) was monitored at 5 µL min^{-1} (no valve) and 0 µL min^{-1} (corresponding to valve-gated condition), and the corresponding estimated concentrations were derived by referring to the calibration curve (obtained at 0 µL min^{-1}). As shown in Fig. 2.25g, the conventional setup overestimated the glucose concentration by 114%, whereas the valve-gated condition accurately estimated the glucose concentration.

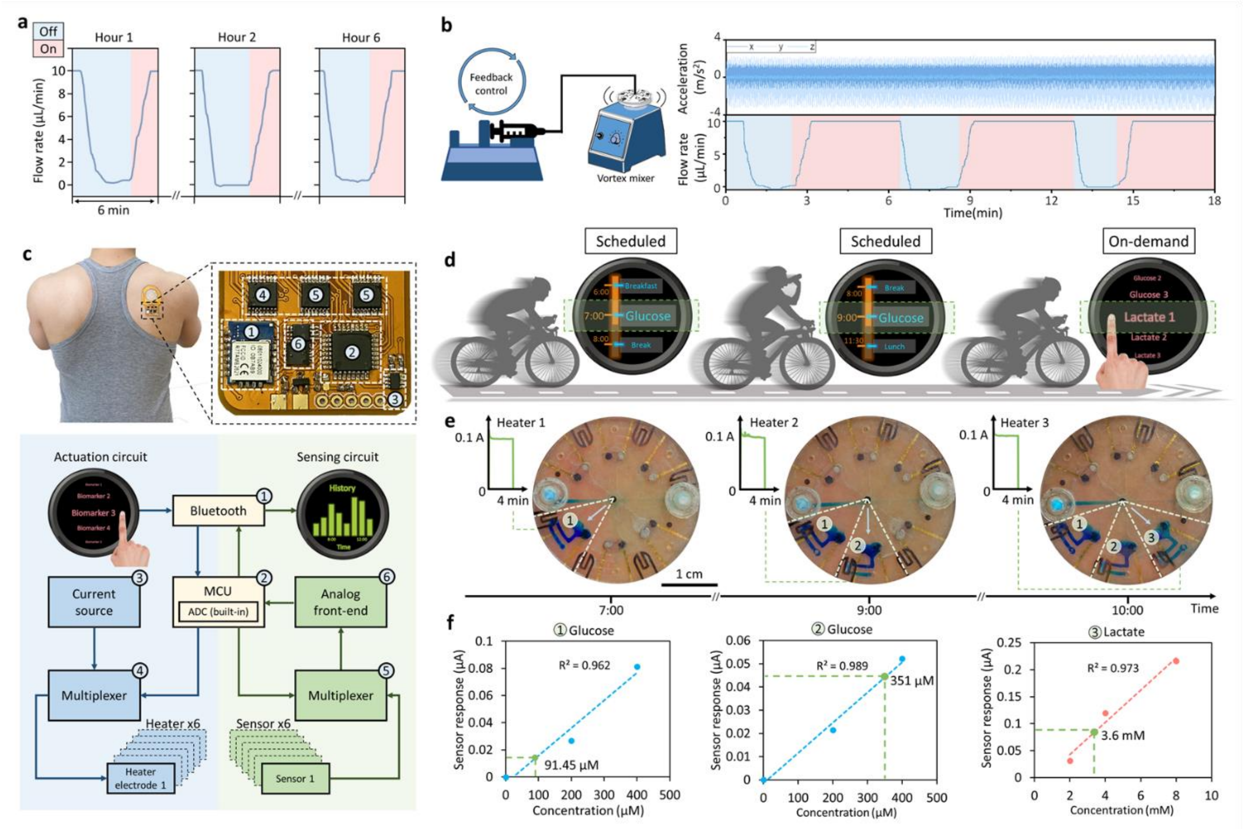

Figure 2. 26 *Integration and characterization for contextually-relevant on-body biomarker analysis. a) Ex situ characterization of the prolonged operation of the pressure-regulated valve (performed over six hours); b) Ex situ characterization of the high-fidelity operation of the pressure-regulated valve in the presence of vortical vibration. The vibrational acceleration profiles are presented in the top half, and the characterized flow rate profile is captured in the bottom half; c) Optical image of a representative fully integrated programmable epidermal microfluidic valving system applied on the back of a subject with a zoomed-in view of the FPCB electronic components. The block diagram details the circuit-level valve actuation and signal processing operations; d) Illustration of the planned study for scheduled/on-demand sweat sampling during physical activity (cycling); e) Optical images of intermittently sampled, routed, and compartmentalized sweat on-body (visualized with the aid of blue dyes, embedded within the compartments). Three valves were sequentially activated/deactivated at programmed timepoints during a physical exercise. The inset figures show the characterized electrical current through the respective valves' microheaters (activated for four minutes); f) Measured sweat glucose and lactate concentrations based on-body sensor readouts (green data points). The corresponding calibration curves (dashed lines) were constructed by linear fitting the measured sensor responses to three reference samples with known analyte concentrations (blue/red data points in the case of glucose/lactate sensors). Sweat glucose readouts were obtained by the valve-gated sensing compartments 1 and 2, before and after a scheduled beverage intake event, respectively. The sweat lactate readout was obtained by the valve-gated sensing compartment 3 upon on-demand user activation.*

2.4.2 Contextually relevant on-body biomarker analysis

In order to apply the devised pressure-regulated valving system for on-body biofluid management and biomarker analysis, we first evaluated the system's operational stability during prolonged use and in the presence of motion artifacts. In that regard, we applied the flow rate characterization setup to quantitatively monitor the performance of a pressure-regulated valve in an *ex-situ* setting. First, to assess its stability during a prolonged testing period, we sequentially activated and deactivated the valve at set timepoints over a period of 6 hours. Fig. 2.26a shows the flow rate, injected by the pressure-driven syringe pump, was successfully reduced to zero and back to its default value upon deactivation and activation of the valve, respectively. Additionally, figure 2.27 illustrates that for our context, hydrogel dehydration does not affect the intended valving functionality, as evident from the maintenance of a relatively constant pressure—across a valve-gated channel—over an extended amount of time (8 h). The minimal impact of hydrogel dehydration can be attributed to the small size of the outlets, minimizing the evaporation rate. Furthermore, to evaluate the stability of the valving system against motion artifacts, its performance was characterized under oscillatory motion (amplitude: ~3 m s^{-2} at 5 Hz [9], generated by a vortex mixer). The measured flow rate profile, shown in Fig. 2.26b, indicates the successful opening and closing of the valve.

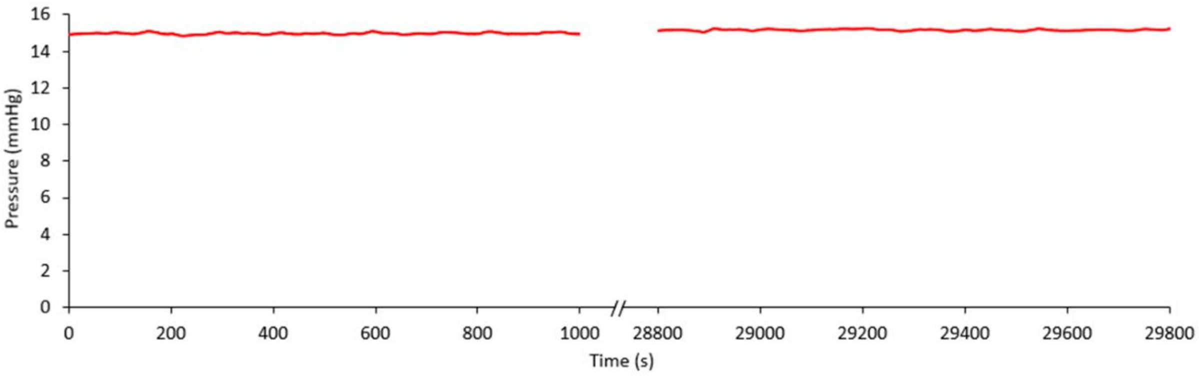

Figure 2. 27 *Validation of prolonged valve sealing. The maintenance of constant pressure across the valve-gated channel indicates that the channel remained fully sealed by the embedded hydrogel (without suffering from possible dehydration-induced shrinkage effects). Pressure characterization experiment was performed over 8 h, and pressure data was recorded in the first and last 1000 s-period of the experiment to illustrate the unchanged sealing status.*

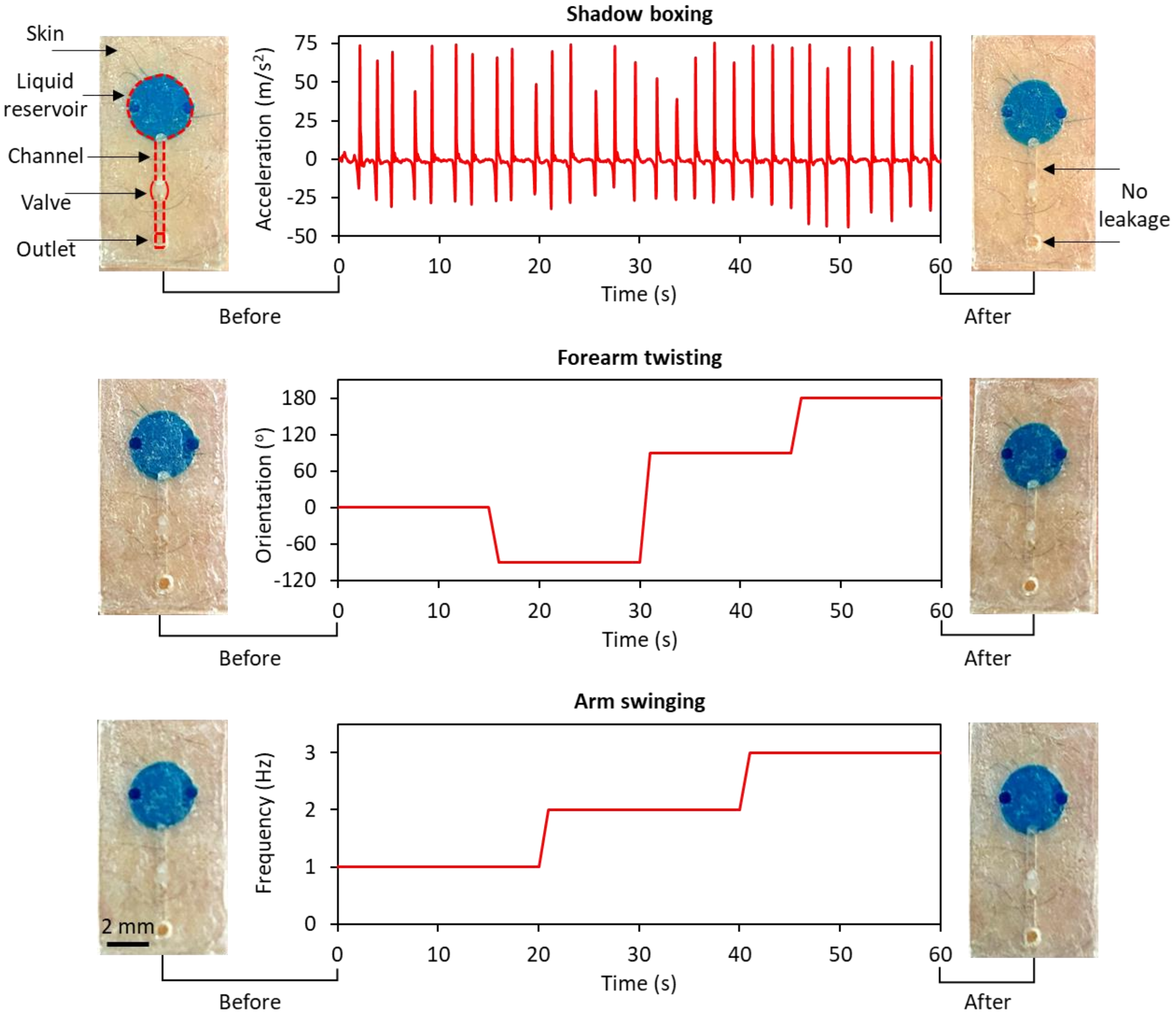

Figure 2. 28 *On-body validation of valve sealing with a subject—wearing the microfluidic module on the forearm—performing shadow boxing, forearm twisting, and arm swinging at different acceleration levels, orientations, and frequencies, respectively. Optical images of the microfluidic module before/after the activities demonstrate the leakage-free preservation of the compartmentalized blue-dyed sample, illustrating the device robustness under routine user motion.*

Further *ex-situ* and *in-situ* characterization results, shown in Fig. 2.28 and Fig. 2.29, provide insight into the robustness of the valving interface in the presence of mechanical deformation and unconstrained body motion. Altogether, these characterization results illustrate the preserved functionality of the valve over the test periods/conditions, informing the robustness of the valving operation for on-body application.

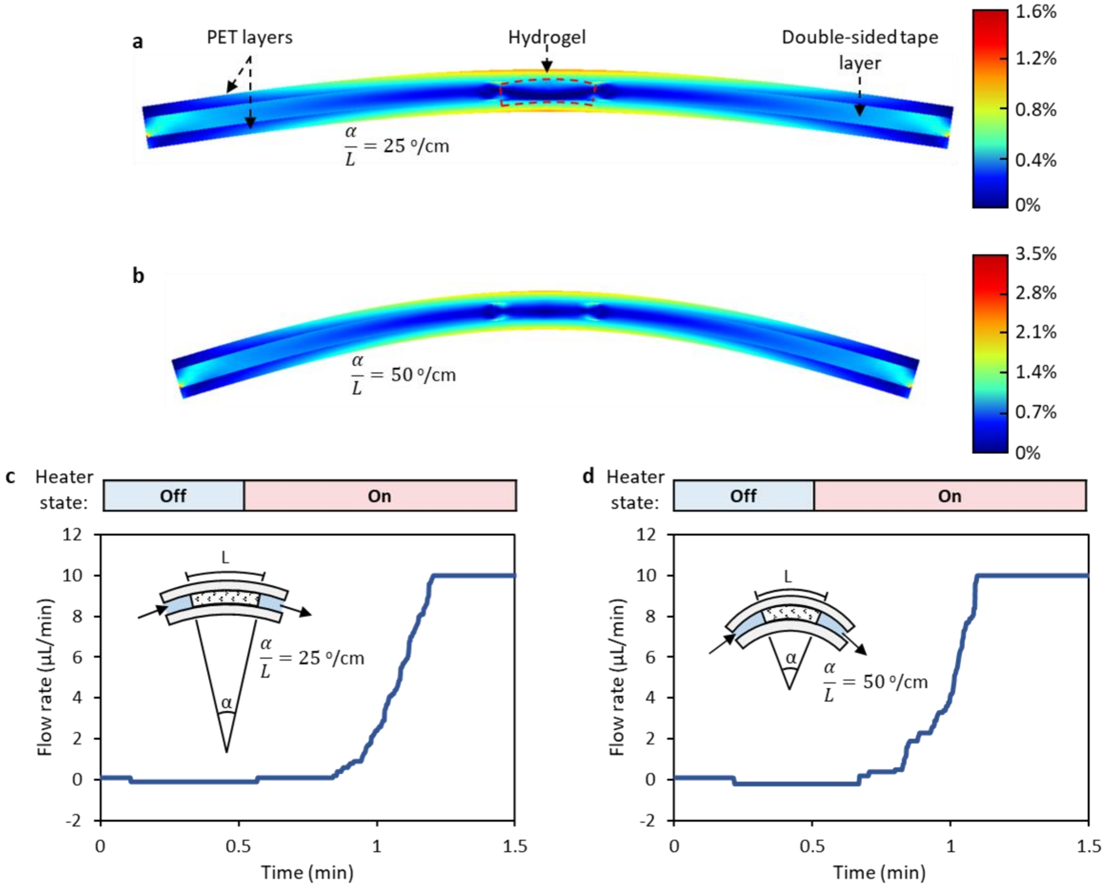

Figure 2. 29 *a-b) COMSOL-simulated strain profile (cross-view) of a flexible microfluidic valve, under two different device bending curvatures: a) α/L = 25 °/cm and b) α/L = 50 °/cm. The hydrogel embodiment sustains minimal strain, as it is located at the neutral plane. Hydrogel valve: 1 mm in length, 170 µm in height; c-d) Experimental validation of fluid valving under two device bending curvatures: c) α/L = 25 °/cm and d) α/L = 50 °/cm. The valve is activated after 0.5 min.*

To realize a wearable valve-enabled bioanalytical platform with seamless control command and biomarker data communication capabilities, the sensor array-coupled valving system is interfaced with a custom-developed wireless FPCB (Fig. 2.30 and Fig. 2.31). Structurally, the FPCB module is 100 µm-thick, and its base material is polyimide, the Young's modulus of which is on the same order as those of the materials used in the microfluidic module's structure.

In case a higher degree of mechanical flexibility is needed (*e.g.*, when interfacing high curvature areas), other base materials with lower Young's modulus can be used to construct the circuit board [10]. Figure 2.26c illustrates the operational block diagram of the FPCB, which is capable of rendering multi-channel valve-actuation and signal processing. Depending on the context at hand and the desired mode of analysis, an activation signal for the designated valve-gated sensing compartment is transmitted to the FPCB's microcontroller unit (MCU). This activation signal can be generated through a scheduled timetable or on-demand (initiated by the user). Upon processing the received command, and with the aid of a multiplexer unit, the MCU selects the appropriate actuation channel to power the corresponding microheater by a current source, subsequently opening the desired valve. Subsequently, the harvested biofluid is routed to the selected compartment. Then, following MCU-generated instructions, the valve closes, and the sensor response is recorded and processed by an analog front-end (consisting of potentiostat and low-pass filter units) *via* the multiplexer-selected sensing channel. The signal processed by the analog front-end is then translated to digital at the MCU level, and wirelessly communicated to a user interface. The user interface can be used to display the acquired biomarker information in real-time and to store it in the user's database.

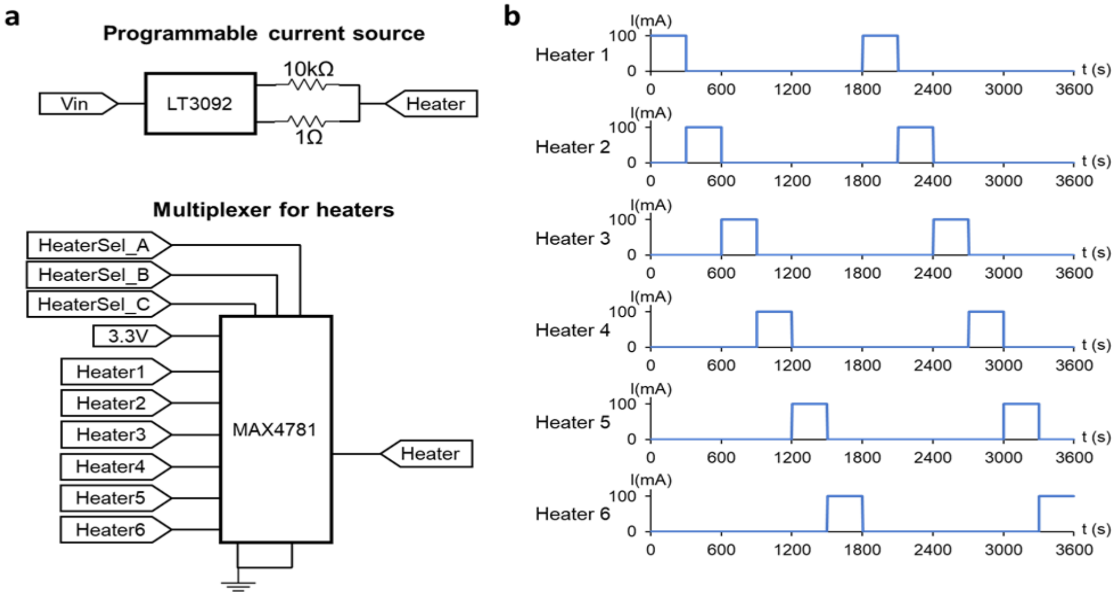
a
Programmable current source
Vin
LT3092
10kΩ
1Ω
Heater
Multiplexer for heaters
HeaterSel_A
HeaterSel_B
HeaterSel_C
3.3V
Heater1
Heater2
Heater3
Heater4
Heater5
Heater6
MAX4781
Heater
b
I(mA)
100
0
Heater 1
Heater 2
Heater 3
Heater 4
Heater 5
Heater 6
t (s)
0
600
1200
1800
2400
3000
3600

Figure 2. 30 *a) Schematic diagram of the actuation circuit, including the programmable current source and multiplexer (for microheaters) circuitries; b) The measured current through six electrical resistive microheaters upon the periodic and sequential activation/deactivation of the microheater array (resistive load: 25 Ω, connected at the output of each of the actuation channels).*

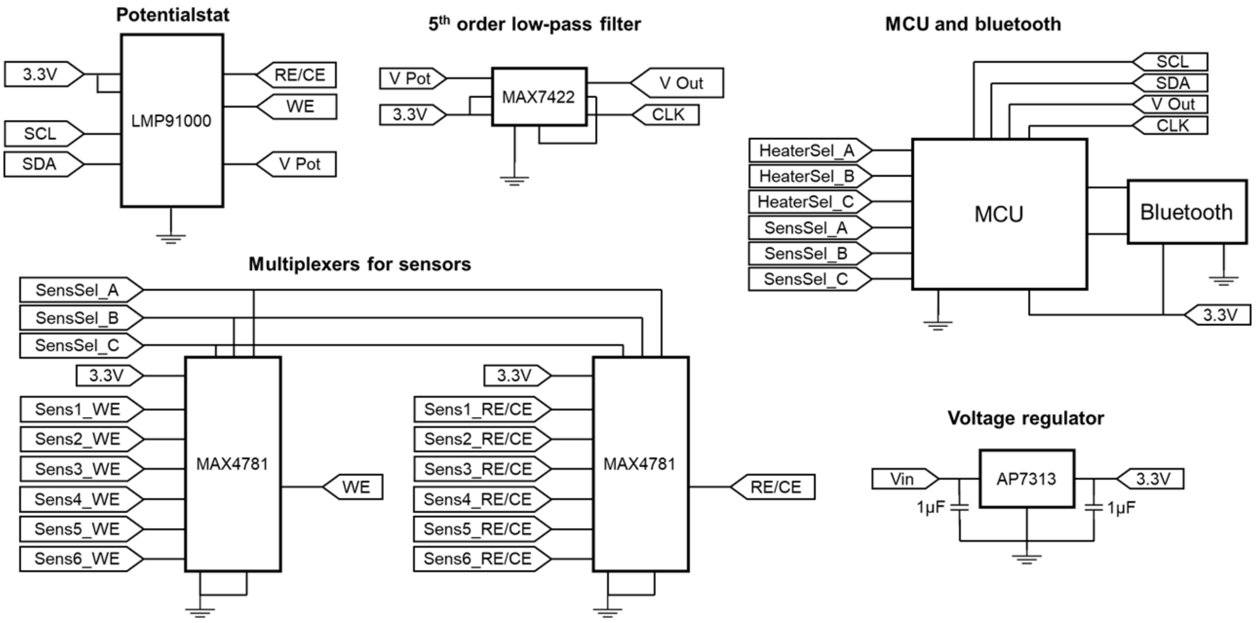
Potentialstat
3.3V
SCL
SDA
LMP91000
RE/CE
WE
V Pot
5th order low-pass filter
V Pot
3.3V
MAX7422
V Out
CLK
MCU and bluetooth
SCL
SDA
V Out
CLK
HeaterSel_A
HeaterSel_B
HeaterSel_C
SensSel_A
SensSel_B
SensSel_C
MCU
Bluetooth
3.3V
Multiplexers for sensors
SensSel_A
SensSel_B
SensSel_C
3.3V
Sens1_WE
Sens2_WE
Sens3_WE
Sens4_WE
Sens5_WE
Sens6_WE
MAX4781
WE
3.3V
Sens1_RE/CE
Sens2_RE/CE
Sens3_RE/CE
Sens4_RE/CE
Sens5_RE/CE
Sens6_RE/CE
MAX4781
RE/CE
Voltage regulator
Vin
AP7313
3.3V
1μF
1μF

Figure 2. 31 *Schematic diagrams of the sensing (consisting of potentiostat and LPF), MCU, wireless transmission (Bluetooth), and power regulating circuits.*

The devised wearable valve-enabled bioanalytical platform was deployed for sweat sampling at scheduled and on-demand timepoints, to illustrate the platform’s capability for contextually-relevant biomarker analysis applications (Fig. 2.26d). Accordingly, the platform was mounted on the back of a subject engaged in cycling (with the aid of a skin-adhesive layer, which provides adequate adhesion force to maintain the platform on the skin). Prior to on-body deployment, we activated the microheaters and monitored the electrical current passing through them to verify their operation. As can be seen from the on-body experiment, shown in Fig. 2.26e, the secreted sweat, at set scheduled/on-demand timepoints, was routed to and compartmentalized within the desired compartments (following a 4-min microheater activation time-window), while other compartments were protected. This time-stamped biofluid acquisition capability can be exploited to take contextual biomarker readings. As shown in Fig. 2.26f, the platform was programmed to take glucose readings before and after a scheduled beverage intake (Trutol, containing 50 g per 296 mL of dextrose) event, and sweat lactate level was measured on-demand as per the user’s command. Specifically, the biomarker readouts indicated the subject’s sweat glucose level was elevated after glucose intake, and the measured sweat lactate level was within an expected range (in agreement with previously reported studies) [11,12]. Figure 2.32 further validates our solution’s suitability for compartmentalization and sensor operations on-body. To provide physiologically meaningful interpretations of such sensor readouts, future large-scale studies should be conducted, aiming to contextualize the measured sweat biomarker concentrations in relation to relevant inter/intra-individual physiological variabilities (*e.g.*, gender, muscle density, and body hydration).

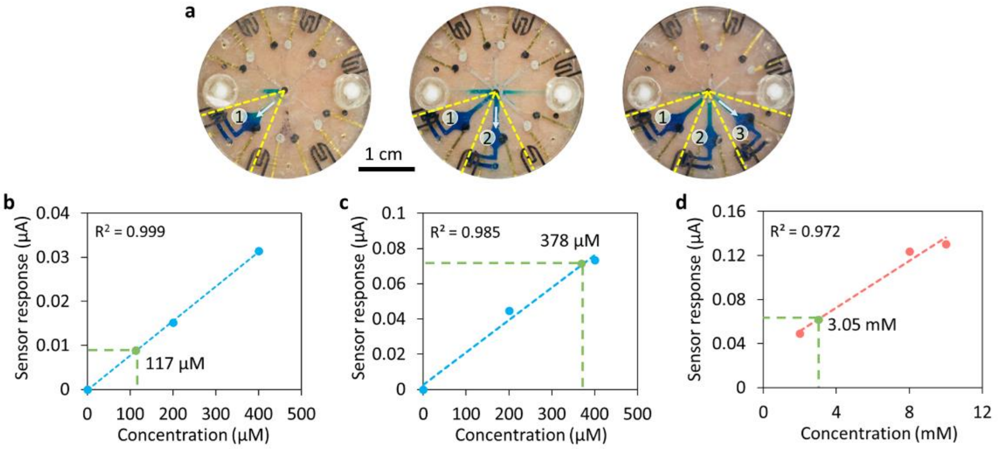

Figure 2. 32 *a) intermittent sample compartmentalization via sequential on-body valving (using blue dyes for visualization); b-d) On-body sweat glucose (b, c) and lactate (d) sensor readouts and the corresponding calibration curves. Sweat glucose readouts in (b) and (c) were obtained before and after beverage intake, respectively.*

2.4.3 Enhanced biochemical sensing based on ACET mixing

As the mechanism of wearable ACET mixing has been demonstrated in the section 2.3, here, we showed its utility in improving biochemical sensing performance. To demonstrate enhanced electrochemical sensing capability and as a proof of concept, we developed enzymatic sensor interfaces (patterned within our microfluidic module), which have been shown to be useful for the sensing a wide panel of biomarkers including metabolites (e.g., glucose and lactate) on-body. Accordingly, we specifically, devise H_2O_2-based enzymatic sensing interfaces. This is because H_2O_2 is the byproduct of oxidases (*e.g.*, glucose oxidase) that are often used as biorecognition elements.

The ability to fabricate multi-layered architectures was adapted to create a sandwiched-like actuation and sensing interface to further illustrate the value of the devised scheme in terms of enabling new degrees of freedom for device operation. To this end, we leveraged the vertical assembly approach, and incorporated electrode-patterned layers, which were aligned to face each other in order to realize a sandwiched-like interface, while forming the microfluidic channel (Fig. 2.33a). We specifically exploited this interface to demonstrate simultaneous ACET (with electrode pair on the ceiling) and electrochemical analysis (specifically, amperometric-based, with pre-functionalized electrode array on the bottom). The individual ACET and sensing electrode arrays, as well as the final assembled device are illustrated in Fig. 2.33b.

The design of the ACET electrode pair is based on a coplanar rotationally symmetric configuration [13]. The coplanar ACET electrode configuration allows for establishing a non-uniform electric field vector, which results in non-uniform joule heating and temperature gradient, and subsequently permittivity and conductivity gradients in the microfluidic channel. The interaction of the electric field with these gradient profiles results in body force acting on fluid, which in turn induces fluid motion. Figure 2.33c shows the corresponding simulated temperature profile as well as the induced micro-vortex-like flow pattern.

To demonstrate the enhancement of the electrochemical sensing performance enabled by the ACET actuation, first, we specifically characterized the effect of ACET actuation on H_2O_2 sensor amperometric response. Characterizing H_2O_2 sensing interface was motivated by the fact that H_2O_2 generation (proportional to the target concentration) is the last reaction step involved in a large group of enzymatic sensing mechanisms (specifically, oxidase-based). The calibration curve of the ACET actuation-assisted H_2O_2 sensor (with 3.5 V_{RMS} applied across ACET electrode pair) was obtained and compared to the corresponding calibration curve where ACET actuation was not activated (a representative H_2O_2 sensor response is shown in Fig. 2.33d, steady-state response shown in Fig. 2.34, reproduced results for two other sensors shown in Fig. 2.35). Collectively, the results indicate that the activation of the ACET electrodes resulted in the 47 %

and 26% enhancement in the H_2O_2 sensor output current level and sensitivity (defined as the slope of output current *vs.* analyte concentration, Fig. 2.33f), respectively.

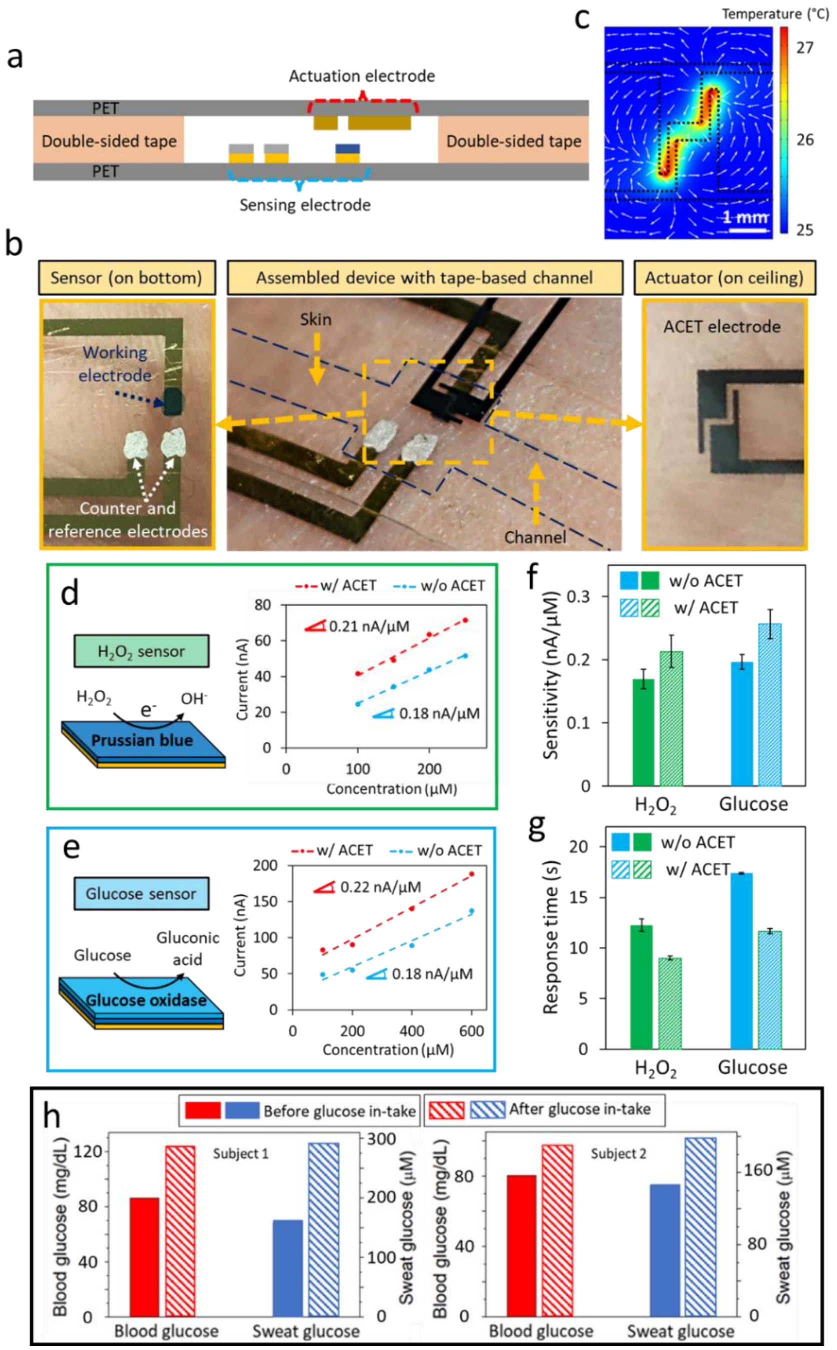

Figure 2. 33 *Sandwiched actuation and sensing interface: a) Cross-section schematic of the sandwiched-electrode array structure; b) Individual sensing (left) and actuation (right) electrode arrays, and final assembled device (middle, where the actuation electrode pair is aligned to face the sensor's working electrode); c) COMSOL ACET simulation (conductivity: 0.6 S/m, dielectric*

constant: 80, excitation: 3.5 V_{RMS}*, ambient temperature: 25 °C), illustrating the temperature profile and induced flow pattern established the rotationally symmetric electrode pair; d) Amperometric* H_2O_2 *sensing mechanism and corresponding calibration curves with and without ACET actuation; e) Enzymatic glucose sensing mechanism and corresponding calibration curves with and without ACET actuation; f, g) Comparison of corresponding amperometric sensors' sensitivities (f) and response time (g) with and without ACET actuation (error bars indicate standard error, N = 3); h) Comparison of blood and sweat glucose levels of two subjects during 12-h fasting and 0.5 h after glucose intake (30 g glucose), demonstrating the elevation of sweat glucose upon glucose intake, as measured by the actuation-assisted glucose sensor.*

Furthermore, as illustrated in Fig. 2.33g the H_2O_2 sensor response time is reduced by 27% when the ACET actuation was activated (example annotated sensor response for time response determination is shown in Fig. 2.36). In order to investigate this phenomenon in the context of enzymatic sensors, we studied the effect of ACET actuation on amperometric glucose sensor response, following the same characterization procedure (Fig. 2.33 e-g, Fig. 2.34-2.36). Collectively, the same trends in the enhancement of the glucose sensor response was observed (74% and 31% increase in the output current level and sensitivity, respectively, and 33% reduction in the response time). To further validate the enhancement of the enzymatic sensor response in the presence of ACET actuation, we constructed and characterized a choline enzymatic sensor, where we observed the similar trends (Fig. 2.37).

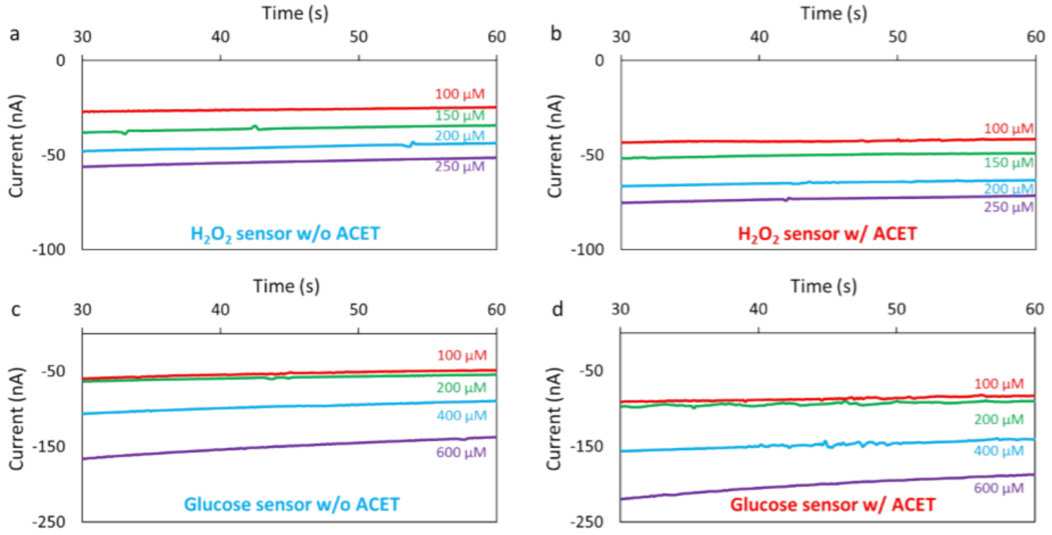

Figure 2. 34 *Recordings of the sensor steady-state responses shown in Fig. 2.33d,e: a)* H_2O_2 *without ACET actuation, b)* H_2O_2 *with ACET actuation, c) Glucose without ACET actuation, and d) Glucose with ACET actuation*

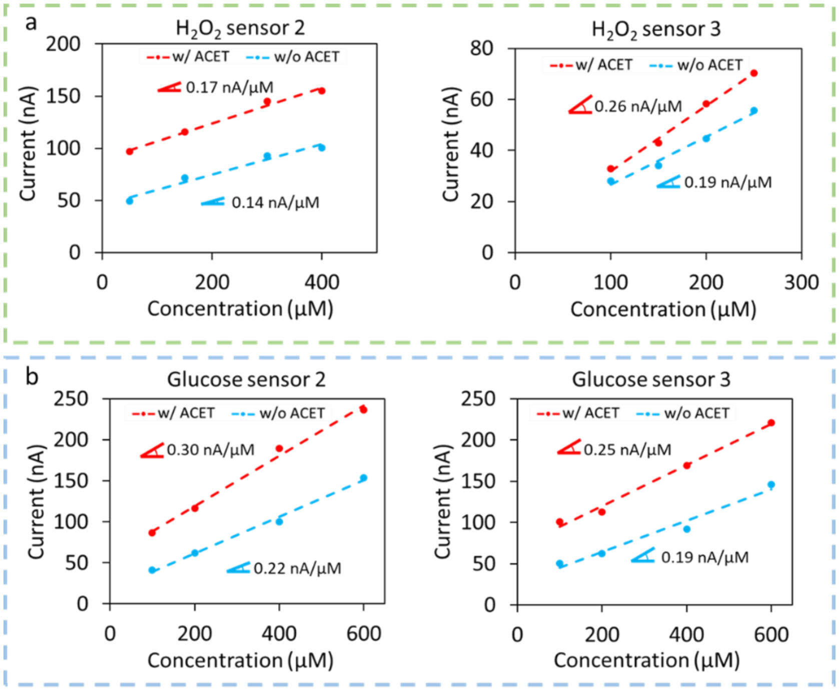

Figure 2. 35 *Reproduced sensor calibration results with and without ACET actuation: a)* H_2O_2 *sensor response and b) Glucose sensor response.*

The enhancement in the sensor response can be attributed to both the effect of mixing (overcoming diffusion) as well as local temperature increase (*e.g.*, enhanced reaction rate at the sensor surface). Given that the improvement of the sensitivity and reduction of response time in both glucose and choline cases were on the same order of magnitude as those for the case of H_2O_2, one may speculate that the acceleration of the H_2O_2 conversion and/or enhanced diffusion by ACET actuation plays a significant role in the sensor performance enhancement.

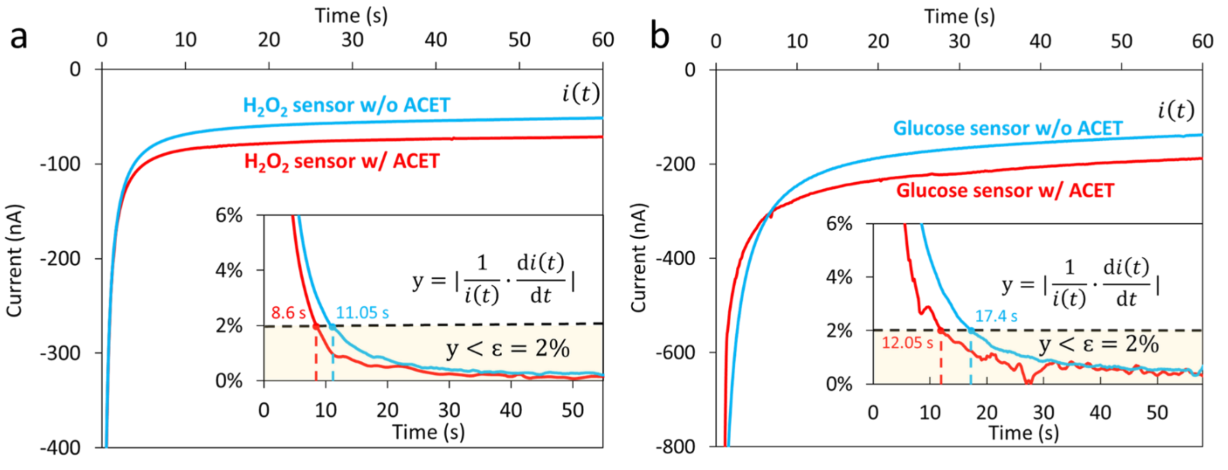

Figure 2. 36 *Recordings of the H_2O_2 (a) and glucose (b) sensors' amperometric responses with and without the presence of ACET. The corresponding insets show the normalized slope functions (see Materials and method section) for the determination of the sensors' response times.*

To validate the on-body operation of the devised actuation-assisted sensing interface, we performed human subject testing. Specifically, we demonstrated the elevation of sweat glucose after glucose intake in fasting subjects. Accordingly, standard iontophoresis protocol was followed for sweat stimulation of two healthy subjects during 12-h fasting and 0.5 h after consumption of 30 g of glucose. Upon each stimulation, the secreted sweat sample was interfaced with the ACET actuation-assisted glucose sensor (worn on body). As shown in Fig. 2.33h, the calibrated sweat sensor responses (measured in the presence of the ACET actuation, 3.5 V_{RMS}) for both subjects indicate the elevation of glucose level in sweat upon glucose intake, reflecting the elevation of glucose in blood.

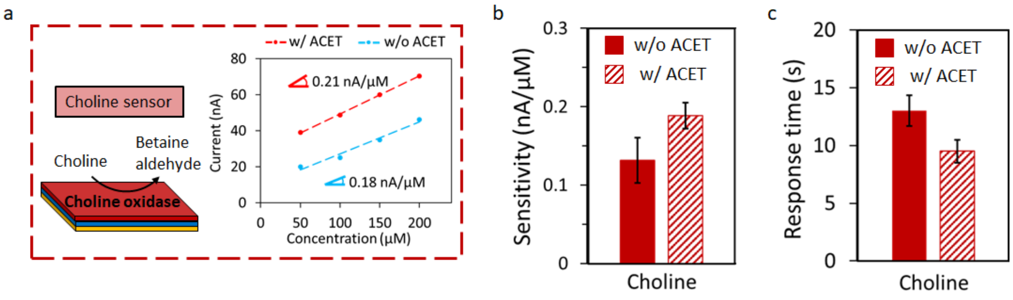

Figure 2. 37 *a) Enzymatic choline sensing mechanism and representative calibration curves of the sensor response (with and without ACET actuation). b, c) Comparison of choline sensor's sensitivity (b) and response time (c) for the cases of with and without ACET actuation (error bars indicate standard error, N = 3).*

2.4.4 References

1. Cheng, X. et al. A mediator-free electroenzymatic sensing methodology to mitigate ionic and electroactive interferents' effects for reliable wearable metabolite and nutrient monitoring. Adv. Funct. Mater. 30, 1908507 (2020).
2. Moyer, J., Wilson, D., Finkelshtein, I., Wong, B. & Potts, R. Correlation between sweat glucose and blood glucose in subjects with diabetes. Diabetes Technol. Ther. 14, 398–402 (2012).
3. Patterson, M. J., Galloway, S. D. & Nimmo, M. A. Variations in regional sweat composition in normal human males. Exp. Physiol. 85, 869–875 (2000).
4. Squires, T. M., Messinger, R. J. & Manalis, S. R. Making it stick: convection, reaction and diffusion in surface-based biosensors. Nat. Biotechnol. 26, 417–426 (2008).
5. Wang, J. & Musameh, M. Electrochemical detection of trace insulin at carbon-nanotube-modified electrodes. Anal. Chim. Acta 511, 33–36 (2004).
6. La Rosa, C., Pariente, F., Hernandez, L. & Lorenzo, E. Amperometric flow-through biosensor for the determination of pesticides. Anal. Chim. Acta 308, 129–136 (1995).
7. Lamberti, F. et al. Flow biosensing and sampling in indirect electrochemical detection. Biomicrofluidics 6, 024114 (2012).
8. Bard, A. J., Faulkner, L. R., Leddy, J. & Zoski, C. G. Electrochemical Methods: Fundamentals and Applications, Vol. 2 (Wiley New York, 1980).
9. Pontzer, H., Holloway, J. H. 4th, Raichlen, D. A. & Lieberman, D. E. Control and function of arm swing in human walking and running. J. Exp. Biol. 212, 523–534 (2009).

10. Huang, Z. et al. Three-dimensional integrated stretchable electronics. Nat. Electron 1, 473–480 (2018).
11. Thennadil, S. N. et al. Comparison of glucose concentration in interstitial fluid, and capillary and venous blood during rapid changes in blood glucose Levels. Diabetes Technol. Ther. 3, 357–365 (2001).
12. Derbyshire, P. J., Barr, H., Davis, F. & Higson, S. P. Lactate in human sweat: a critical review of research to the present day. J. Physiol. Sci. 62, 429–440 (2012).
13. Huang, S.-H., Wang, S.-K., Khoo, H. S. & Tseng, F.-G. AC Electroosmotic Generated In-Plane Microvortices for Stationary or Continuous Fluid Mixing. TRANSDUCERS 2007 - 2007 International Solid-State Sensors, Actuators and Microsystems Conference (2007) doi:10.1109/sensor.2007.4300392.

Chapter 3 Mobile point-of-person biochemical monitoring

3.1 Introduction

The advent of Industry 4.0 is pioneered by automated guided vehicles (AGV) that are widely used in distribution and supply chain logistics to perform autonomous, accurate, and consistent cargo transportation, while reducing transit times and labor costs [1]. The flexibility and scalability of such mobile automated systems, in conjunction with their ability to assign specific tasks to individual vehicles cooperating in a large network, provide new degrees of automation in comparison to physically constrained conveyor-belt or forklift-operated systems [2]. The same degrees of automation are poised to revolutionize point-of-person monitoring and applications such as medical diagnostics [3,4], -omics [5-7], drug development [8], and chemical/material synthesis [9]. In that regard, the full potential of these applications can be unlocked by adopting solutions centering on microfluidic logistics, herein defined as the detailed coordination of diverse, large-scale, and small-volume fluid handling operations to perform a plethora of sample processing and analysis tasks.

To this end, conventional continuous-flow microfluidic systems have shown high throughput and robust fluid handling capabilities [10-12]. However, their predefined fluid pathways and geometrically constrained operations severely limit their adaptability and automation, imposing the same limitations as conveyor-belt systems within larger-scale settings. Aiming to resolve such constraints, digital microfluidic actuation techniques such as electrowetting-on-dielectric (EWOD) have emerged, capable of transporting discrete droplets on an open surface in a programmable fashion [13-15]. However, inherent limitations of EWOD devices, stemming from the reliance on direct interactions between the solution and the electrified surfaces, can restrict their service life and compatibility with other peripheral components, thus narrowing their application diversity [16,17].

Here, inspired by the transformational impact of automated guided robotic systems on the manufacturing and distribution industries, we devised a robotic system which employs a network of individually addressable robots, each performing designated micro/nano-fluid manipulation-based tasks in cooperation with other robots. As illustrated in Fig. 3.1a, analogous to a standard AGV system, which consists of three primary entities, including a navigation floor, an electric motor, and a cargo carrier for package delivery, our robotic system can be described as: 1) an electromagnetic navigation floor, which can be programmed to establish localized electromagnetic (EM) fields in an addressable matrix of coils; 2) a millimeter-scale permanent magnet as a motor, the movement of which is controlled by the activated EM field(s); and 3) a ferrofluid droplet carrier, encapsulating the bio/chemical sample of interest (i.e., the "package"), which is set in motion upon experiencing strong body forces originating from the interaction of the ferrofluid's magnetic nanoparticle constituents with the motor's magnetic actuation field.

Effectively, the devised design leverages EM induction to achieve scalable control, and an intermediary EM-controlled permanent magnet to amplify the actuation field exerted on the ferrofluid (Fig. 3.1b). In this way, we overcome the fundamental limitations of previously reported magnetic digital microfluidics, which use complex translational stages and bulky magnets that are not portable [18,19] or electromagnetic coils [20,21] that lack the ample driving forces to execute efficient fluid operations. The addressability and strength of the ferrofluid actuation enables new degrees of mobility and automation central to the devised robotic system; hereafter, referred to as "ferrobotic system".

The contactless and high-strength nature of the ferrobotic actuation mechanism inherently renders it rapid, repeatable, and robust. These traits, together with the reconfigurability of the ferrobotic system, can be exploited to integrate passive and active functional components to implement advanced and diverse microfluidic operations (e.g., droplet dispensing, generation, merging, filtering) besides basic transportation operations (Fig. 3.1c). Depending on the objective at hand, a set of these operations can be combined within a disposable microfluidic architecture to deliver versatile system-level microfluidic functionalities.

This high degree of robustness and the individual addressability of ferrobots can be in turn leveraged to deploy a network of ferrobots that carry out generalizable cross-collaborative objectives, centering on microfluidic logistics, such as fluidic package sorting. To illustrate the utility of the ferrobotic system in diverse point-of-person monitoring application spaces, this system was specifically applied to execute a set of cross-collaborative and diverse operations, toward the quantification of active matrix metallopeptidases (MMP, a biomarker for cancer malignancy and inflammation) in human plasma [22-24], where its reconfigurable functionality and teamwork capability converged to implement a fully automated assay.

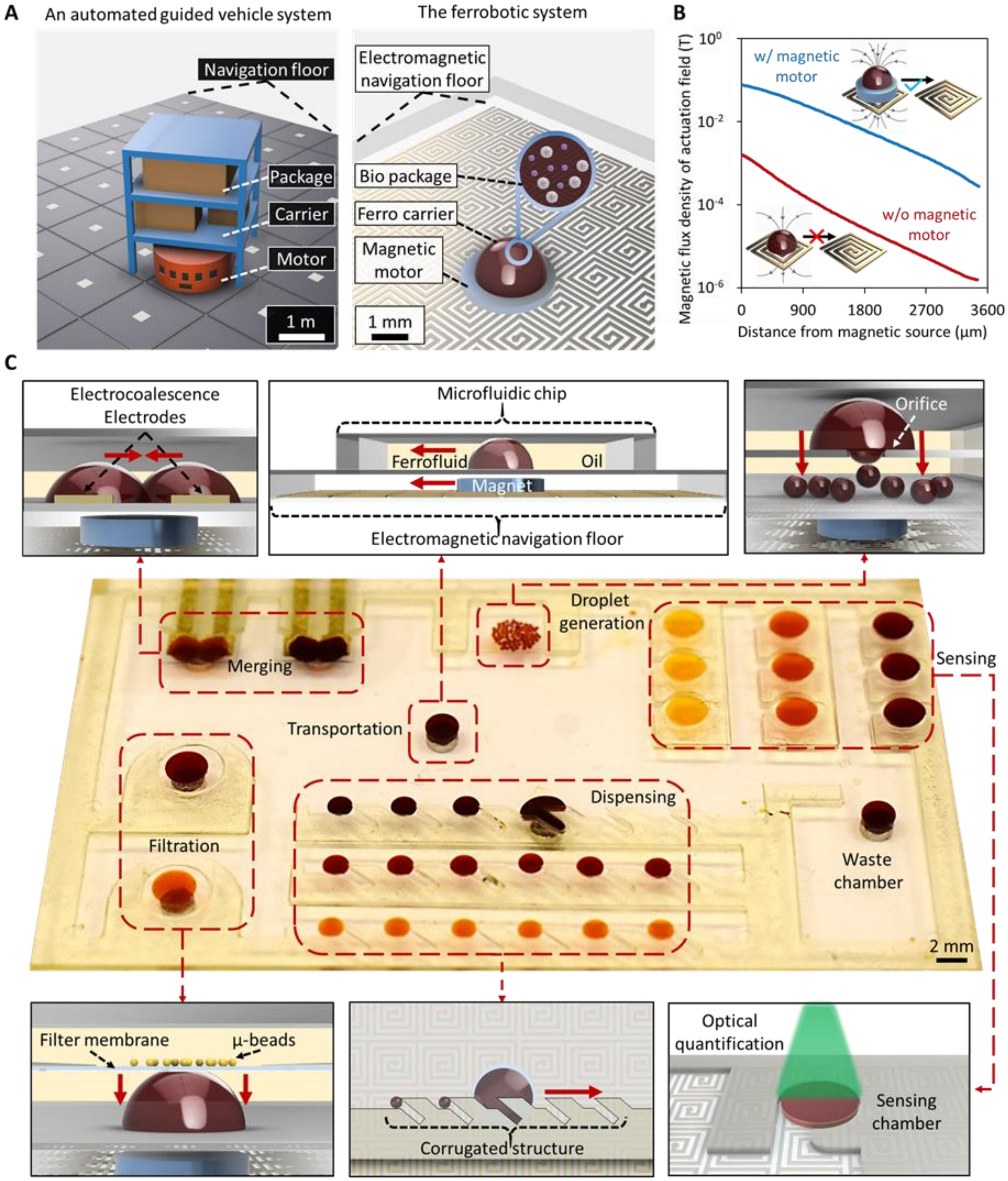
A
An automated guided vehicle system
Navigation floor
Package
Carrier
Motor
1 m
The ferrobotic system
Electromagnetic navigation floor
Bio package
Ferro carrier
Magnetic motor
1 mm
B
Magnetic flux density of actuation field (T)
10^0
10^{-2}
10^{-4}
10^{-6}
w/ magnetic motor
w/o magnetic motor
0
900
1800
2700
3600
Distance from magnetic source (μm)
C
Electrocoalescence Electrodes
Microfluidic chip
Ferrofluid
Oil
Magnet
Electromagnetic navigation floor
Orifice
Merging
Droplet generation
Sensing
Transportation
Filtration
Dispensing
Waste chamber
2 mm
Filter membrane
μ-beads
Corrugated structure
Optical quantification
Sensing chamber

Figure 3. 1 *The overview of ferrobotic system concept and mechanism. a) An analogy: mobility and automation in an AGV system and the devised ferrobotic system; b) Simulation results depicting the amplification of the actuation capability with the magnetic motor (the x-axis is the vertical distance from the center of the magnetic source); c) Optical image of a representative multifunctional ferrobotic system capable of performing diverse operations, including droplet package transportation, merging, generation, filtration, dispensing, and sensing. Rendered images* *of the droplets are for illustration purposes only (droplets can form hemisphere or disk-like shapes depending on the channel geometry).*

3.2 Amplified addressable electromagnetic actuation

By utilizing the electromagnetic coil matrix as the addressable actuator, and the millimeter-scale permanent magnet as the magnetic field actuation amplifier, robust ferrobotic fluid operations can be realized within a compact footprint. As seen in the magnetic field simulation results, illustrated in Fig. 3.1b and Fig. 3.2, the incorporated permanent magnet amplifies the actuation magnetic field by approximately two orders of magnitude (generated from passing of a 0.2 A DC current through the electromagnetic coil). In this way, high force actuation of relatively dilute magnetic solutions and/or smaller fluid volumes is achieved, rendering robust fluid transportation. Fluid transportation is the ferrobotic system's core functionality where an encapsulated package within the ferrofluidic carrier can be directed by the sequential activation of the EM coils along a desired route on the navigation floor.

The electromagnetic navigation floor on the PCB comprised an active matrix array of 32 × 32 electromagnetic coil elements. Each element had a 3-turn coil with a size of 1.5 × 1.5 mm stacked on three layers (Fig. 3.2). Adjacent coils were separated by a gap of 0.1mm, altogether, giving a total active area of the navigation floor of 51 × 51 mm. Each coil element can be activated when powered by a 0.2 A current, generating a localized magnetic force that attracted the magnetic motor. The specific coil selection was achieved by programming power switch ICs, including MAX14662 (Maxim Integrated, CA, USA) for row selection and MC33996 (NXP semiconductor, Netherlands) for column selection in the navigation floor. The target electromagnetic coil was selectively actuated when the corresponding row and column lines of its coordinate were activated by switch ICs. Switch ICs were linked by serial peripheral interface (SPI) wires to Arduino Nano, which communicated with a PC through serial communication. Target coordinates pre-programmed or sent from the user interface in the PC were translated to SPI commands by the MCU, then transmitted to switch ICs for addressable activation of the EM coils. The navigation floor was powered by an external power supply (Keithley 2230-30-1, Tektronix, OR, USA). A DC current source was used for EM coil activation, and the total current I followed the equation: $I = 0.2\ A \times N$ (N is the number of activated coils).

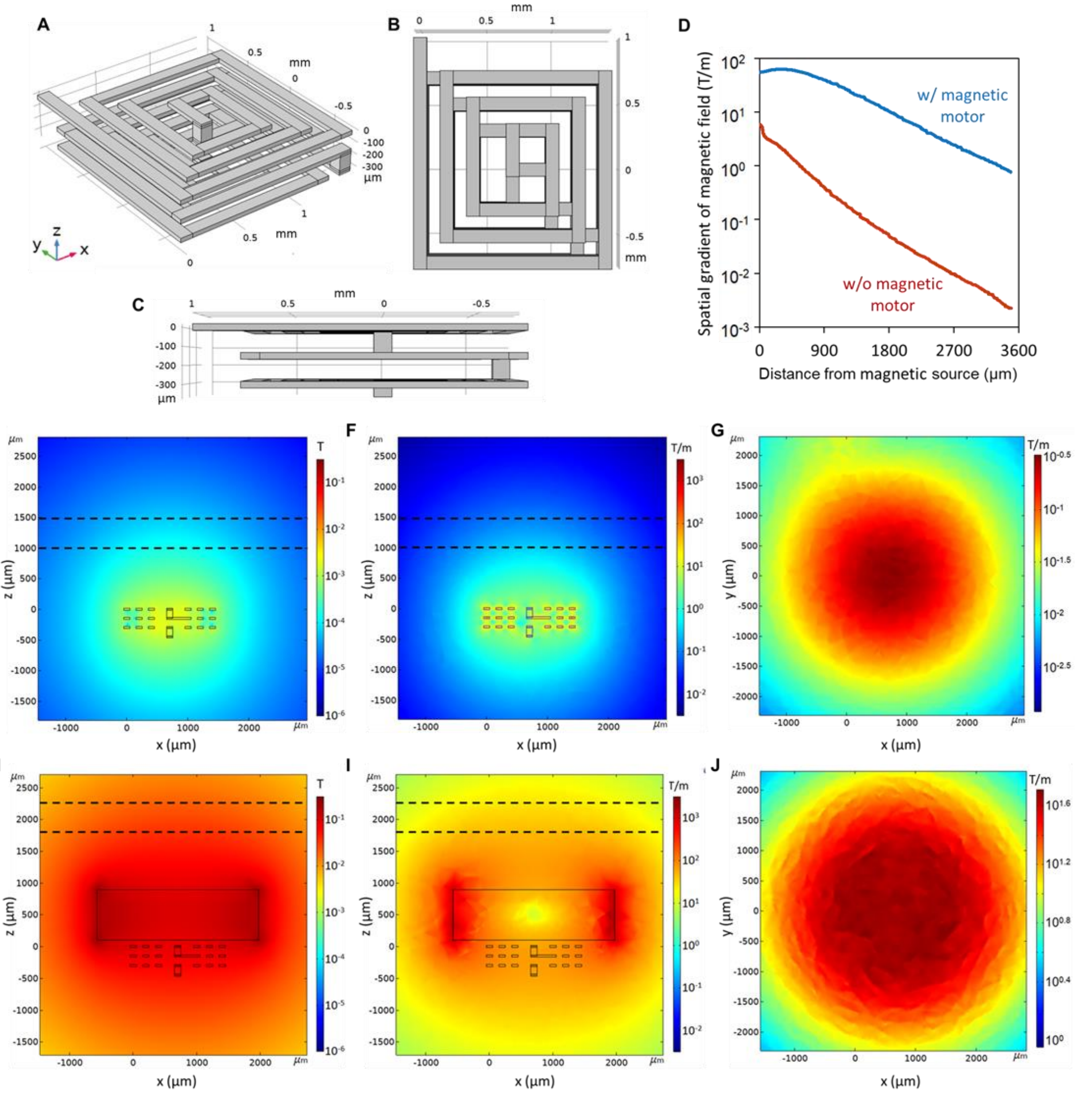

__Figure 3. 2__ EM-coil geometry and magnetic field simulation. Oblique (a), top (b) and side (c) view of the EM-coil's geometry; d) COMSOL simulation results of the spatial gradient of the magnetic field with and without the magnetic motor (i.e., the ferrobot). The x-axis is the distance from the

magnetic source center along the z-axis; e,f) magnetic field intensity (e) and spatial gradient of the magnetic field (f) in x-z plane in the absence of the ferrobot. The dashed lines outline the boundaries of the microfluidic chamber; g) spatial gradient of the magnetic field in x-y plane (1 mm above the coil) in the absence of the ferrobot; h,i) magnetic field intensity (H) and spatial gradient of the magnetic field (I) in x-z plane in the presence of the ferrobot. The dashed lines outline the boundaries of the microfluidic chamber; j) spatial gradient of the magnetic field in the x-y plane (1 mm above the coil) in the presence of the ferrobot.

The multi-layer implementation allows the proportional increase of the localized EM induction capability of each element for ferrobot attraction. To activate these elements in an addressable manner, two integrated circuit (IC) switches were incorporated in the PCB for row and column selection (Fig. 3.3a, b), which are connected to external power sources and controlled by a microcontroller unit (MCU). Depending on the task at hand, and by programming at the MCU level, these coils can be sequentially and/or simultaneously activated to engineer the desired paths for a single or multiple ferrobot(s). To illustrate this feature, we programmed the MCU to navigate single ferrobots through U-, C-, L-, and A-like routes (Fig. 3.3c), as well as four ferrobots to simultaneously trace the perimeter of a square-like route (Fig. 3.4). In all scenarios, the ferrobots successfully carried their designated loads.

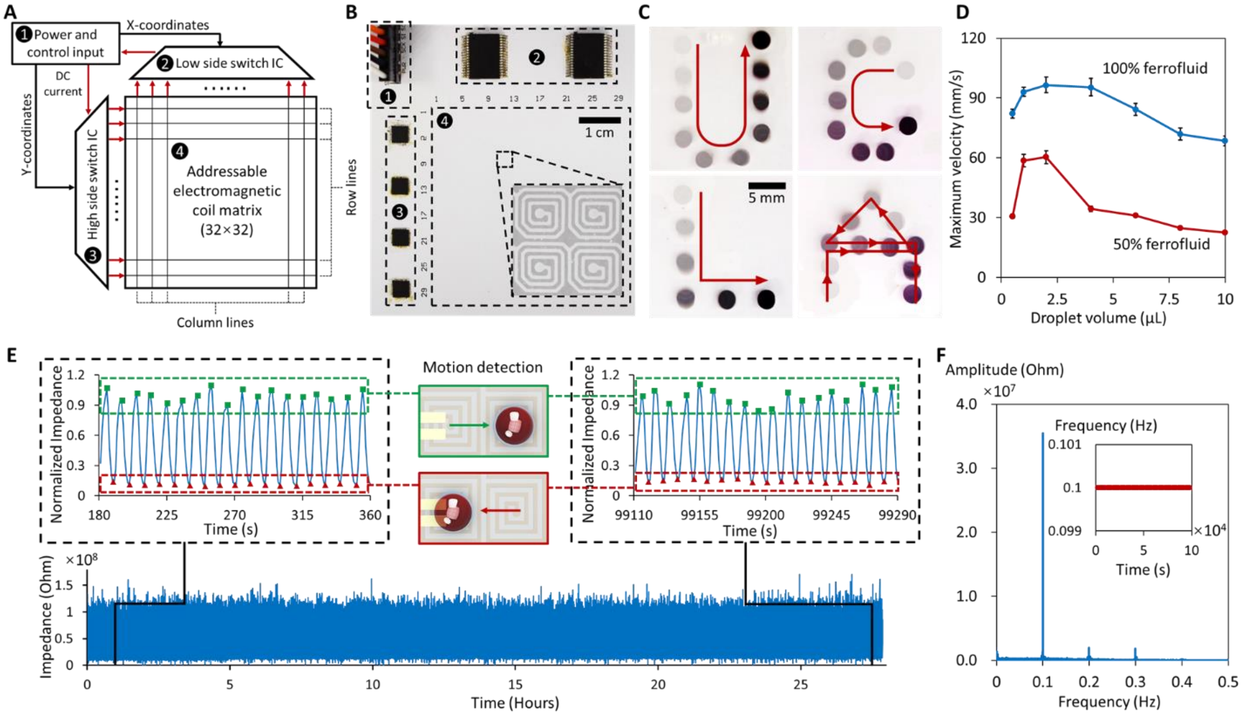

Figure 3. 3 *Design and characterization of the navigation floor for package transportation. a) Schematic diagram of the control circuitry; b) Optical image of the implemented control circuitry and the navigation floor with the close-up view of four neighboring EM coils; c) Overlaid sequential images (derived from video frames) visualize the commuted path of the ferrobot (programmed with different navigation plans; the duration for commuting "U", "C", "L" and "A" paths were correspondingly 1.4 s, 1.4 s, 0.7 s, and 2.3 s); d) Characterization of the maximum transportation velocity for two different ferrofluid concentrations. Error bars indicate standard error (n = 3); e) Characterization of the oscillatory transportation of a package with a ferrobot (sensed with an impedance sensing electrode pair) to evaluate the robustness of the ferrobotic actuation (performed for > 24 hours); f) FFT analysis of the oscillatory profile measured by the impedance sensing electrodes in part (e). Inset shows variation of the fundamental frequency of the 2000 s-segmented time windows, depicting near zero variation.*

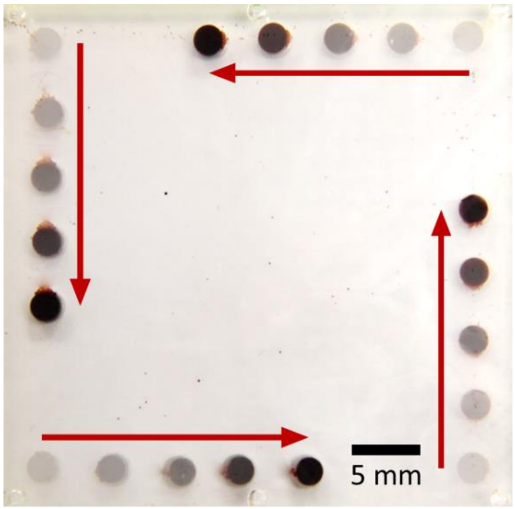

Figure 3. 4 *Multi-ferrobot transportation. Overlaid sequential images visualize the commuted paths of the four simultaneously commuting ferrobots (duration: 7 s).*

As shown in Fig. 3.3d and Fig. 3.5, with the devised approach, maximum droplet transportation velocities on the order of 10 cm/s can be achieved. To characterize the maximum transportation velocity, a microfluidic device with a 40 × 40 × 1.5 mm inner chamber was fabricated, assembled and filled with oil. The device was placed 2 mm above the navigation floor. A magnetic motor was placed on top of the navigation floor and below the microfluidic device. Ferrofluid droplets with volume gradients of 0.5-10 µL (0.5, 1, 2, 4, 6, 8, 10 µL) and two different concentrations, (100% and 50% ferumoxytol dilution in DI water) were loaded in the microfluidic chamber. These droplets moved along with the ferrobot, which was guided by the EM coils actuation in one row from left (y = 1) to right (y = 32) sequentially. The velocity of the ferrobot was controlled by adjusting the time interval between activating two adjacent coils. If the ferrofluid droplet followed the magnetic motor to the end successfully, the velocity of the magnet would increase by shortening the actuation time interval (by 1 ms) in the next round, until the droplet failed to follow the magnet.

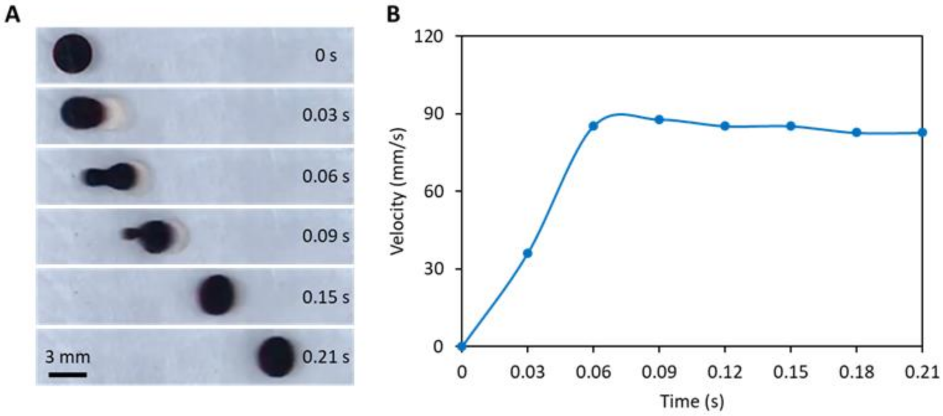

Figure 3. 5 *Characterization of the average velocity profile of the droplet. a) Sequential imaging of a representative droplet moving along the navigation floor; b) Corresponding measured averaged velocity.*

The maximum velocity of the droplet initially increases along with its size, showing the dominance of the driving magnetic force on relatively small droplets. The following decrease in maximum velocity illustrates the increased dominance of frictional forces beyond a certain droplet size (for an expanded discussion on this topic, please refer to Appendix E). The same trend is observed for a more diluted ferrofluid concentration (50% dilution by volume, also shown in Fig. 3.3d). Here, the droplet volume characterization range is chosen based on the envisioned microfluidic droplet applications (e.g., the MMP assay).

The contactless aspect of the actuation mechanism (i.e., no ferrobotic surface interaction with the package or the surrounding fluid) inherently renders it repeatable and durable, in contrast with contact-based EWOD actuation that is susceptible to surface degradation [16, 17, 25, 26]. To demonstrate the durability of our ferrobotic system, an illustrative continuous characterization experiment was performed, which involved a 10,000-cycle automated oscillatory transport (frequency: 0.1 Hz) of a package over the duration of > 24 hours (Fig. 3.3e). Specifically, A microfluidic device with a 20 × 20 × 0.7 mm chamber was fabricated and assembled, with a pair of gold electrodes deposited on the substrate as an impedance sensor. A 2 µL ferrofluid droplet was loaded in the oil-filled microfluidic chamber. A magnetic motor was actuated to carry the droplet back-and-forth between two locations periodically (0.1 Hz). In each cycle, the droplet was first carried away from the sensing electrodes, consequently raising the impedance signal, then carried back in contact with the electrodes causing the impedance signal to drop. These actions were repeatedly is performed for over 100,000 seconds in order to finish 10,000 cycles. The electrodes were connected to a potentiostat (CH Instrument 660E, TX, USA) and impedance (at 1 kHz) was measured between the two electrodes (Fig. 3.6a), patterned on the substrate of a microfluidic chip. The electrodes were used to continuously track the entrance/departure of the package through monitoring the impedance signal change (correspondingly leading to an increased/decreased measured impedance, annotated in green/red, Fig. 3.3e). Fast Fourier Transform (FFT) analysis of the continuously recorded data (Fig. 3.3f) yielded an output fundamental frequency of 0.100 Hz, which matches the input actuation frequency at the MCU level. Furthermore, the detailed FFT analysis of the 2000 s-segmented time windows yielded less than 0.01% variation in the motion frequency of the package. We also performed oscillatory droplet transport experiments at 1 Hz with water- and plasma-based droplets (over 1000 cycles). The FFT analysis, shown in Fig. 3.6b, c, indicates that repeatable oscillatory motions are achieved for both droplet samples. It is worth noting that beyond ~10 Hz, the droplet cannot be effectively manipulated because this leads to a velocity that exceeds the maximum velocity threshold.

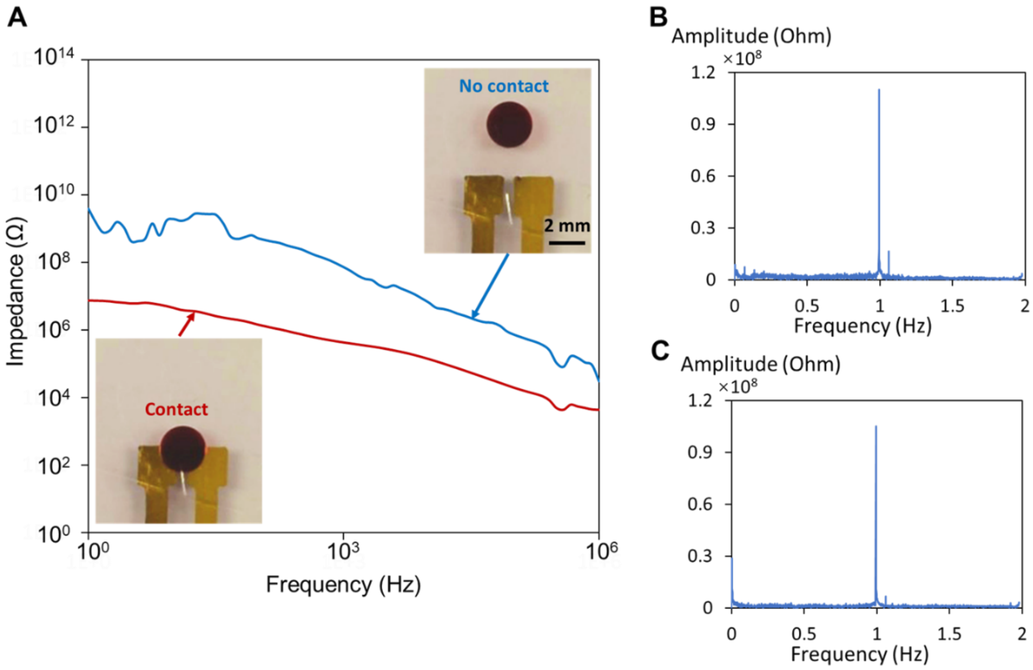

Figure 3. 6 *Impedance spectrum measured by the impedance sensing electrode pair. a) The impedance spectrum shows distinct impedance differences when the ferrobot is present vs. not present (inset shows the droplet position with respect to the sensing electrodes for the corresponding measurements); b,c) Corresponding FFT of the impedance measurements tracking the oscillatory motion (1 Hz, over 1000 cycles) of the droplet with compositions: (b) 50% ferrofluid (diluted in water) and (c) 50% ferrofluid (diluted in plasma).*

3.3 Functional components for advanced operations: droplet dispensing, generation, merging, and filtration

The high-strength and contactless aspects of the devised actuation mechanism can be exploited to conveniently interface the loaded package with different passive and active peripheral components and microfluidic structures in all three spatial dimensions, thus enabling operations of interest in a reconfigurable manner. For example, by carrying the package against a corrugated microfluidic structure formed in the $x - y$ plane, droplet dispensing can be achieved. Moreover, by delivering the droplet package within a multi-layered chamber, and through VIA (vertical interconnect access) and membranes along a z axis, droplet generation and filtering can be realized.

Furthermore, without causing physical/field interference, droplets can be delivered to active electro-fluidic interfaces to render complementary actuation mechanisms such as electrocoalescence for droplet merging.

3.3.1 Dispensing

Droplet dispensing is a precise liquid-handling capability that is useful for applications such as drug discovery, quantitative biology, and chemical analysis [27,28]. To implement the dispensing of uniformly sized droplets with the ferrobotic system, a microfluidic architecture with a corrugated wall structure was utilized. As demonstrated in Fig. 3.7a, a "parent" droplet package is guided by a ferrobot underneath the microfluidic chip. When it is transported along the corrugated structure, smaller "child" droplets are dispensed. As shown in Fig. 3.7b, the parent droplet starts moving along the corrugated wall at t = 0 s. After the droplet passes the corrugated structure at t = 1 s, due to geometric pinching, a small volume of the droplet breaks away from the parent and enters the structure. The corrugated structure can be extended into an array format to dispense multiple droplets. As shown in the final step of Fig. 3.7b, three homogenous droplets (1.63±0.09 µL) are dispensed. To study the level of control that our system has on the dispensed droplet sizes, we designed and tested various corrugated-opening widths. The results show that by increasing the corrugated-opening width, the dispensed droplet volume can be modulated from 0.5 and 4 µL (Fig 3.7c). The same trend is observed for diluted ferrofluid concentrations (10% and 50% dilutions by volume, Fig. 3.8). If larger dispensed droplet volumes are needed, a larger magnet in addition to an enlarged corrugated-opening width may be required.

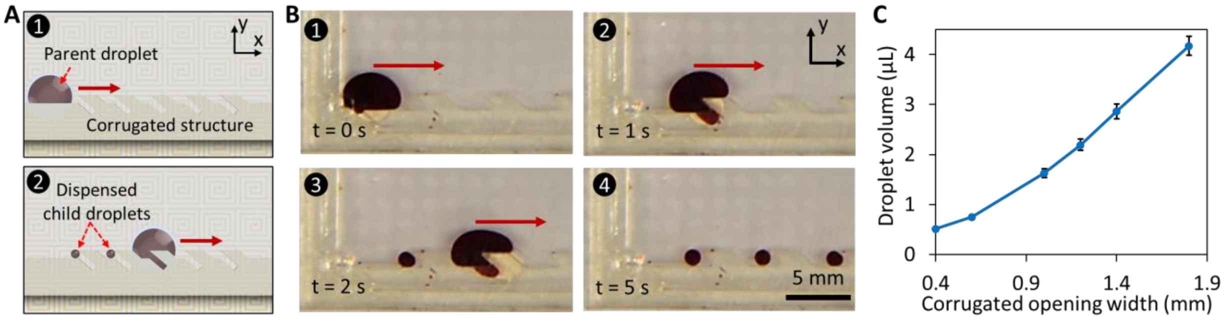
A
①
Parent droplet
Corrugated structure
②
Dispensed
child droplets
y
x
B
①
t = 0 s
②
t = 1 s
③
t = 2 s
④
t = 5 s
5 mm
C
Droplet volume (µL)
0
1
2
3
4
0.4
0.9
1.4
1.9
Corrugated opening width (mm)

***Figure 3. 7** a) Schematic illustration of the droplet dispensing mechanism, involving the transportation of the package against a corrugated microfluidic wall; b) Sequential optical images of the droplet dispensing process; c) Characterization of the dispensed droplets' size for different corrugated opening widths. Error bars indicate standard error (n = 10).*

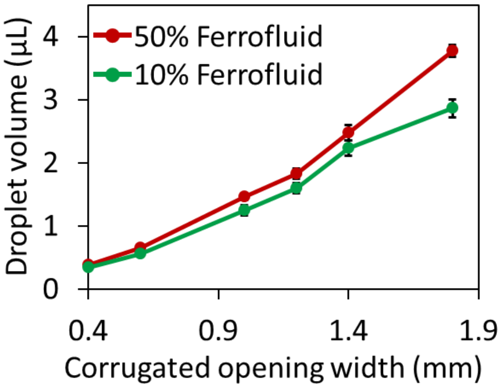

***Figure 3. 8** Dispensed droplet characterization. Characterization of the dispensed droplets' size for different corrugated opening widths and using two ferrofluid concentrations. Error bars indicate standard error (n = 10).*

3.3.2 Generation

Furthermore, higher throughput and smaller volume droplet generation can be realized by incorporating an orifice-like VIA connecting neighboring layers in a multi-layer microfluidic architecture. As schematically illustrated in Fig. 3.9a, when the parent droplet is guided through the upper layer to the top of the orifice, it is attracted towards the lower layer by the vertically exerted magnetic force from the ferrobot. Every time a critical volume of the droplet passes the orifice, it breaks off into a child droplet. As shown in Fig. 3.9b, the following sequential events occur: 1) the transport of the parent droplet (in the upper layer) to an orifice; 2) the positioning of the parent droplet on the orifice to generate child droplets; and 3) the departure of the parent droplet, leaving behind the generated child droplets (in the lower layer). By adjusting the width of the junction orifice, the droplet volume (~10-125 nL) and the generation rate can be tuned (Fig. 3.9c, Fig. 3.10). Such nL-generated droplets can also be further manipulated by the ferrobot (Fig. 3.11).

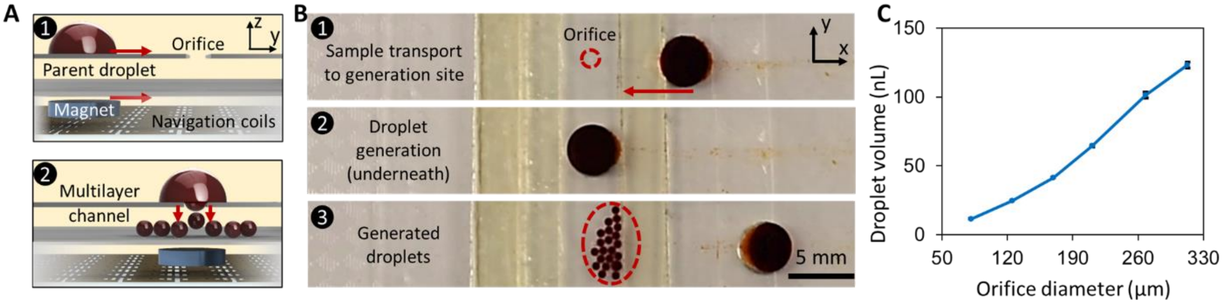
A
①
Orifice
z
y
Parent droplet
Magnet
Navigation coils
②
Multilayer
channel
B
①
Sample transport
to generation site
Orifice
y
x
②
Droplet
generation
(underneath)
③
Generated
droplets
5 mm
C
150
100
50
0
Droplet volume (nL)
50
120
190
260
330
Orifice diameter (μm)

Figure 3. 9 *a) Schematic illustration of the droplet generation process, involving the droplet transportation to a VIA-like orifice; b) Sequential optical images of the droplet generation process; c) Characterization of the generated droplets' volume for different orifice diameters. Error bars indicate standard error (n = 20).*

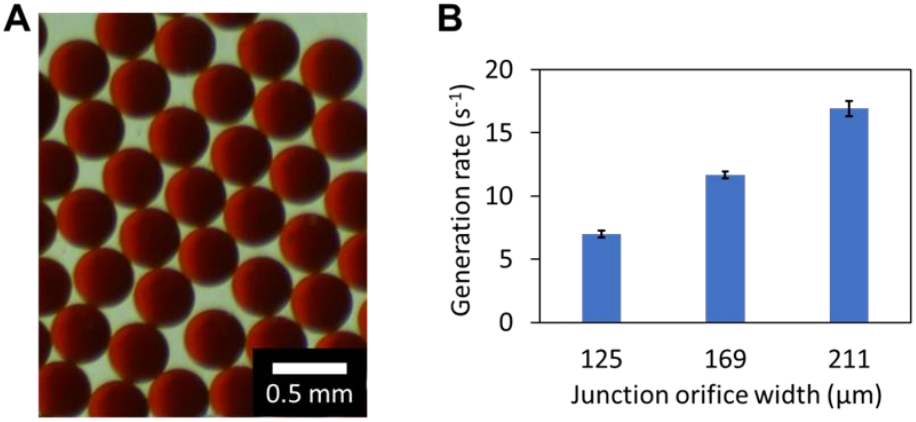

Figure 3. 10 *Droplet generation characterization. a) Optical microscopic images of generated droplets using 169 μm-diameter orifice; b) Characterization of droplet generation rate for varying orifice diameters (based on counting the generated droplets over 4 s).*

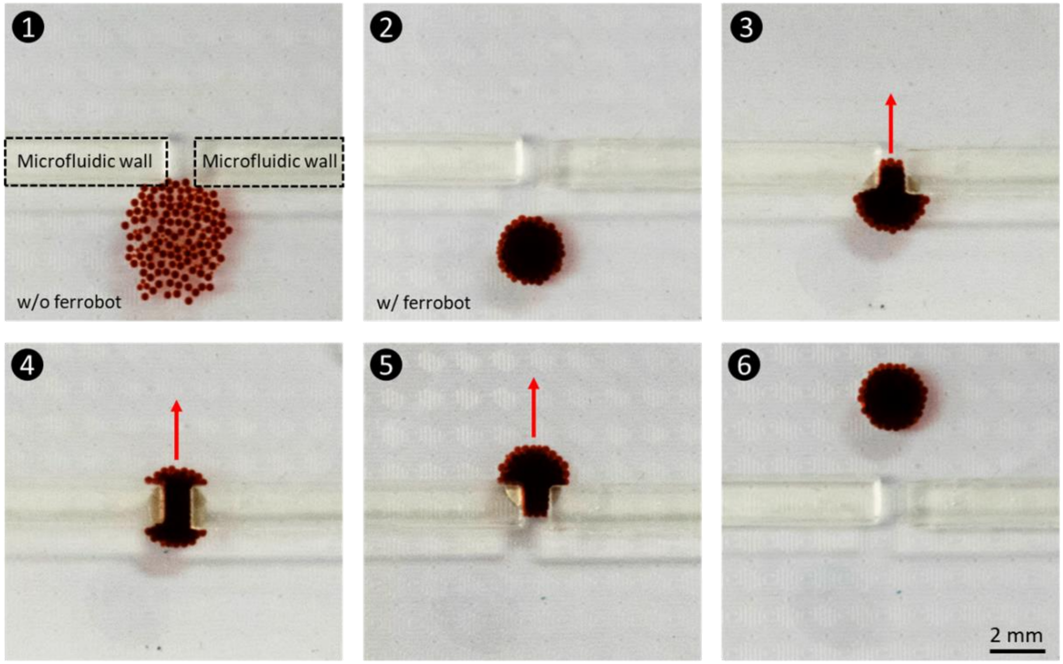

Figure 3. 11 *Collective transportation of nL-droplets by a ferrobot. Sequential imaging indicates the collection and transportation of generated nL-droplets by a ferrobot through a 2 mm-wide × 1mm-long pore.*

3.3.3 Filtration

Microfluidic filtration is one of the key sample processing procedures required for applications such as cell separation [29,30]. Here, by incorporating a membrane between the two layers of the microfluidic device, size-based filtration is realized. As schematically shown in Fig. 3.12a, the contactless magnetic force exerted by the ferrobot causes the droplet to be pulled through the filter to the lower layer, leaving behind particles that are too large to pass through. Specifically, here, a membrane with a size cut-off of 10-μm is used to filter out μ-beads of 25 μm diameter. To quantify the filtration capability, the ferrofluid droplet is optically imaged before and after the filtration procedure. As can be seen from Fig. 3.12b, 25 μm μ-beads can be observed in the droplet prior to filtration, and are subsequently filtered out, as evident from the post-filtration optical analysis results (three trials, Fig. 3.12c).

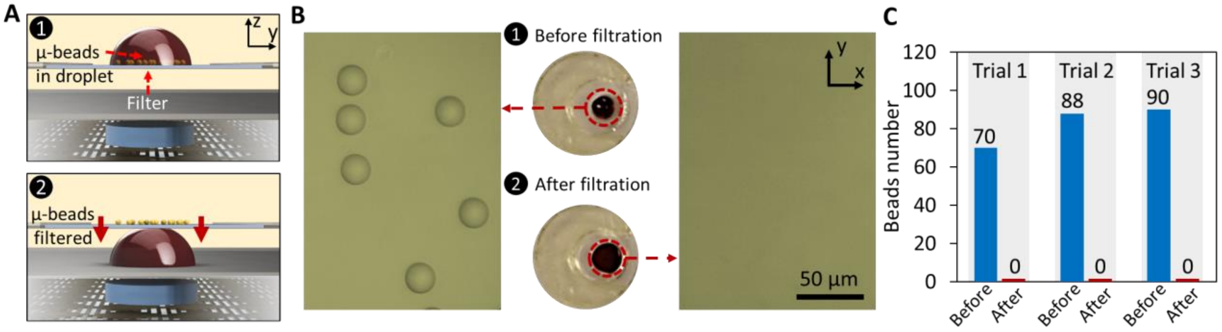

Figure 3. 12 *a) Schematic illustration of the filtration mechanism; b) Optical image of the solution sample before and after filtration; c) Bead counts before and after filtration (three trials).*

3.3.4 Merging and mixing

Droplet merging allows for timed and metered addition of reagents and can play a critical role in performing droplet-based biological assays, aiming to measure DNA/RNA, protein, and cell properties in samples [31-35]. Here, to achieve the merging of droplets in the ferrobotic system, we leverage electrocoalescence as a complementary actuation mechanism which is non-interfering with the contactless ferrobotic actuation (Fig. 3.13). Accordingly, electrocoalescence is realized by applying 2 V across a pair of gold electrodes (2 mm × 2 mm, spaced 1 mm apart, patterned on the substrate of the microfluidic device). Figure 3.13b show that upon applying 2 V, two droplets delivered in the vicinity of the electrodes coalesce. To achieve homogeneous and evenly distributed droplet contents after merging, chaotic fluid motion within the merged droplet can be induced by actuating neighboring electromagnetic coils with a frequency of 10 Hz in a cyclic fashion, resulting in an oscillatory motion of the ferrobot within the confines of the coil's coordinates. This cyclic motion creates folding flows in alternating directions to effectively render mixing. Figure 3.13b visually demonstrates the significant effect of the devised active mixing on shortening the time required to achieve homogeneity in a merged droplet. To quantify this effect, optical analysis on the merged red/green droplet is performed by defining a mixing index. The results are illustrated in Fig. 3.13c, demonstrating that a near-homogenous profile is achieved within ~15 s using active mixing, which is substantially shorter than without active mixing.

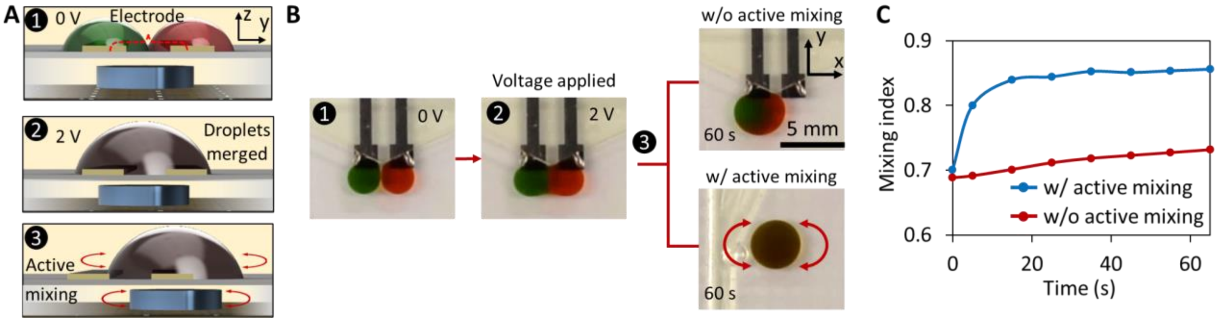

Figure 3. 13 *a) Schematic illustration of droplet merging and mixing mechanisms; b) Optical images to visualize the droplet merging (upon applying 2 V) and mixing process (with and without active mixing); c) Comparison of the progressive mixing index for the two cases of with and without active mixing.*

3.4 Efficient achievement of objectives with a cross-collaborative network of ferrobots

The robustness and addressability of the ferrobotic system can be leveraged to deploy fleets of ferrobots to dynamically accomplish collaborative tasks in parallel, toward the more efficient achievement of a common objective. Here, as an example, a package-sorting mission is assigned to the ferrobotic system, where the objective is to sort randomly-sequenced packages into a sorted sequence of increasing droplet volumes. Figure 3.14a illustrates the system-level view of the sorting procedure, which includes: 1) loading of multiple packages of various sizes into the ferrobotic system with random relative positions; 2) top-view image acquisition of the packages on the navigation floor to identify the package sizes and positions; 3) computationally deriving the navigation plan to formulate the detailed tasks for the ferrobots in accordance to the “merge sort” algorithm [36] and the acquired size and position information; and 4) communicating the corresponding assigned tasks for each of the ferrobots with the aid of the on-board microcontroller, to achieve the overarching sorting objective.

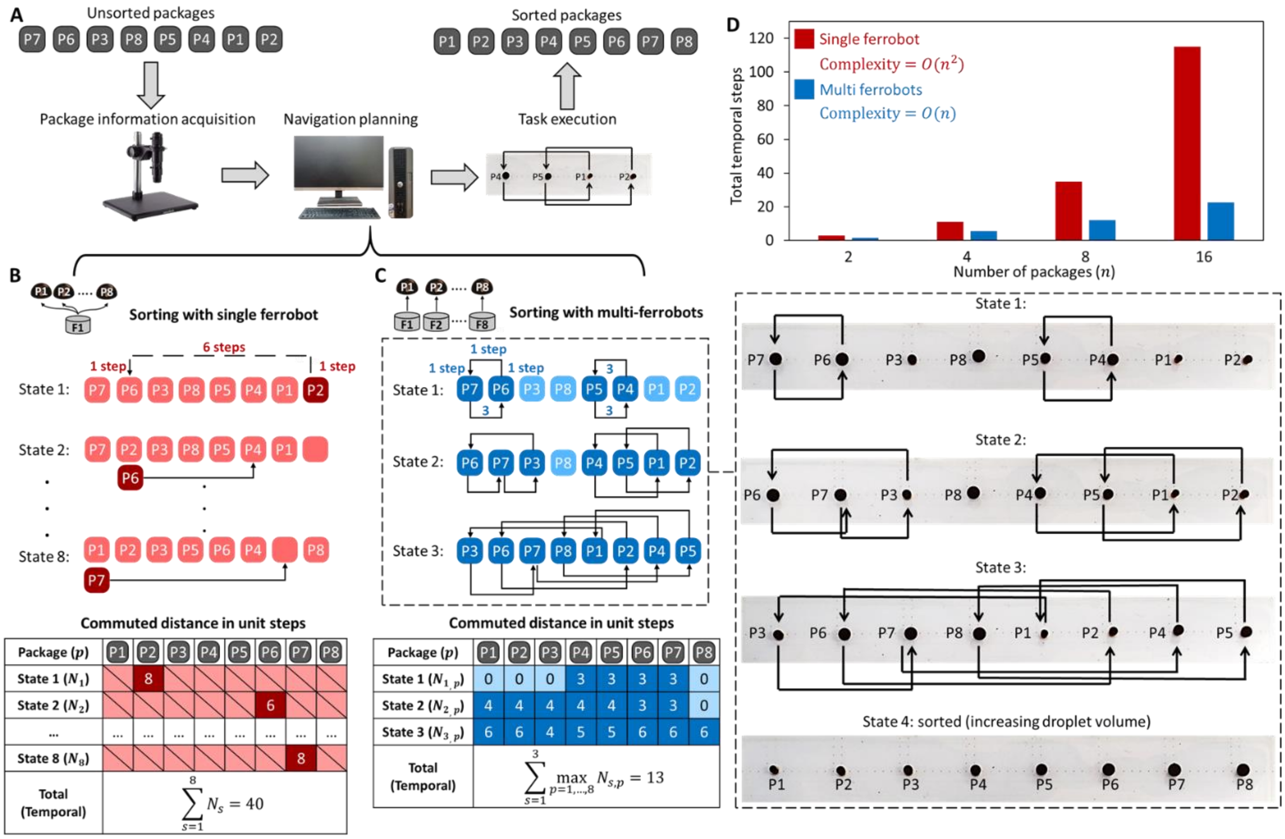
A
Unsorted packages
P7 P6 P3 P8 P5 P4 P1 P2
Package information acquisition
Navigation planning
Task execution
Sorted packages
P1 P2 P3 P4 P5 P6 P7 P8
B
Sorting with single ferrobot
6 steps
1 step
State 1:
State 2:
State 8:
Commuted distance in unit steps
C
Sorting with multi-ferrobots
State 1:
State 2:
State 3:
Commuted distance in unit steps
D
Single ferrobot
Complexity = $O(n^2)$
Multi ferrobots
Complexity = $O(n)$
Total temporal steps
Number of packages (n)
State 1:
State 2:
State 3:
State 4: sorted (increasing droplet volume)

Package (p)	P1	P2	P3	P4	P5	P6	P7	P8
State 1 (N_1)		8						
State 2 (N_2)						6		
...	...	...	...	...	...	...	...	...
State 8 (N_8)							8	
Total (Temporal)	$\sum_{s=1}^{8} N_s = 40$							

Package (p)	P1	P2	P3	P4	P5	P6	P7	P8
State 1 (N_{1_p})	0	0	0	3	3	3	3	0
State 2 (N_{2_p})	4	4	4	4	4	3	3	0
State 3 (N_{3_p})	6	6	4	5	5	6	6	6
Total (Temporal)	$\sum_{s=1}^{3} \max_{p=1,\ldots,8} N_{s,p} = 13$							

Figure 3. 14 *Efficient package sorting with a cross-collaborative network of ferrobots. a)System-level view of the sorting procedure; b,c) Comparison of the sorting efficiency achieved by (b) a single ferrobot and (c) eight ferrobots tasked with sorting a random sequence of eight packages. State-by-state transitions for both scenarios are illustrated and the table details the commuted distance of each ferrobot (left). The snapshots from the sorting experiment performed with eight ferrobots are shown on the right (captured at the end of each state); d) the total temporal unit steps required for sorting 2, 4, 8, and 16 packages (based on statistical averaging of all the possible permutations).*

To particularly demonstrate the degree of efficiency that can be attained when deploying a cross-collaborative network of ferrobots, the n-package sorting performance achieved by a team of n ferrobots was compared against that achieved by a single ferrobot on the basis of the completion time (as detailed in Fig. 3.14b, c, for an illustrative case of n = 8).

When only one ferrobot is used for sorting, it is responsible for the delivery of all the packages by itself. At each state (defined as the period during which the available ferrobot starts and finishes one round of package delivery), only one package can be moved to its target location.

In order to quantitatively characterize the sorting efficiency, a “unit step” which equals to the distance between two navigation coils is defined to measure the distance that the ferrobots will move. For example, referring to Fig. 3.14b, at state 1, the ferrobot moves 8 unit steps (2 vertical steps and 6 horizontal steps) to deliver package 2 (“P2”) from position 8 to position 2. Since only one ferrobot is performing the task, the “temporal steps” (number of steps, which determine the maximum time elapsed over the course of a state) required to complete sorting are equal to the total unit steps moved by the single ferrobot. In the example shown, it takes the single ferrobot a total of 40 temporal steps to meet the sorting objective.

When multiple ferrobots are deployed (Fig. 3.14c), each ferrobot is charged with moving one package, and they can move in parallel with other ferrobots during the same state (following the computationally derived navigation plan in accordance with the “merge sort” algorithm, Fig. 3.15a). The corresponding experiment is visualized in Fig. 3.14c (right panel). In this scenario, the number of temporal steps for each state is determined by the maximum steps taken by a ferrobot within the team, because the ferrobots are delivering packages in parallel. For example, referring to Fig. 3.14c, in state 2, among 8 ferrobots, one ferrobot moves 0 steps, two ferrobots move 3 steps, and five ferrobots move 4 steps, yielding 4 temporal steps for that state. The total number of temporal steps to achieve the sorting objective is also equal to the sum of temporal steps for each state, which is 13 for the illustrated example. By comparison, for this illustrative example, sorting using multiple ferrobots results in about 300% increased efficiency as compared to the single ferrobot case. This degree of improvement achieved due to the deployment of a cross-collaborative network of ferrobots will be even higher for the cases requiring sorting of a larger number of packages (i.e., larger n). That is because, the complexity of the mission at hand for the case of a single ferrobot increases as $O(n^2)$, while for the case of multiple ferrobots it increases linearly (i.e., $O(n)$). To reinforce this point, as shown in Fig. 3.14d we derived the total temporal unit steps for the cases of n = 2, 4, 8, and 16, based on statistical averaging of all the possible permutations (consistent with the trend observed when simulating 10,000 randomly generated sequences of n packages, Fig. 3.15b). Altogether, the results presented within the framework of this generalizable objective illustrate the utility of the deployment of a network of ferrobots to achieve the objective at hand efficiently as well as the suitability of the ferrobotic system for microfluidic logistics.

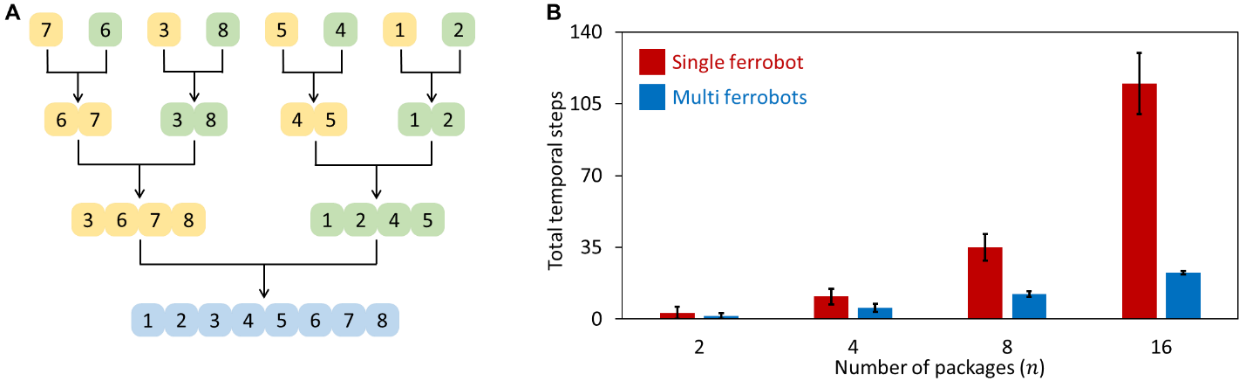

Figure 3. 15 *Merge sort algorithm and sorting performance for single vs. multi ferrobots. a) Representative schematic of the application of recursive merge sort algorithm to sort an array of 8 integers; b) The averaged total temporal unit steps required for sorting n = 2, 4, 8, and 16 packages, performed with a single or n ferrobots (simulated based on 10,000 randomly generated sequence of packages for each scenario, error bars indicate standard deviation).*

3.5 Application of the ferrobotic system: automated matrix metallopeptidases bioassay

Leveraging the demonstrated capability of the ferrobotic system to deliver advanced and cross-collaborative operations, we implemented a pipelined and automated bioassay equipped with a dynamic self-calibration mechanism, as an example utility of the presented technology in diverse application spaces centering on microfluidic logistics. Accordingly, the ferrobotic logistics were adapted to quantify MMP concentrations in human plasma, a biomarker extensively studied and reported as an immunological indicator, wherein the elevation of plasma MMP concentration is associated with physiological and pathological processes such as cancer metastasis [22,23,37], sepsis onset [38-40], immune activation [24, 41], and wounding healing [42,43].

Figure 3.16a illustrates the workflow of the MMP assay, which is based on the fluorescent quantification of the enzymatic activity of MMPs from a test sample (introduced into the input well) as well as the calibrator samples, indicated by the intensity of fluorescent signals. To realize an automatic self-calibration mechanism, pre-loaded source samples (introduced at the source well array, with known concentrations of the MMP collagenase) are used for the construction of calibrator samples in-situ, providing optional flexibility to dynamically construct new calibrator concentrations (e.g., [C_2] in Fig. 3.16a). To facilitate optical readout, a FRET (Fluorescence Resonance Energy Transfer)-based MMP substrate is pre-loaded in the calibration well array and the output well (designated for test sample analysis). The self-calibration capability of the assay establishes a standard curve *in situ* and concurrently with the testing assay, which is particularly useful for mitigating systematic error typically associated with fluorescence spectrometry and ensuring the accuracy of the measurements [44].

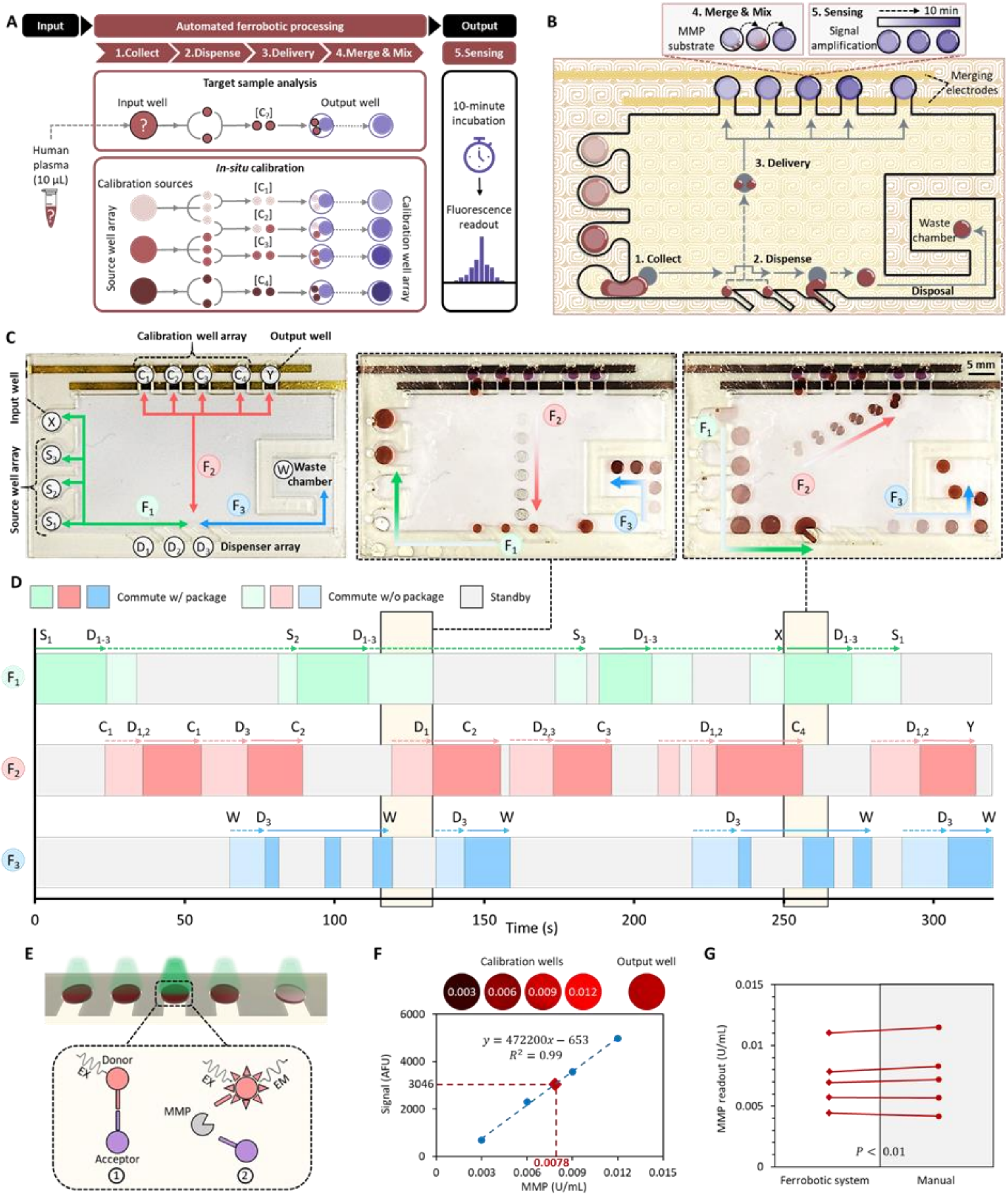
A
Input
Automated ferrobotic processing
Output
1.Collect
2.Dispense
3.Delivery
4.Merge & Mix
5.Sensing
Target sample analysis
Input well
Output well
?
[C?]
Human plasma (10 μL)
In-situ calibration
Calibration sources
Source well array
[C1]
[C2]
[C3]
[C4]
Calibration well array
10-minute incubation
Fluorescence readout
B
4. Merge & Mix
MMP substrate
5. Sensing
10 min
Signal amplification
Merging electrodes
3. Delivery
Waste chamber
1. Collect
2. Dispense
Disposal
C
Calibration well array
Output well
Input well
Source well array
C1
C2
C3
C4
Y
X
S3
S2
S1
F1
F2
F3
W Waste chamber
D1
D2
D3
Dispenser array
5 mm
D
Commute w/ package
Commute w/o package
Standby
S1
D1-3
S2
S3
X
C1
D1,2
D3
C2
D1
D2,3
C3
C4
Y
W
Time (s)
0
50
100
150
200
250
300
E
Donor
EX
Acceptor
①
MMP
EM
②
F
Calibration wells
Output well
0.003
0.006
0.009
0.012
y = 472200x − 653
R² = 0.99
Signal (AFU)
6000
4000
3046
2000
0
0.0078
0.015
MMP (U/mL)
G
0.015
0.01
0.005
MMP readout (U/mL)
P < 0.01
Ferrobotic system
Manual

Figure 3. 16 *Pipelined and automated MMP assay, performed by the ferrobotic system. a) General workflow of the MMP assay equipped with a dynamic self-calibration mechanism; b) Illustration of the ferrobotic tasks in relation to the navigation floor over the processing of a representative sample (performed by three ferrobots); c) Overview of the navigation plans of the three deployed ferrobots (F_1, F_2, and F_3) with annotated locations of interest; d) The detailed timeline of the ferrobots' status (commuting with/without package, standby), with annotated locations of interest.*

Overlaid sequential video frames illustrating the status at two representative stages; e) Illustration of the FRET pair from the MMP substrate cleaved by the MMPs present in the sample to yield a fluorescent product that is no longer quenched; f) The fluorescent readouts from the calibration and output wells, after automated ferrobotic processing and 10 minutes of incubation. The concentration of MMP in the test sample is estimated with the aid of a real-time calibration standard curve generated from the 4 calibrator samples (estimated: 0.0078 U/mL vs. expected: 0.008 U/mL); g) Estimated MMP concentrations in five tested human plasma samples (performed by the ferrobotic system and manually by a technician, $p < 0.01$).

The ferrobotic system was programmed to implement the steps of the automated assay within a microfluidic architecture, including 1) sample collection, 2) dispensing (to ensure uniform sample volume), 3) delivery, and 4) merging (with the aid of an electrocoalescence electrode pair) and mixing for sensing (Fig. 3.16b). Specifically, three ferrobots (F1, F2, and F3) were utilized to carry out the required tasks in a pipelined manner. The overview of the navigation plans of the three ferrobots is shown in Fig. 3.16c. In this regard, ferrobot F_1 is in charge of collecting and dispensing the source and test samples into smaller uniform droplets. Ferrobot F_2 is responsible for delivering the dispensed droplets to the designated detection wells, and ferrobot F_3 is tasked with removing the dispensed droplet residues to the waste chamber. The detailed timeline of the task sequence executed by each ferrobot in coordination with the other two ferrobots, along with representative snapshots of the navigation floor status, are illustrated in Fig. 3.16c, d.

Upon delivering the dispensed calibrator/test sample droplets to the calibration well array/output well, the electrocoalescence electrode pair (a single pair patterned across all the detection wells) is activated, merging the delivered droplets with the pre-loaded MMP substrate within each well all at once. To achieve a homogenous mixture after merging, ferrobot F2 can induce a chaotic internal flow. Upon merging and mixing of the samples with MMP substrate, enzymatic reactions (Fig. 3.16e) effectively commence at the same time, resulting in the generation of fluorescent signal proportional to the respective MMP content in a well. The fluorescent signals are quantitively analyzed by fluorescence microscopy. The linearity of the fluorescent signals with the MMP content of a sample was validated by spiking collagenase in a phosphate-buffered saline (PBS) buffer at different levels and reading out fluorescence after a 10 min incubation (Fig. 3.17). To evaluate the analytical accuracy of the ferrobotic assay for measuring the MMP content in human plasma, four calibrator samples with collagenase concentration of 0.003, 0.006, 0.009, 0.012 Wünsch U/mL were used to determine the MMP concentration of a test sample (human plasma spiked with MMP at a collagenase concentration of 0.008 U/mL). As illustrated in Fig. 3.16f, by referring to the real-time standard curve generated by the calibrator samples, the test sample MMP content was measured to be 0.0078 U/mL ± 0.0005 U/mL (based on 95% confidence interval). To further evaluate the analytical performance of the ferrobotic assay, four additional test samples were analyzed by the ferrobotic system, as well as by a technician using manual pipetting steps and a plate reader [45]. As shown in Fig. 3.16g, the readouts obtained from the ferrobotic system closely matched those analyzed using standard manual analysis ($P < 0.01$), which in turn illustrates the successful execution of all ferrobotic instructions with a high degree of and robustness and precision. This pipelined assay exemplifies the capacity of the ferrobotic system to perform highly quantitative biochemical processes with a high level of integration and automation.

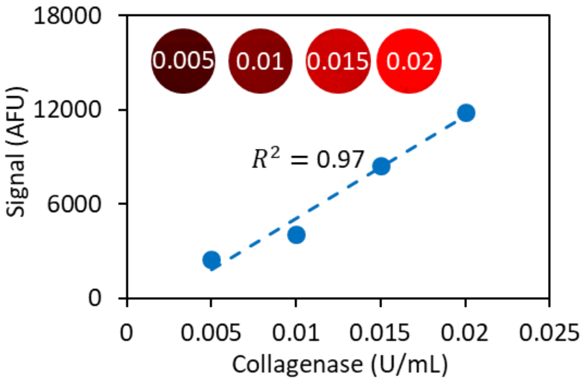

Figure 3. 17 *Characterization of the MMP assay. The recorded fluorescence signals from the calibration well array, where each well contains PBS dilutions of collagenase at different end concentrations.*

3.6 References

1. J. Lambert, How Robots Change the World (Oxford Economics, 2019), vol. 43, pp. 5–8.
2. J.-T. Li, H.-L. Liu, Design optimization of amazon robotics. Automat. Contr. Intel. Syst. 4, 48–52 (2016).
3. A. H. C. Ng, R. Fobel, C. Fobel, J. Lamanna, D. G. Rackus, A. Summers, C. Dixon, M. D. M. Dryden, C. Lam, M. Ho, N. S. Mufti, V. Lee, M. A. M. Asri, E. A. Sykes, M. D. Chamberlain, R. Joseph, M. Ope, H. M. Scobie, A. Knipes, P. A. Rota, N. Marano, P. M. Chege, M. Njuguna, R. Nzunza, N. Kisangau, J. Kiogora, M. Karuingi, J. W. Burton, P. Borus, E. Lam, A. R. Wheeler, A digital microfluidic system for serological immunoassays in remote settings. Sci. Transl. Med. 10, eaar6076 (2018).
4. V. Srinivasan, V. K. Pamula, R. B. Fair, An integrated digital microfluidic lab-on-a-chip for clinical diagnostics on human physiological fluids. Lab Chip 4, 310–315 (2004).
5. A. H. C. Ng, M. D. Chamberlain, H. Situ, V. Lee, A. R. Wheeler, Digital microfluidic immunocytochemistry in single cells. Nat. Commun. 6, 7513 (2015).
6. A. R. Wheeler, H. Moon, C. A. Bird, R. R. O. Loo, C.-J. C. J. Kim, J. A. Loo, R. L. Garrell, Digital microfluidics with in-line sample purification for proteomics analyses with MALDI-MS. Anal. Chem. 77, 534–540 (2005).
7. A. Stark, D. J. Shin, T.-H. Wang, A sample-to-answer droplet magnetofluidic assay platform for quantitative methylation-specific PCR. Biomed. Microdevices 20, 31 (2018).
8. A. Stark, D. J. Shin, T.-H. Wang, A sample-to-answer droplet magnetofluidic assay platform for quantitative methylation-specific PCR. Biomed. Microdevices 20, 31 (2018).

9. H. Ding, S. Sadeghi, G. J. Shah, S. Chen, P. Y. Keng, C.-J. C. J. Kim, R. M. van Dam, Accurate dispensing of volatile reagents on demand for chemical reactions in EWOD chips. Lab Chip 12, 3331–3340 (2012).
10. M. Antfolk, T. Laurell, Continuous flow microfluidic separation and processing of rare cells and bioparticles found in blood – A review. Anal. Chim. Acta 965, 9–35 (2017).
11. M. Karle, S. K. Vashist, R. Zengerle, F. von Stetten, Microfluidic solutions enabling continuous processing and monitoring of biological samples: A review. Anal. Chim. Acta 929, 1–22 (2016).
12. D. Di Carlo, D. Irimia, R. G. Tompkins, M. Toner, Continuous inertial focusing, ordering, and separation of particles in microchannels. Proc. Natl. Acad. Sci. U.S.A. 104, 18892–18897 (2007).
13. M. Abdelgawad, A. R. Wheeler, The digital revolution: A new paradigm for microfluidics. Adv. Mater. 21, 920–925 (2009).
14. M. G. Pollack, R. B. Fair, A. D. Shenderov, Electrowetting-based actuation of liquid droplets for microfluidic applications. Appl. Phys. Lett. 77, 1725 (2000).
15. K. Choi, A. H. C. Ng, R. Fobel, A. R. Wheeler, Digital Microfluidics. Annu. Rev. Anal. Chem. 5, 413–440 (2012).
16. M. Mibus, G. Zangari, Performance and reliability of electrowetting-on-dielectric (EWOD) systems based on tantalum oxide. ACS Appl. Mater. Interfaces 9, 42278–42286 (2017).
17. Y. Zhang, N.-T. Nguyen, Magnetic digital microfluidics- A review. Lab Chip 17, 994–1008 (2017).

18. J. Pipper, Y. Zhang, P. Neuzil, T.-M. Hsieh, Clockwork PCR including sample preparation. Angew. Chem. Int. Ed. Engl. 47, 3900–3904 (2008).
19. W. H. Koh, K. S. Lok, N.-T. Nguyen, A digital micro magnetofluidic platform for lab-on-achip applications. J. Fluids Eng. 135, 021302 (2013).
20. U. Lehmann, C. Vandevyver, V. K. Parashar, M. A. M. Gijs, Droplet-based DNA purification in a magnetic lab-on-a-chip. Angew. Chem. Int. Ed. Engl. 45, 3062–3067 (2006).
21. C.-H. Chiou, D. J. Shin, Y. Zhang, T.-H. Wang, Topography-assisted electromagnetic platform for blood-to-PCR in a droplet. Biosens. Bioelectron. 50, 91–99 (2013).
22. M. Egeblad, Z. Werb, New functions for the matrix metalloproteinases in cancer progression. Nat. Rev. Cancer 2, 161–174 (2002).
23. L. Sevenich, J. A. Joyce, Pericellular proteolysis in cancer. Genes Dev. 28, 2331–2347 (2014).
24. W. C. Parks, C. L. Wilson, Y. S. López-Boado, Matrix metalloproteinases as modulators of inflammation and innate immunity. Nat. Rev. Immunol. 4, 617–629 (2004).
25. I. Swyer, R. Fobel, A. R. Wheeler, Velocity saturation in digital microfluidics. Langmuir 35, 5342–5352 (2019).
26. J. Li, N. S. Ha, T. Liu, R. M. vanDam, C.-J. Kim, Ionic-surfactant-mediated electro-dewetting for digital microfluidics. Nature 572, 507–510 (2019).
27. S. Kahkeshani, J. E. Kong, Q. Wei, D. Tseng, O. B. Garner, A. Ozcan, D. Di Carlo, Ferrodrop dose-optimized digital quantification of biomolecules in low-volume samples. Anal. Chem. 90, 8881–8888 (2018).

28. S. Kahkeshani, D. Di Carlo, Drop formation using ferrofluids driven magnetically in a step emulsification device. Lab Chip 16, 2474–2480 (2016).
29. Y. Cheng, X. Ye, Z. Ma, S. Xie, W. Wang, High-throughput and clogging-free microfluidic filtration platform for on-chip cell separation from undiluted whole blood. Biomicrofluidics 10, 014118 (2016).
30. X. Qiu, J. A. Lombardo, T. M. Westerhof, M. Pennell, A. Ng, H. Alshetaiwi, B. M. Luna, E. L. Nelson, K. Kessenbrock, E. E. Hui, J. B. Haun, Microfluidic filter device with nylon mesh membranes efficiently dissociates cell aggregates and digested tissue into single cells. Lab Chip 18, 2776–2786 (2018).
31. B. Bhattacharjee, S. A. Vanapalli, Electrocoalescence based serial dilution of microfluidic droplets. Biomicrofluidics 8, 044111 (2014).
32. R. Tewhey, J. B. Warner, M. Nakano, B. Libby, M. Medkova, P. H. David, S. K. Kotsopoulos, M. L. Samuels, J. B. Hutchison, J. W. Larson, E. J. Topol, M. P. Weiner, O. Harismendy, J. Olson, D. R. Link, K. A. Frazer, Microdroplet-based PCR enrichment for large-scale targeted sequencing. Nat. Biotechnol. 27, 1025–1031 (2009).
33. D. J. Eastburn, A. Sciambi, A. R. Abate, Picoinjection enables digital detection of RNA with droplet rt-PCR. PLOS One. 8, e62961 (2013).
34. A. R. Wheeler, H. Moon, C.-J. Kim, J. A. Loo, R. L. Garrell, Electrowetting-based microfluidics for analysis of peptides and proteins by matrix-assisted laser desorption/ ionization mass spectrometry. Anal. Chem. 76, 4833–4838 (2004).
35. A. H. C. Ng, B. B. Li, M. D. Chamberlain, A. R. Wheeler, Digital microfluidic cell culture. Annu. Rev. Biomed. Eng. 17, 91–112 (2015).
36. R. Cole, Parallel merge sort. SIAM J. Comput. 17, 770–785 (1988)

37. M. Dhar, J. N. Lam, T. Walser, S. M. Dubinett, M. B. Rettig, D. Di Carlo, Functional profiling of circulating tumor cells with an integrated vortex capture and single-cell protease activity assay. Proc. Natl. Acad. Sci. U.S.A. 115, 9986–9991 (2018).
38. R. E. Vandenbroucke, L. Dejager, C. Libert, The first MMP in sepsis. EMBO Mol. Med. 3, 367–369 (2011).
39. G. Martin, V. Asensi, A. H. Montes, J. Collazos, V. Alvarez, J. A. Carton, F. Taboada, E. Valle-Garay, Role of plasma matrix-metalloproteases (MMPs) and their polymorphisms (SNPs) in sepsis development and outcome in ICU patients. Sci. Rep. 4, 5002 (2014).
40. I. Vanlaere, C. Libert, Matrix metalloproteinases as drug targets in infections caused by gram-negative bacteria and in septic shock. Clin. Microbiol. Rev. 22, 224–239 (2009).
41. L. Nissinen, V.-M. Kähäri, Matrix metalloproteinases in inflammation. Biochim. Biophys. Acta. 1840, 2571–2580 (2014).
42. L. Ravanti, V. M. Kähäri, Matrix metalloproteinases in wound repair (review). Int. J. Mol. Med. 6, 391–407 (2000).
43. A. Gutiérrez-Fernández, M. Inada, M. Balbín, A. Fueyo, A. S. Pitiot, A. Astudillo, K. Hirose, M. Hirata, S. D. Shapiro, A. Noël, Z. Werb, S. M. Krane, C. López-Otín, X. S. Puente, Increased inflammation delays wound healing in mice deficient in collagenase-2 (MMP-8). FASEB J. 21, 2580–2591 (2007).
44. E. M. Miller, A. R. Wheeler, A Digital microfluidic approach to homogeneous enzyme assays. Anal. Chem. 80, 1614–1619 (2008).
45. D. H. Nam, X. Ge, Development of a periplasmic FRET screening method for protease inhibitory antibodies. Biotechnol. Bioeng. 110, 2856–2864 (2013).

Chapter 4 Conclusions and prospects

In overall, this dissertation introduces new wearable and mobile bioanalytical systems that are uniquely positioned to support health monitoring at the point-of-person.

For the wearable system, we devised a simple, scalable, and low-cost “CAD-to-3D Device” fabrication and integration scheme, which renders 3D and complex microfluidic architectures for the on-body sweat sampling. The spatial efficiency and new degrees of freedom achieved by the rendered 3D and multi-layered microfluidic architectures allows for the incorporation of a multitude of bioanalytical operations such as biofluid management, processing, and sensing.

By devising a network of individually addressable microheater-controlled thermo-responsive hydrogel valves, we achieved *in situ* active biofluid management, which is central to the realization of autonomous and advanced biofluid processing and analysis capabilities underpinning the envisioned lab-on-body platforms. A devised electronic-hydraulic analogy provided the basis for developing a pressure regulation mechanism (integrated within the microfluidic valving system), which was used to harvest biofluid, in situ, from pressure-driven bio-interfaces (here, sweat glands). The active fluid control achieved by this valving system is harnessed to create new wearable bioanalytical capabilities at both the sensor and system levels. At the sensor level, the valving capability is exploited to decouple the previously overlooked issue (in wearable biosensing) of flow rate influence on sensor response. At the system level, addressable biofluid routing and compartmentalization achieved by valving were leveraged to implement programmable sensor selection/protection. Through integration with an FPCB and seamless bilateral communication with consumer electronics, the valving system was adapted for on-body biomarker analysis, where the demonstrated capabilities converged to render contextually relevant (scheduled/on-demand) biomarker data acquisition. While here, we demonstrated wearable valving in the context of exercise-induced sweat sample compartmentalization, the presented technology can be equivalently adopted for the compartmentalization of iontophoretically induced sweat. In that regard, a dedicated programmable iontophoresis interface can be integrated, which enables contextually relevant sweat sampling in sedentary subjects.

By exploiting the ACET effects and engineering the biofluid flow profiles on the body, fluid processing functionalities such as pumping, and mixing can be achieved in the wearable format. The wearable ACET flow is induced using corrosion-resistant electrode configurations (fabricated on a flexible substrate and embedded within a microfluidic module) and custom-developed, wirelessly programmable high frequency (MHz) excitation circuitry. Various tunable flow profiles were demonstrated with the aid of the devised flexible ACET electrode configurations, where the induced profiles were in agreement with the ACET theory and simulation. The presented platform overcomes the limitations of previously demonstrated wearable bioanalytical devices in terms of lack of active control on biofluids, and enables the implementation of previously demonstrated lab-on-a-chip-based sample preparation and manipulation operations on-body. The simultaneous biofluid actuation and sensing interface enables the enhancement of the sensitivity and response time for different biochemical sensors such as glucose, choline, and H_2O_2.

The inherent simplicity of the devised fabrication and integration scheme sets forth a feasible path for scalable and low-cost manufacturing of wearable microfluidic devices. In that regard, our scheme can be adapted for the fabrication and large-scale deployment of the currently reported and future bioanalytical wearable devices, which is critical at the prototyping level, for fueling large-scale clinical investigations, as well as at the production level for commercialized consumer applications and general population health monitoring.

The demonstrated active functionalities can be equivalently adapted to implement sample processing operations such as incubation, reagent delivery, and purification, thus enabling the realization of advanced assays (particularly, those that have already been demonstrated in lab-on-a-chip settings) to create new biomarker detection solutions in a wearable format. The valve-enabled sample processing and analysis operations can be positioned as addressable compartments to form the building blocks of multistep and multichamber bioanalytical functions within microfluidic architectures, allowing for the execution of synchronous/asynchronous sequential and parallel bioanalytical objectives autonomously. On a broader level, the convergence of the active biofluid management capabilities achieved by the presented technology and other active actuation modalities allows for the creation of fully autonomous lab-on-body platforms to monitor the biomarker profiles of individuals at the point-of-person, thus informing personalized and actionable feedback toward improving the individual's health.

For the mobile system, inspired by the degrees of freedom achieved by the emergence of AGV robotic systems in terms of mobility and automation, we introduced and experimentally demonstrated the concept of a ferrobotic system. Accordingly, an amplified addressable EM actuation mechanism is devised for robotic guidance. The contactless (i.e., no ferrobotic contact with the package or the surrounding fluid) and high-strength actuation mechanism inherently renders it rapid (10 cm/s), repeatable (>10,000 cycles), and robust (>24 hours). These traits, together with the reconfigurability of the system, enabled the implementation of advanced and diverse operations through the integration of passive and active functional components. To this end, we designed and characterized droplet microfluidic operations—including dispensing, generation, merging, and filtering—where the results indicated minimal undesired operational performance deviation. Furthermore, we demonstrated the significantly elevated efficiency of the ferrobotic system for microfluidic logistics applications by deploying a network of cross-collaborative ferrobots to deliver an illustrative and generalizable package sorting objective. To showcase an application where logistics of sample dosing, merging, and mixing are required, we leveraged the advanced and cross-collaborative ferrobotic operations to achieve a pipelined and automated bioassay for the quantification of MMPs in human plasma.

Collectively, our characterization results demonstrate precise, repeatable, durable, and cross-collaborative ferrobotic operations in versatile settings. Although these operations were realized with a 32-by-32 addressable navigation floor, the scale of the ferrobotic operations can be expanded by simply adopting a larger navigation floor (requiring minimal reconfiguration of the PCB, specifically, increasing the number of EM coils). In that regard, augmentation with image or electrical ferrobot/droplet positioning sensing capabilities within the ferrobotic system will allow for the implementation of a feedback control process as a corrective measure to ensure the robustness of desired large-scale operations. Furthermore, the optical readout of the assay is currently performed using a benchtop fluorescence microscope. Further automation and integrated sample-to-answer solutions, especially in point-of-care settings, would benefit from integrated low-cost readers leveraging consumer electronic devices. Alternatively, other assays could be read using electrochemical sensors, which can be integrated onto the platform in a similar manner as the electrodes used for electrocoalescence. Exploiting the ferrofluid biocompatibility, fluorescence and electrochemical assays can be adapted for applications centering on cell and nucleic acid analysis.

On a broader level, adaptation of the ferrobotic system for translational applications necessitates future and convergent designated efforts in microscopic and macroscopic domains toward establishing a generalizable design space for the ferrobotic system. Microfluidic physicsfocused efforts are required to comprehensively model the underlying ferrobotic actuation mechanism and understand its limitations in relation to relevant forces, scaling of dimensions (including magnet-, droplet-, and microfluidic structure dimensions), fluidic properties, and other design parameters. Furthermore, macroscopically, dynamic navigation planning algorithms are required to optimize the performance of the cross-collaborative ferrobots toward the delivery of the required objective(s) and in the presence of operational constraints (such as a ferrobotic "safety distance"). To this end, readily developed models from the AGV community aiming to address issues such as layout challenges, fleet management, speed/movement limitations, and optimization functions can be adapted and applied within the framework of the ferrobotic system.

The versatility, scalability, and reconfigurability of the devised ferrobotic system allow for its adaptation to perform diverse and massively parallelized and sequential microfluidic operations relevant to diverse application spaces including point-of-care diagnostics, -omics, drug development, and chemical/material synthesis. By capitalizing on the high degree of automation that can be achieved by the presented technology, large datasets can be generated to unravel complex biological and chemical processes, seeding the transformation of the biotechnology and pharmaceutical industries and mirroring the impact of the AGV robotic systems on their respective industries.

Appendix A: Fabrication and assembly of wearable microfluidic modules for biofluid sampling

The microfluidic modules were created by assembling several layers of double-sided tape (170 μm-thick, 9474LE 300LSE, 3M) and transparent PET film sheets (100 μm-thick, MG Chemicals, which were selectively patterned with actuation and sensing electrodes). Skin adhesive medical tape (Tegaderm Transparent Film Dressing, 3M) can be incorporated in the assembly process to form the skin-interfacing layer. The microfluidic embodiments, including microchannels and VIAs, were created by laser-cutting (Epilog Mini 24, Epilog Laser) 2D patterns within the tape- and the PET-based substrates. The minimum resolution of the microfluidic device depends on the resolution of the laser-cutter. Using our basic laser cutter, we could achieve ∼100 μm features. A more advanced laser cutter can be used, if higher resolution is needed, which can render features with resolution on the order of ∼10 μm. With the proper alignment of VIAs and microchannels, fluidic connections in vertical direction were achieved, rendering the complex 3D microfluidic structures. Here, the electrode arrays were patterned on PET substrates by photolithography using positive photoresist (MicroChemicals AZ5214E), followed by the evaporation of 20 nm Cr, 100 nm Au, and 20 nm Ti for actuation electrodes and 20 nm Cr and 100 nm Au for sensing electrodes. After deposition, the lift-off step was performed in acetone. For the envisioned low-cost and disposable device design applications, screen-printing techniques can be used to pattern electrodes (following well-established protocols).

Appendix B: Fabrication procedure for epidermal microfluidic valving system

The wearable valve-enabled bioanalytical platform is composed of multiple vertically stacked layers, which can be listed from the bottom to the top as: (a) a double-sided skin-adhesive film, (b) a biochemical sensing electrode array patterned on a polyethylene terephthalate (PET, ~100 µm, MG Chemicals) substrate, (c) a microfluidic layer for sweat sampling, routing, and compartmentalization, (d) a thermo-responsive hydrogel array layer, (e) a microheater electrode array for valve switching, and (f) pressure regulator embodiments. These components are fabricated following the ensuing described protocols.

The microfluidic module is constructed by vertical assembly of double-sided tapes (170-µm thick, 9474LE 300LSE, 3 M) and transparent PET film layers. Microfluidic features such as microchannels and VIAs (Vertical Interconnect Access) were fabricated by laser-cutting (VLS2.30, Universal Laser Systems). Through the vertical alignment of the microchannels and VIAs, fluidic connections were made between different layers of the microfluidic module, rendering a 3D microfluidic structure.

The microheater electrode array was patterned on PET by photolithography using a positive photoresist (MicroChemicals AZ5214E), followed by the evaporation of 20 nm Cr, 100 nm Au, and 20 nm Ti. The sensor electrode array was also patterned on PET by photolithography using positive photoresist (MicroChemicals AZ5214E), followed by the evaporation of 20 nm Cr and 100 nm Au. The lift-off step was performed in acetone. To establish seamless electrical connections, in a spatially efficient manner between the microheater/sensor array layers and the FPCB, double-sided adhesive anisotropic conductive films (ACFs, 9703, 3 M, 50 µm) were used as VIAs to connect the contact pads of the board (located on its front- and back-sides) to the layers. Specifically, for the microheater electrode array, the connections were made to the front-side of the FPCB (from the top), and for the sensor electrode array, the connections were made to the back-side of the FPCB (from the bottom).

The thermo-responsive hydrogels were prepared by mixing 0.545 g NIPAM (Sigma-Aldrich), 0.0297 g N,N′-methylenebisacryl-amide (Sigma-Aldrich), 0.75 mL dimethyl sulphoxide (Sigma-Aldrich), 0.25 mL deionized water, 0.02 mL [3-(methacryloylamino)propyl]trimethylammonium chloride (MAPTAC, Sigma-Aldrich) solution (50 wt.% in water), and 0.0385 g 2,2-dimethoxy-2-phenylacetophenone (Sigma-Aldrich). This mixture was then sonicated in a water bath for 30 min at 48 °C with a sonication frequency of 40 kHz. Next, the mixture was injected and cast into custom-designed tape-based molds (laser-cut with the desired features), followed by a photo-polymerization step (405 nm ultraviolet light, Formlabs Form Cure, intensity: 1.25 mW cm^{-2} and exposure time: 2 min). The crosslinked hydrogels were immersed in a DI water bath for at least 12 h, prior to their deployment for the planned characterization/validation experiments.

The pressure regulators were constructed by embedding laser-cut filter membranes (GD 120 Glass Fiber Filter, Advantec MFS Inc.) in between two double-sided tape layers (170-µm thick, 9474LE 300LSE, 3 M), forming a sandwiched structure. Epoxy (Devcon) was used to seal the gap between the layers.

To develop biochemical sensing interfaces, first, platinum-based working electrodes were constructed by electrochemically depositing (−0.1 V vs. Ag/AgCl, 600 s) a platinum nanoparticle (PtNP) layer onto the designated sensor electrodes (Au-based) using an aqueous solution containing 2.5 mM Chloroplatinic acid ($H_2PtCl_6 \cdot 6H_2O$, Sigma-Aldrich) and 1.5 mM formic acid (Sigma-Aldrich). Next, a poly-m-phenylenediamine (PPD) layer was electrochemically deposited onto the PtNP/Au electrode (0.85 V vs. Ag/AgCl, 300 s) in a phosphate-buffered saline (PBS) solution (pH 7.2; Gibco PBS, Thermo Fisher Scientific) containing 5 mM m-phenylenediamine (Sigma-Aldrich). The constructed PPD/PtNP/Au electrode was then washed (with DI water) and dried at room temperature. Reference electrodes were constructed by drop-casting Ag/AgCl ink onto the designated electrodes (Au-based). Then, the deposited layer was dried at 70 °C for 30 min. It is worth noting that the Ag/AgCl reference electrode construction took place in between the PtNP and PPD deposition steps (when constructing the working electrode). Supplementary Table 2 summarizes the chemical composition of the enzymatic sensing interfaces.

To develop the glucose sensor, 0.3 μL of a 1:1 (v/v) mixture of 1% chitosan solution and glucose oxidase (50 mg ml−1 in PBS, pH 7.2; Sigma-Aldrich) was coated onto the PPD/PtNP/Au electrode (1.13 mm^2). The 1% chitosan solution was prepared by dissolving chitosan (Sigma-Aldrich) in a 2% acetic acid (Sigma-Aldrich) solution at 60 °C for 30 min. To develop the lactate sensor, a 0.3 μL of 1:1 (v/v) mixture of bovine serum albumin (BSA, Sigma-Aldrich) stabilizer solution and lactate oxidase solution (50 mg ml^{-1} in PBS, pH 7.2; Toyobo) was coated onto the PPD/PtNP/Au electrode (1.13 mm^2) and dried at room temperature for 1 h. The BSA stabilizer solution was prepared by adding 0.8% (v/v) of 25 wt.% glutaraldehyde solution (GAH, Sigma-Aldrich) in a PBS solution containing 10 mg ml−1 BSA. Then 0.3 μL of PVC solution (0.375 wt.% in Tetrahydrofuran; Sigma-Aldrich) was deposited twice (separated by 1 h) onto the electrode surface to form a lactate diffusion limiting layer. All sensors were allowed to dry overnight at 4 °C while being protected from light, prior to their deployment for the planned characterization/validation experiments.

Appendix C: ACET theory and simulation

To investigate and model ACET-induced fluidic motion, finite element analysis (COMSOL Multiphysics 5.2) was used to perform electrothermal simulation. Given the similarity of our electrode and channel configurations, the same approach was adopted to simulate the ACET phenomena. In short, application of an AC voltage across a coplanar electrode pair establishes a non-uniform electric field and subsequently non-uniform temperature, permittivity, and conductivity profiles. Consequently, the interaction of the electric field and the charge density distribution (ρ) results in a non-zero body force on the fluid. In such a system, the charge distribution must satisfy both Gauss's law and the following charge conservation conditions (equations below):

$$\nabla \times \mathbf{E} = 0 \qquad (1)$$

$$\nabla \cdot (\varepsilon \mathbf{E}) = \rho \qquad (2)$$

$$\nabla \cdot (\sigma \mathbf{E}) = -\frac{\partial \rho}{\partial t} \qquad (3)$$

By solving the above equations in the frequency domain ($\partial / \partial t = i\omega$, where ω is the angular frequency of the excitation voltage), and by applying small permittivity and conductivity gradient approximations, the ρ can be expressed as:

$$\rho = \nabla \varepsilon \cdot \mathbf{E}_0 - \varepsilon_0 \frac{\mathbf{E}_0 \cdot \nabla(\sigma + i\omega\varepsilon)}{\sigma_0 + i\omega\varepsilon_0} \qquad (4)$$

, where the subscript 0 represents the variables for a spatially constant temperature T_0.

In the case of electrothermal kinetics, the temperature gradient-induced permittivity and conductivity gradients can be expressed as:

$$\nabla \varepsilon = \varepsilon_0 \alpha \nabla T, \ \nabla \sigma = \sigma_0 \beta \nabla T, \text{ where } \alpha = \frac{1}{\varepsilon}\frac{\partial \varepsilon}{\partial T}, \ \beta = \frac{1}{\sigma}\frac{\partial \sigma}{\partial T} \qquad (5)$$

, where for aqueous solutions at 25 °C, $\alpha \approx -0.0046$ K^{-1} and $\beta \approx 0.020$ K^{-1}. After calculating the space charge density, the electrical body force density can be determined, which is the sum of a Coulomb term and a dielectric term.

$$\mathbf{f}_{\mathrm{E}} = \rho\mathbf{E} - \frac{1}{2}E^2\boldsymbol{\nabla}\varepsilon \qquad (6)$$

Combining (4), (5) and (6), the ACET body force can be expressed as:

$$\mathbf{f}_{\mathrm{E}} = [\frac{\varepsilon_0\sigma_0(\alpha-\beta)}{\sigma_0+i\omega\varepsilon_0}\boldsymbol{\nabla}T \cdot \mathbf{E}_0]\mathbf{E}_0 - \frac{1}{2}E_0^2\boldsymbol{\nabla}\varepsilon \qquad (7)$$

In the case of ACET biofluid actuation, conductivity and relative permittivity is 0.6 S/m and 80.2 respectively and AC frequency is 8 MHz. With $\omega \ll \sigma_0/\varepsilon_0$, low-frequency approximation can be applied and (7) can be simplified to:

$$\mathbf{f}_{\mathrm{E}} \approx -0.022\varepsilon_0 E_0^2\boldsymbol{\nabla}T \qquad (8)$$

which is defined as the body force in the Navier-Stokes equation when simulating laminar flow in the channel.

In the COMSOL Multiphysics simulation setup, laminar flow, heat transfer, and electric current physics were employed in the context of a 3D microfluidic channel (with a PET substrate and ceiling) containing a solution with properties similar to that of a biofluid (*e.g.*, sweat). The simulation used the same electrode dimensions as the experimental setup. The ceiling of the microfluidic channel was set as ambient temperature (25 °C) and the bottom surface of the PET substrate (assumed to be in direct contact with skin) was set as skin temperature. Other surfaces (walls of the channel) were assumed to be thermally insulated.

Appendix D: Theoretical analysis of the flow rate influence on the electrochemical sensor response

In the general case of modeling the response of a microfluidic electrochemical sensing system, analyte transport (by advection and diffusion) and surface reaction must be simultaneously considered. However, in the context at hand, because of the high enzymatic catalytic activity (i.e., high surface reaction rate), it can be assumed that the response of the electroenzymatic sensor is completely controlled by analyte transport onto the sensor surface[1]. Accordingly, the enzymatic current response can be presented as

$$I = nFAJ \quad (1)$$

, where n is the number of electrons in the electro enzymatic reaction, F is Faraday's constant, *A* is the sensing electrode area, and *J* is the analyte flux (molecules per area per time) onto the sensor surface.

When no flow rate is present, the analyte consumption on the sensor surface creates a growing analyte depletion zone with a thickness of $\delta \propto \sqrt{Dt}$, where *D* is the diffusion coefficient of the target analyte and *t* is time. Accordingly, the analyte molecules diffuse along the concentration gradient, resulting in analyte flux *J* onto the sensor surface, where $J = D\nabla c$. As the first-order approximation, the gradient ∇c can be simply equated to the difference in the analyte concentration in bulk (c_0) *vs*. immediate vicinity of the sensor surface (c_s, where $c_s \approx 0$, due to the assumption of relatively high surface reaction rate) divided by the depletion thickness (δ), hence:

$$J \approx \frac{D(c_0 - c_s)}{\delta} \approx \frac{Dc_0}{\delta} \quad (2)$$

Despite the continuous growth of the depletion thickness with time, if one takes measurements at a fixed timepoint, the proportionality of J in relation to c_0 can be exploited to establish a linear calibration curve (current response *vs.* analyte concentration).

When performing sensing in the presence of advective flow (with volume flow rate Q) inside a microfluidic chamber, because of the continuous supply of analytes, the advection halts the growth of the depletion zone, setting a steady-state δ_s. For the case where the advection transport is stronger than analyte diffusion (captured by the non-dimensional Peclet number, $Pe = \frac{Q}{DW} \gg 1$), the advective delivery of analytes results in the compression of the depletion zone following the relationship below:

$$\frac{\delta_s}{L} \sim \sqrt[3]{\frac{DH^2W}{QL^2}} \quad (3)$$

, where L is the length of the sensor and W and H are the chamber width and height, respectively[2]. Combining equations (1-3) yields $I \propto J \propto \sqrt[3]{Q}$, a trend which is in agreement with both the simulation and experimental results.

Appendix E: Force balance model of ferrofluid droplet transportation

In our model, three forces are considered to play dominant roles in ferrofluid droplet kinetics: a magnetic body force $\boldsymbol{F}_M$, friction force between the droplet and substrate $\boldsymbol{F}_f$, and drag force on a droplet in an oil environment $\boldsymbol{F}_{drag}$. Here, we ignore droplet deformation by shear because of the low capillary number, which captures the relative strength of viscous forces in the presence of surface tension. Specifically, in our context the capillary number is on the order of 0.002-0.02 (assuming surface tension ~7 mN/m , viscosity of the oil ~1.3 mPa·s, and velocity ~10-100 mm/s). Because of the low capillary number, we also assume the droplet will adopt a minimal surface shape.

The magnetic body force can be expressed as:

$$\boldsymbol{F}_M = \frac{V_M \chi}{\mu_0} (\boldsymbol{B} \cdot \nabla) \boldsymbol{B}$$

where V_M is the magnetically actuated volume of ferrofluid droplet, χ is the magnetic susceptibility (proportional to ferrofluid concentration), μ_0 is permeability of free space, and $\boldsymbol{B}$ is the magnetic flux density.

Friction force between the ferrofluid droplet and substrate of the channel is on the order of:

$$\boldsymbol{F}_f \sim K_f R_b \mu_{oil} U$$

where K_f is the friction constant, R_b is the radius of the contact area between ferrofluid droplet and substrate beneath, μ_{oil} is the viscosity of the oil, and U is the velocity of the carrier (assuming that viscous drag in the vicinity of the contact line is significant).

Given the relatively small value of the Reynold number (Re < 12-120, assuming viscosity of the oil ~1.3 mPa·s, density of the oil ~1614 kg/m3, characteristic length-scale ~1 mm, and velocity ~10-100 mm/s), and assuming that the droplet motion is in near-steady state, drag force is on the order of:

$$\boldsymbol{F}_{drag} \sim 3\pi D\mu_{oil}U\frac{1 + 2\mu_{oil}/3\mu_{ff}}{1 + \mu_{oil}/\mu_{ff}}$$

where D is the diameter of the droplet and μ_{ff} is the viscosity of the ferrofluid.

During the process of magnetic actuation, $\boldsymbol{F}_f$ and $\boldsymbol{F}_{drag}$ act as restraining forces to counteract the driving force $\boldsymbol{F}_M$. This net effect can be described as $\boldsymbol{F}_M - \boldsymbol{F}_f - \boldsymbol{F}_{drag} = ma$, where m is the mass of droplet and a is the acceleration of the droplet motion. Accordingly, this relationship sets an upper-bound on the droplet velocity, which can be expressed as:

$$U \leq \frac{\frac{V_M\chi}{\mu_0}(\boldsymbol{B}\cdot\nabla)\boldsymbol{B}}{K_f R_b \mu_{oil} + 3\pi D\mu_{oil}\frac{1 + 2\mu_{oil}/3\mu_{ff}}{1 + \mu_{oil}/\mu_{ff}}} = U_{\max} \quad (1)$$

As equation 1 shows, the concentration related variable (χ) and three size related variables (V_M, R_b, D) affect this velocity limit. Specifically, U_{max} is proportional to magnetic susceptibility χ, illustrating that a higher concentration of ferrofluid results in a larger velocity limit. For size related variables, V_M determines the magnetic actuation force (in the numerator), while R_b and D (in the denominator) affect the friction and drag force respectively. When the volume of ferrofluid droplet (V) is smaller than the characteristic length scale (on the order of the coil size) of the activated EM-field, whole droplet is considered magnetically actuated ($V_M \approx V$). In this case, the increase of V results in the increase of U_{max} because of scaling relations ($V \propto R_b^3 \propto D^3$ isometrically). However, V_M will reach a saturation value when V is considerably larger than the characteristic length scale of the localized EM-field. In this scenario, two restraining forces opposing the droplet movement, $\boldsymbol{F}_f$ and $\boldsymbol{F}_{drag}$, tend to lower the velocity limit when the carrier volume increases, caused by increasing R_b and D.